UNIVERSIDAD DE CONCEPCIÓN
FACULTY OF PHYSICAL SCIENCES AND MATHEMATICS

THE DEBIASED MORPHOLOGICAL TRANSFORMATION OF GALAXIES SINCE Z=3 IN CANDELS

LA TRANSFORMACIÓN MORFOLÓGICA INSESGADA DE GALAXIAS DESDE Z=3 EN CANDELS

By: Diego Ignacio Salvador Campe

Thesis presented to the Faculty of Physical Sciences And Mathematics of the University of Concepción to obtain the Masters Degree in Astronomy

July 2023
Concepción, Chile

Advisor: Dr. Ricardo Demarco
Co-Advisor: Dr. Pierluigi Cerulo
Astronomy Department

En memoria de mi amada abuelita Margarita, para mi mamita, Janet, y la gente que quiero.

In memory of my beloved grandmother Margarita, to my mother Janet and the people I love.

ACKNOWLEDGEMENTS

El día antes de irme de Antofagasta para empezar mi carrera, miraba con tristeza mi pieza vacía. Te sentaste a mi lado y me dijiste que era un sacrificio que debíamos hacer por un par de años. Esta tesis es el resultado final de aquel sacrificio. Espero que estés orgullosa, mamá. Gracias por ser una fuente de apoyo, cariño, sabiduría e inspiración durante toda mi vida. Gracias por permitirme cumplir esta meta y alentarme en mi búsqueda de nuevos desafíos. Gracias a mi tía hermosa, Eliana, a mi tío Marco y mis primos, Cristina y Rodrigo, por toda su ayuda y apoyo en este proceso. Sin ustedes todo hubiese sido más complicado. A mi abuelita Margarita, donde sea que estés, sigues siendo una inspiración para mí. Te extraño y te amo.

Gracias a mis supervisores, Ricardo Demarco y Pierluigi Cerulo, por todo lo que me han enseñado y por ayudarme en la elaboración de esta tesis.

También agradezco a quienes han sido mis amigos durante estos años. A Michell D., Nicolás M. e Ignacio L., por todo lo que hemos vivido desde el colegio hasta hoy. Hemos mantenido una larga amistad y por ello significan mucho para mi. A Javier C., Felipe O., Nicolás S., Vanessa A. y Rodrigo A. por ser mis compañeros de estudio, de viajes y salidas. Nombrarlos a todos me es imposible, pero gracias a todos mis amigos, los de Antofagasta (JB, MG, AI, ML y GP) y los de Concepción (AD, CC, BG, AH, RS, SR, LV, FV y MV). Gracias por su amistad, por entender mi humor ridículo y por los buenos momentos que hemos tenido. Sepan que han sido parte importante de mi vida y estoy agradecido de conocerles.

Sinceramente y de todo corazón, muchas gracias a todos.

Abstract

To trace the morphological evolution of galaxies one first needs to correctly quantify the morphological mixture at different epochs. Morphological quantitative measurements and visual-like classifications are, however, susceptible to biases such as cosmological surface brightness dimming (CSBD): the measured surface brightness of a galaxy decays with redshift as $(1+z)^{-4}$. However, the effect of CSBD on morphology has not been thoroughly discussed in literature. To investigate the impact of CSBD on morphological classifications, we employ artificial redshifting techniques on a sample of 206 galaxies in the GOODS-S field, spanning redshifts from $z = 0.2$ to $z = 3.0$. We compare the visual classifications and morphological coefficients (G and M_{20}) obtained from the original and simulated images. Subsequently, we develop two correction methods to mitigate the effects of CSBD. The first approach involves calculating correction percentages for false-positives and false-negatives in the visual classifications, while the second method is based on tracking the shifts of objects in the $G - M_{20}$ parameter space with increasing redshift. Both correction methods are then applied to a CANDELS sample. Our findings reveal that CSBD, low resolution and signal-to-noise significantly biases visual morphological classifications beyond $z > 1.0$. Specifically, we observe an overestimation of the fractions of spheroids and irregular galaxies by up to 20% and 60%, respectively, while the fractions of early and late-type disks are underestimated by up to 40%. However, we find that morphological coefficients are not significantly affected by CSBD. Furthermore, we find that galaxies tend to increase their asymmetry and G value, and decrease their M_{20} and half-radius toward high-redshift, thus exhibiting a more diffuse, asymmetric, and less clumpy appearance at higher redshifts. We validate the consistency of our correction methods by applying them to the observed morphological fractions in the IllustrisTNG-50 sample, yielding similar results to those obtained from the CANDELS sample. This suggests that the TNG simulation effectively reproduces galaxy evolution in terms of morphology. We propose two potential confusion channels in morphological classifications due to CSBD: galaxies may be misclassified as spheroids or as irregulars. Additionally, we analyze the morphological fractions of star-forming and quiescent subsamples as a function of redshift and stellar mass. Our investigation of the quiescent subsample reveals a decreasing trend in the fraction of late-type disk galaxies

with cosmic time, while the fractions of quiescent early-type disks and spheroid galaxies. Star-forming late-type galaxies are also found to decrease at the exchange of an increasing irregular fraction. Our results imply that late-type-disks are transforming into star-forming irregulars or into quiescent spheroids/early-type disks. We suggest that merger events are responsible for the morphological transformation of late-type disks and that the increase in bulge mass is driving the star-formation quenching.

Keywords – Galaxies – galaxies: evolution – morphology – cosmological surface brightness dimming – morphological fractions – fields

Contents

List of Tables

List of Figures

Chapter 1

Introduction

Galaxies are baryonic and dark matter over-densities that have been or are capable of transforming cold molecular gas into stellar mass Huertas-Company et al. (2016). The star formation rate of a galaxy will depend on whether internal and external processes that act in favor of star formation (e.g gas inflow and cooling) dominate over the processes that halt it (e.g. AGN-feedback and gas heating) or vice versa. The well-known star formation rate density (SFRD) versus redshift (z) diagram shown by Madau and Dickinson (2014) shows that the Universe reaches a star formation peak around $z \sim 2$ and subsequently experiences a decrease until present times. The latter is due to quenching processes (Renzini, 2016) and lower molecular gas fractions at low redshifts (Gobat et al., 2020). Despite the ubiquity of this trend, the details of the physical processes that drive quenching remain elusive and require further investigation.

Regardless of whether galaxies lose their ability to form stars, their stellar populations continue to evolve. The evolution of both quenched and star-forming galaxy stellar populations produces a well-defined galaxy bimodality in a color-magnitude diagram. Specifically, the star-forming galaxies congregate in the demarcated blue cloud, while the passive, non-star-forming galaxies are clustered in the so-called red sequence (Strateva et al., 2001; Baldry et al., 2004). Moreover, when examining the relationship between the star formation rate (SFR) and the stellar mass (M_*) of galaxies, those that are actively forming stars generally populate a main sequence that lies above a region occupied by passive galaxies.

Observational investigations (e.g. Christlein and Zabludoff, 2005; Bruce et al.,

2012; Wang et al., 2012; Lee et al., 2013), have demonstrated that there is a link between the morphology of galaxies and their star-forming activity. Explicitly, star-forming galaxies that populate the main sequence and the blue cloud typically have disk-like shapes, while passive galaxies that lack ongoing star formation and predominantly occupy the red sequence exhibit a dominant spheroidal morphology. This link underscores how the morphology of galaxies, a property that refers to their shape and spatial distribution of light, is interconnected with other physical properties, including color and star formation rate (Brennan et al., 2015).

There is abundant evidence (e.g. Hausman and Ostriker, 1978; Abraham and van den Bergh, 2001; van Dokkum and Franx, 2001; Postman et al., 2005; Genzel et al., 2008; van der Wel, 2008; Cerulo et al., 2017) on the evolution of the morphological mixing of galaxies with time. In the local Universe galaxies are predominantly bulge-dominated (elliptical and lenticular, early-type), whereas at $z = 3$, approximately 80% of galaxies exhibit disk-like morphologies. However, this fraction declines to approximately 20% in the nearby Universe as noted by (Conselice et al., 2004; Delgado-Serrano et al., 2010; Conselice, 2014). These findings motivate us to explore the potential links between the mechanisms that trigger or quench star formation and the morphological transformations of galaxies.

Galactic mass and size are two additional properties that experience temporal evolution (e.g Longhetti et al., 2007; van Dokkum et al., 2008; Duncan et al., 2014). Firstly, Bruce et al. (2012) reported that galaxies at higher redshifts are more compact than their local counterparts, with galaxies in the range $1 < z < 3$ being a factor 2.3 ± 0.1 times smaller ($\sim 2.6 \pm 0.2 kpc$) than local galaxies. The gas mass fraction (M_{gas}/M_*) of massive disk galaxies increases with redshift, with the gas fraction rising from 0.1 at $z = 0.2$ to 1.0 at $z > 2$ (e.g Carilli and Walter 2013a and references therein). This implies that, at $z \sim 2 - 3$, molecular gas mass is comparable to or even exceeds stellar mass. A higher gas fraction is also seen in high redshift passive galaxies (Gobat et al., 2020; Magdis et al., 2021). Additionally, Carilli and Walter (2013a) found that galaxy sizes increase between redshift $z = 3.0$ and the present epoch. The size evolution factor varies in the range $2 - 5$, with spheroidal galaxies exhibiting a faster rate of size evolution than disk galaxies. Other physical properties such as the star formation rate (Franx et al., 2008), color (Cerulo et al., 2019) and metallicity (Rupke et al., 2010) are also found to evolve.

The drivers of the evolution of morphology and other physical properties in galaxies can be subdivided into two groups: *i)* external or environmental processes, such as galaxy-galaxy and galaxy-ICM/IGM interactions and pre-processing; and *ii)* internal processes which are related to stellar and AGN feedback and secular evolution, which refers to the mechanisms related to disk, bar, rings or dark matter halo instabilities that result in a gradual change in morphology (Buta, 2011).

Empirical evidence from several studies, including the Butcher and Oemler (1978) effect, the morphology-density relation (Dressler, 1980; Postman et al., 2005; Holden et al., 2007; van der Wel, 2008), and the star formation-density relation (Patel et al., 2011), indicates that the environment in which a galaxy resides plays a crucial role in shaping its evolutionary path. It is thought that galaxies that live in dense environments are subject to a series of mechanisms, such as gas stripping (Gunn and Gott, 1972), galaxy harassment (Moore et al., 1996), galaxy strangulation (Larson et al., 1980), and mergers (Hopkins et al., 2009), which can modify or transform their morphology and quench their star formation (Fasano et al., 2000). Among dense environments, galaxy clusters stand out as the most massive ($M \sim 10^{14-15}\, M_{\odot}$) and largest ($R \sim 1 - 5\, Mpc$) virialized structures in the Universe, with a high galaxy density ($\Sigma \geq 30\, [gal/Mpc^2]$) and a greater frequency and impact of environmental mechanisms on their member galaxies (Treu et al., 2003). As expected, early-type galaxies are found to primarily reside in dense environments. The fraction of early-type galaxies in cluster cores is roughly $22 - 30\%$, decreasing by a factor of two toward less dense regions (cluster outskirts and in-fall regions), in contrast to the behavior of late-type galaxies (Calvi et al., 2012). These observations indicate that the environment where a galaxy is located plays a critical role in shaping its evolutionary path.

While there is a considerable amount of publications on the relationship between morphology and star formation in galaxy clusters, studying the morphological evolution of galaxies in both cluster and field environments is necessary for a through understanding of galaxy evolution. Correctly tracing the evolution of the morphological mix of galaxies is crucial to understanding the relationship between morphology and star formation in both the cluster and field environments. This can be achieved by quantifying the morphological fraction of galaxies at different redshifts and environmental densities, and using these results to develop a model that can interpret the observational results.

However, the expansion of the Universe and the presence of the intergalactic medium affect the transmission of the light from the source to the observer. Therefore, an observer might be led to perceive a different morphology compared to the real one. There are two main sources of bias that can arise from cosmic expansion. Firstly, the wavelength-dependent morphological K-correction. Due to the expanding Universe, sources observed at high redshifts are sampled at different rest-frame frequencies (Windhorst et al., 2009; Buta, 2011), which poses a significant challenge in understanding their morphology. The light we perceive from galaxies is a combination of the emitted light from stars, gas, and dust present within them. When observing a galaxy at different wavelengths, we are effectively probing different components, leading to potential variations in the object's appearance. Consequently, we say that the morphology of galaxies is a function of wavelength. So, when observing galaxies at high redshift, one has to make sure that the difference between the observed and the rest-frame wavelength is not large enough that the observed morphology may be altered. On the other hand, the expansion of the Universe also results in a decrease of the observed surface brightness with redshift which follows a power-law of the type $(1+z)^{-4}$ (cosmological surface brightness dimming, CSBD; Tolman 1930). This constitutes the second source of bias, which, together with the effects of extinction and low resolution in images of high-redshift objects (i.e. the angular size of galaxies becomes comparable with the full width at half maximum of the point spread function), can lead to a distorted perception of the true morphology of galaxies.

Most of the literature on CSBD primarily focuses on the selection (Malmquist) bias, which is the systematic preference to detect only high surface brightness galaxies at high redshift (e.g Bouwens et al., 2004; Calvi et al., 2014; Paulino-Afonso et al., 2017). However, there is limited discussion on the impact of CSBD on morphology (Barden et al., 2008). As part of this study, we aim to evaluate whether the morphological classification bias introduced by CSBD significantly affects the estimation of the fractions of the morphological types of galaxies (hereafter morphological fractions). This evaluation will enable us to determine whether it is necessary to decouple the effect of CSBD to retrieve the underlying morphological evolution of galaxies.

In order to assess and evaluate the CSBD bias we have developed two methods to correct the morphological fractions, which are both based on the artificial

redshifting of a galaxy. To this end we utilized the DOPTERIAN software (Paulino-Afonso et al., 2017) to simulate how a low-redshift ($z = [0.2 - 0.4]$) reference sample of 206 galaxies from the Great Observatories Origins Deep Survey South (GOODS-S) field (Guo et al., 2013) would be observed at higher redshifts due to surface brightness dimming. The first correction method consisted in building a team of four classifiers who visually labeled both the original and the simulated galaxies in the reference sample. The morphological types of the simulated high-redshift galaxies were compared with those of the original galaxies, and then the correction factors that accounted for the false-positive and false-negative in both samples were derived. Non-parametric statistics, such as the Gini coefficient (G) and the M_{20} coefficient, provide quantitative measures to characterize galaxy morphology. The Gini coefficient assesses the inequality of light distribution within a galaxy, while the M_{20} coefficient quantifies the concentration of light in a galaxy. The second correction method relies on the change of position of the original and simulated galaxies in the $G - M_{20}$ plane caused by CSBD. The correction terms were derived in this case using the information from the parent sample and the Bayes' theorem to construct a generative model that predicted the most likely shifts for objects in the $G - M_{20}$ plane.

We applied these two correction methods to a sample of 25,456 galaxies from the Cosmic Assembly Near-Infrared Deep Extragalactic Legacy Survey (CANDELS, Grogin et al., 2011; Koekemoer et al., 2011) at redshifts ranging from $z = 0.2$ to $z = 3.0$. We further analyzed the observed and CSBD-corrected morphological fractions as a function of redshift and stellar mass, and separately investigated the morphological fractions of star-forming and quiescent galaxies. We also compared our findings with the predictions of the IllustrisTNG-50 simulation (Nelson et al., 2019; Pillepich et al., 2019). The results from this work support a scenario in which the fraction of late-type disk galaxies decreases towards $z \sim 0$, while the fraction of spheroids increases.

The results obtained from this study will facilitate future comparisons of the evolution of morphological types as a function of environmental density and contribute to a better understanding of the morphological evolution of field galaxies as well as the impact of CSBD on morphological classification.

This thesis is organized as follows. Chapter 2 gives insights to the objectives of this thesis. Chapter 3 introduces the dataset used in the study, including the

sample of galaxies, the images and the simulations. In Chapter 4 we outline the methods employed to derive and correct the morphological fractions and present the results of the analysis. Chapter 5 provides a comprehensive discussion and interpretation of the results, which are summarized in Chapter 6.

Chapter 2

Science Goals and Objectives

2.1 General and Specific Objectives

The primary objective of this thesis is to investigate the evolutionary patterns of morphological fractions in field galaxies across cosmic time, with a focus on redshift [insert specific redshift range]. By tracing the temporal changes in morphological fractions, the aim is to gain insights into the morphological mixing processes occurring in field galaxies throughout the history of the universe.

The main goal of this thesis is to trace the morphological mixing evolution (the changes of morphological fractions across cosmic time) of field galaxies at redshift $0.4 \leq z < 3$, taking into account the bias introduces by CSBD as a consequence of the expansion of the Universe. By tracing the temporal changes in morphological fractions, the aim is to gain insights into the morphological evolution processes occurring in field galaxies throughout the history of the universe.

The specific objectives of this thesis are:

- To measure the morphological fractions of field galaxies in the CANDELS survey as a function of redshift and stellar mass at $0.4 \leq z < 3.0$.
- To quantify the CSBD-bias and to develop corrections methods that can be used to correct this effect from morphological measurements.
- To compare of the observed and corrected morphological fractions with those estimated in the IllustrisTNG-50 simulation.

- To interpret and analyze our results in the context of morphological transformation and the quenching of star formation.

2.2 Activities

During the development of this thesis, the following activities were carried out:

1. Collection of images and data.
    - Download of the CANDELS survey mosaics and catalogs containing information (position, stellar mass, redshift, morphological classification, etc.) of the sample galaxies.
    - Pre-processing of the images by preparing image cut-outs (postage stamps) of the galaxies being studied.
2. Sample selection and image degradation/simulation.
    - Selection of the reference 'parent sample' from the GOODS-S field. The galaxies were selected in the range $0.2 < z < 0.4$.
    - Artificially redshifting of galaxies in the parent sample using DOPTERIAN, according to the CSBD-law. Galaxies were simulated for six different redshift bins: $0.4 < z < 1.0$ (bin 1), $1.0 < z < 1.25$ (bin 2), $1.25 < z < 1.5$ (bin 3), $1.5 < z < 2.0$ (bin 4), $2.0 < z < 2.5$ (bin 5) and $2.5 < z < 3.0$ (bin 6).
3. Development of the first correction method.
    - The original images and their simulated versions were visually classified following a classification scheme of: spheroids, lenticulars, early-type disks, late-type disks, irregular and point sources or artifacts.
    - Morphological classifications were compared and correction percentages for false-positives and false-negatives were calculated.
4. Development of the second correction method.
    - To estimate the morphological coefficients (G and M_{20}) of the original and simulated images of the galaxies of the parent sample.
    - To use Bayes' theorem to build a generative model that retrieves the

most likely shift in the position of an object in the $G - M_{20}$ plane, for a given pair of observed coefficients.

- To assign a morphological label based on the values of the corrected coefficients using the criterion suggested in Sazonova et al. (2020).

5. Estimate morphological fractions as a function of redshift and stellar mass.
6. Comparison with cosmological simulations.
    - Repeating the process stated above but for the IllustrisTNG-50 simulation sample.
7. Analysis of the results.
    - Analysis of the evolution of the corrected morphological fractions, comparing it with other results. The analysis attempts to relate the results to morphological transformations in the context of the quenching of star formation.

Chapter 3

Theoretical Framework

3.1 Morphology

The morphological classification is a crucial step in the study of galaxies, as it provides valuable information regarding their evolutionary history and physical properties. Morphology refers to the shape and structure of a galaxy, and can be described in several ways. The structure of a galaxy is intimately linked with its internal dynamics and star formation activity. For instance, spiral galaxies typically have ongoing star formation in their disks, while elliptical galaxies tend to have older populations of stars and less (or no) star formation and are more dispersion dominated (Cappellari, 2016). Thus, by studying the morphological classification of galaxies, astronomers can gain insights into their formation and evolution, as well as the physical processes that govern their properties.

In the first instance, we need to establish a morphological classification system; that is, an arrangement of classes of objects ordered according to their visual characteristics and amount of (sub-)structures in their light distribution. If the chosen classification system is clever, then galaxies could be separated into fundamental classes such that *i)* objects in the same class are morphologically similar (although their physical properties might be different) and *ii)* objects of different classes are significantly different from each other (Binney and Merrifield, 1998). The most widely used classification system is the *Tuning fork* described by Hubble (1926, 1936), which consists of a sequence that starts with elliptical galaxies and terminates with spiral galaxies, which may or may not be barred.

Sandage (1961) proposed that the morphological classification starts from the recognition of *i)* the smoothness of the light distribution and *ii)* the presence of two structures: *a)* a disk, a flat and extended structure; and *b)* the bulge, a compact spheroidal structure. From this convention, four main morphological types have been historically acknowledged: *i)* elliptical galaxies (E), characterized by a concentrated light distribution, a dominant bulge and an absent disk (or negligible if present); *ii)* lenticular galaxies (S0), those with a concentrated light distribution and a disk without spiral arms; *iii)* spiral galaxies (Sp), those in which a bulge and a dominant disk with spiral arms are detectable to the eye, and with a sharper cut-off in their light distribution; and *iv)* irregular galaxies, which do not have any light distribution pattern or the dominant presence of a bulge or a disk. Hubble's early-type galaxies, namely lenticulars and ellipticals, have none or little star formation, and because they are mainly made out of population II stars, they populate the red sequence of the color-magnitude diagram. Spirals and irregulars, or Hubble's late-type galaxies, are typically located in the blue cloud, as they typically have population I stars and are associated with strong star formation activity.

3.1.1 Galaxy Structure

3.1.1.1 Visual morphology

The morphological classification of galaxies based on human-eye examination is the earliest and most direct approach to the structural labeling of galaxies. Although humans possess the ability to identify sub-structures and patterns within galaxies, visual morphology is subject to personal interpretation, rendering it rather subjective. The primary drawback of this form of classification lies in its discreteness, as visual classifications are typically discrete in nature while morphology properties constitute a continuum (see e.g. Cappellari et al., 2011). Consequently, visual classification results in the loss of fine-grained structural information regarding galaxies. To ensure the robustness of visual classification, it is essential to use the same classification criteria within a sample of galaxies. If classification is done in stages, the criteria should be ordered by priority. Additionally, the sample should be homogeneous. For instance, galaxies should be observed at the same wavelength and with the same resolution.

Visual classification becomes increasingly impractical as the size of a dataset expands. Current astronomical surveys such as the Sloan Digital Sky Survey (SDSS, York et al., 2000), the Kilo Degree Survey (KIDS, de Jong et al., 2013) and CANDELS contain data for hundreds of thousands of galaxies, and this number will increase once the Simonyi Survey Telescope of the Vera Rubin Observatory begin operations. The visual classification in such large datasets would be extremely time consuming and, for this reason, during the latest fifteen years there has been a growing use of automated classification methods based on machine learning and deep learning (Pérez-Carrasco et al., 2019). These algorithms can be trained with a sample of visually labeled galaxies and produce human-like classifications. Since it is possible in this way to manage large volumes of data within a short period, automated methods have become an invaluable tool in astronomy.

The visual-based morphological classification are subject to the classifier's criteria, as some structural features may be considered significant to some classifiers and insignificant to others. This challenge remains even with machine learning algorithms trained for visual-like classifications, as they are trained to recognize only specific patterns while potentially overlooking less prominent features. This highlights another problem with visual classification: it is not considered a fundamental type of classification and should therefore be carefully analyzed and accompanied by quantitative analysis whenever possible.

3.1.1.2 Parametric methods

A parametric approach for the morphological classification of galaxies is a rigorous technique that employs mathematical models to describe the structural characteristics of galaxies. This method quantifies galaxy morphology by fitting analytical models to the observed light profiles or isophotes of the galaxies. These models are defined by a set of parameters, such as the size, shape, and orientation of the galaxy components. The fit of these models to the observed data is then utilized to determine the morphological type of the galaxy.

One of such techniques is the fitting of integrated light profiles, which involves measuring the variation of the average intensity of a galaxy with respect to its radius. Although initially introduced by de Vaucouleurs (1948), a comprehensive

formalism for describing light profiles of galaxies was proposed by Sérsic (1963):

$$I(R) = I_0 \cdot exp\left\{-b(n) \cdot [(R/R_e)^{1/n} - 1]\right\}, \tag{3.1.1}$$

where the surface brightness at radius R is denoted as $I(R)$, the surface brightness at the effective radius R_e, where half of the total flux of the galaxy is enclosed, is denoted as I_0, $b(n)$ is a normalization constant which contains half of the galaxy's total light within the effective radius, and n is the Sérsic index, a parameter utilized to characterize the concentration of the brightness distribution, in other words, this gives the shape of the light profile.

The primary structural parameters of a galaxy are n and R_e. Values of $n < 2.5$ typically indicate disk-dominated galaxies, while values $n \geq 2.5$ indicates bulge-dominated structures. At $n = 4$ the Sérsic profile coincides with the de Vaucouleurs profile, which was proposed in de Vaucouleurs (1948) as the light profile for elliptical galaxies. On the other hand, $n = 1$ coincides with the exponential profile, which is typical of the most disc-dominated galaxies.

Several codes have been developed to quantitatively analyze the light profiles of galaxies. The most widely used ones employ one- or two-dimensional fitting methods to model elliptical radial profiles and incorporate convolution with one or multiple point spread functions (PSFs). Examples of such codes include BUDDA (de Souza et al., 2004), Gim2D (Simard, 2010) and GALFIT (Peng et al., 2011). The latter is a two-dimensional fitting code designed to extract structural components from galaxy images in the most flexible possible way. Depending on the case, the morphology of a galaxy can be approximated using a single component (usually an ellipsoidal shape) or through the sum of multiple components (bulge+disk or bulge+disk+bar). According to the visual morphology of the galaxy and the resolution of the image, the user can decide the number of components to fit.

This type of analysis has been used to develop the study the evolution of disks, explore the cosmic evolution of morphology, investigate dark matter and baryonic matter distributions, study the fundamental plane of spheroids (Gudehus, 1973; Djorgovski and Davis, 1987), and investigate the formation of supermassive black holes, quasar host galaxies, and other topics (see Peng et al. (2011) and references therein).

Although parametric methods have several advantages for classifying the morphology of galaxies, they also have limitations. This kind of models assume a specific functional form for the galaxy's light profile, and so while they may provide accurate fits to many galaxies, they may not be able to capture the full complexity of the observed morphology, particularly for galaxies with irregular or asymmetric features. Additionally, small errors in these assumptions can result in significant biases in the estimated structural parameters. Finally, the fitting procedure for complex models with multiple components can be computationally demanding and may require specialized hardware for an efficient analysis.

3.1.1.3 Non-parametric methods

A less computationally intensive alternative to the parametric light profile fitting in the quantitative study of galaxy morphology is provided by the non parametric morphological coefficients. These quantities provide estimates of the concentration, asymmetry and smoothness of galaxies without assuming a functional form for the light profile.

The non parametric coefficients have the advantage of being flexible and able to capture a wider range of morphologies than the parametric methods, since they allow one to quantify the asymmetry and clumpiness of galaxies besides their concentration, which may be missed in the parametric models. On the other hand, the non parametric-coefficients do not allow one to perform a bulge-disk decomposition, thus missing key structural properties of galaxies.

We provide a definition of key non-parametric coefficients commonly utilized in characterizing galaxy morphology.

- **Concentration (C).** C is the ratio between the fluxes measured within two concentric circular or elliptical apertures which are chosen to contain two different fractions (30% and 70% or 20% and 80%) of the galaxy's light. The centers of the aperture coincide with the center of the galaxy:

$$C = 5 \log \left(\frac{r_{80}}{r_{20}} \right), \tag{3.1.2}$$

  where r_i are the circular apertures containing i% of the total flux. The total flux is defined as the flux contained within $1.5r_p$ (r_p being the Petrosian

radius[1] Graham et al., 2005) from the galaxy center. The center of the galaxy is determined by asymmetry minimization.

- **Asymmetry (A).** The asymmetry coefficient (A) is a morphological statistic that measures the degree of rotational symmetry of a galaxy's light distribution, as introduced by Conselice et al. (2004). To calculate A, the original image of the galaxy is subtracted from a rotated version of the image by 180° around the galaxy's central pixel. The absolute value of the pixel differences is summed and divided by the total flux of the galaxy, minus the average asymmetry of the background. The central pixel that minimizes the value of A is used as a reference point. The asymmetry coefficient provides a quantification of the degree of asymmetry or irregularity in the galaxy's morphology. The asymmetry coefficient is then defined as:

$$A = \frac{\sum_{i,j} |I(i,j) - I_{180}(i,j)|}{\sum_{i,j} |I(i,j)|} - B_{180}, \tag{3.1.3}$$

  where I is the galaxy image and I_{180} is the image rotated by 180° about the central pixel of the galaxy, and B_{180} is the average asymmetry of the background.

  The shape asymmetry (A_s) coefficient was proposed by Pawlik et al. (2016) as a method to identify galaxies with low-surface-brightness tidal features. Unlike the traditional asymmetry coefficient, A_s uses segmentation mask images to weight all parts of the galaxy equally and quantifies its overall level of asymmetry. The calculation of A_s is similar to that of the traditional asymmetry coefficient, with the difference being the use of segmentation mask images (an image where each pixel is assigned a label corresponding to a specific object within the image) instead of galaxy light images. This approach allows for the measurement of asymmetry independently of the galaxy's light distribution information.

- **Smoothness** or **clumpiness** (**S**). (S) quantifies the degree of small-scale structures, like compact star clusters. The image is smoothed by a boxcar

[1]The Petrosian radius is defined as the radius at which the ratio of the local surface brightness to the average surface brightness within that radius falls below a specified threshold, which is typically set to 0.2 (Bershady et al., 2000; Guaita et al., 2015).

kernel and then subtracted from the original image:

$$S = \frac{\sum_{i,j} |I(i,j) - I_S(i,j)|}{\sum_{i,j} |I(i,j)|} - B_S, \tag{3.1.4}$$

where I_S is the flux in the galaxy image smoothed by a boxcar of width $0.25r_p$, and B_S is the average smoothness of the background.

Most of these indices are sensitive to signal-to-noise ratio (S/N) and resolution. Although they do not assume any particular analytical form for the light distribution of a galaxy, because of the way these coefficients are defined, a certain circular symmetry is assumed, which may not be true, for example, in the case of irregular galaxies. This problem is overcome by the Gini coefficient (Abraham et al., 2003) and M_{20} (Lotz et al., 2004).

- The Gini coefficient (G) quantifies the inequality in the light distribution within a galaxy (Abraham et al., 2003). It is calculated by sorting the pixel fluxes in the image from lowest to highest and comparing the resulting distribution to a perfectly uniform light distribution which is parametrized with the Lorenz curve (Florian et al., 2016). The latter curve is defined as:

$$L(p) = \frac{1}{\bar{X}} \int_0^p F^{-1}(u) du, \tag{3.1.5}$$

where p is the percentage of faintest pixels, $F(x)$ is the cumulative distribution function, and $\bar{X}$ is the mean over all (pixel flux) values (X_i). The Gini coefficient is the ratio of the area between the Lorenz curve and the *uniform equality* curve (where $L(p) = p$) to the area under the curve of uniform equality. In the discrete case, the Gini coefficient is the mean of the absolute difference between all X_i:

$$G = \frac{1}{2\bar{X}n(n-1)} \sum_{i=1} \sum_{j=1} |X_i - X_j| = \frac{1}{\bar{X}n(n-1)} \sum_{i}^{n} (2i - n - 1) X_i, \tag{3.1.6}$$

where n is the number of pixels in a galaxy. G will take a value of 0 when all pixels have the same value, and will take the value 1 when all the galaxy's flux is in one pixel. Note that, unlike C, Gini is independent of the large-scale spatial distribution of the galaxy's light.

It is important to note that that the inclusion of *sky pixels*, and the exclusion

of *galaxy pixels* in the calculation of G will systematically increase/decrease this index, respectively. One could consider the pixels of the galaxy as all those that exceed a threshold of surface brightness.

- The total second order moment (variance) M_{tot} is defined as the flux of each pixel f_i multiplied by the square of the distance to the center of the galaxy, summed over all the pixels of the galaxy (Lotz et al., 2004),

$$M_{tot} = \sum_{i}^{n} M_i = \sum_{i}^{n} f_i[(x_i - x_c)^2 + (y_i - y_c)^2], \tag{3.1.7}$$

where x_c and y_c are the coordinates of the galaxy center, computed by finding the pair (x, y) that minimizes M_{tot}. We define M_{20} as the normalized second-order moment of the brightest 20% of the galaxy's flux:

$$M_{20} \equiv \log 10 \left(\frac{\sum_i M_i}{M_{tot}} \right), \qquad \text{while} \quad \sum_i f_i < 0.2 f_{tot}, \tag{3.1.8}$$

where f_{tot} is the total flux of the galaxy pixels, and f_i is the flux of each individual pixel ranked in such a way that f_1 is the brightest pixel. Then, M_{20} is a comparison between the brightness of the brightest regions to the total brightness of the galaxy, and provides a measure (values between 0 and -4.0) of how concentrated those bright regions are within the overall structure of the galaxy. Defining The 20% threshold is commonly chosen in astronomy because higher values produce unrealistic results, while lower values lead to a less discriminating statistic.

As noted by (Lotz et al., 2004), M_{20}, unlike the concentration coefficients, is not measured within circular or elliptical apertures and it relies on how the light is distributed within the galaxy as is depends on the squared distances between pixels and the brightest regions of a galaxy.

The Parametric and non parametric methods for quantitative morphology differ in several ways. Parametric methods assume a specific functional form for the light distribution, while non-parametric methods do not make strong assumptions about the underlying distribution. This makes non-parametric methods more flexible, as they can adapt to the complexity of the data without relying on assumptions about the light distribution. Parametric methods typically use a

fixed number of parameters to describe the data, while non-parametric do not assume that the shape of a galaxy is not represented by an analytic relationship. In terms of interpretability, parametric methods are generally more interpretable than non-parametric methods, as they provide a clear set of parameters that can be used to understand the behavior of the model. Non-parametric methods may be less interpretable, as they rely on flexible models that can be difficult to understand.

3.1.1.4 Integral Field Spectroscopy

Integral field (IF) spectrographs are instruments capable of acquiring spectra in different positions across a galaxy. In an IF unit a spectrum is acquired for each spaxel (an array of pixels, the unit element that collects the light to produce a spectrum) of the detector. IF spectroscopy allows one to go beyond the visual, non-parametric and parametric structural measurements, since in this way one can study the underlying kinematics and star formation rate as a function of position within a source. In addition to these physical properties, IF spectroscopy also permits the study of the chemical composition and age of the galaxy as a function of position, thus allowing, in principle, the simultaneous study of different aspects of the evolution of galaxies (star formation, AGN, chemical evolution).

High-resolution spectra of galaxies can provide valuable information on their structure that may not be captured by parametric or non-parametric methods alone. This is because spectra can reveal the detailed kinematics of a galaxy, including its rotation, velocity dispersion, and asymmetric features such as gas outflows and inflows (Carilli and Walter, 2013b; Sobral et al., 2013; Tumlinson et al., 2017; Paillalef et al., 2021). By analyzing these kinematic features, it is possible to infer the underlying structure of the galaxy, such as the presence of rotation- or dispersion-dominated components.

Although IF spectroscopy seems to makes the study of galaxy morphology obsolete, there are still limitations in the use of spectra in the study of galaxy structure. High-quality data and specialized equipment are required to obtain the necessary information, and the analysis process can be time-consuming and computationally intensive. So IF spectroscopy can be used on a small sample of galaxies, while the structural and morphological analysis of galaxies can be applied to large data-sets.

The most comprehensive method for the study of galaxy structure would thus consist of a combination of high-resolution IF spectroscopy and morphological analysis techniques.

3.1.2 Morphological types

Galaxy morphology classification is, as it has been mentioned, based on two visual properties: the symmetry of the light distribution and the presence/absence of a disk (Sandage et al., 1975; van der Wel et al., 2010). In this section we define the main four morphological types, adopting the descriptions provided in Buta (2011) and Conselice (2014).

3.1.2.1 Elliptical galaxies

The light distribution of elliptical galaxies is typically symmetric and smoothly varying, with a steep decline in brightness toward the outskirts of the galaxy. They exhibit a circular or elliptical shape, and a high concentration of stars in their central regions. These galaxies are predominantly composed of old stellar populations, containing very little gas and dust. In addition, their effective radius, central velocity dispersion, and mean effective surface brightness are linearly related to each other into a plane known as the fundamental plane (Djorgovski and Davis, 1987). The light distribution of elliptical galaxies is typically symmetric and smoothly varying, with a steep decline in brightness toward the outskirts of the galaxy.

Elliptical galaxies are commonly divided further into sub-classes based on their projected ellipticity, denoted as E_m, as defined in Hubble's classification scheme. The parameter is calculated as:

$$E_m = 10\left(1 - \frac{b}{a}\right),$$

where a and b represent the semi-major and semi-minor axes of the galaxy's isophotes, respectively, yielding a measure of the galaxy's flattening factor. The parameter m is an integer ranging from 0 to 7, indicating the apparent flattening of the galaxy, with higher values of m corresponding to galaxies with a more elongated shape and 0 corresponding to a circular object.

Kormendy and Bender (1996) proposed a more quantitative approach to classify

elliptical galaxies based on their velocity anisotropy. A property is anisotropic if it varies with the direction in which it is measured. The velocity anisotropy correlates with the size of the deviations of the isophotes from an elliptical fit. If the relative amplitude of the deviation is positive, the isophotes are pointed and oval in shape, and the galaxy is classified as E(d). On the other hand, if the relative amplitude is negative, the isophotes are boxy and oval in shape, and the galaxy is classified as E(b) (Sandage et al., 1975). It has been found that boxy ellipticals, E(b), have more velocity anisotropy than disky ellipticals, E(d).

The luminosity profiles of large and luminous elliptical galaxies can be effectively described by the Sérsic profile ($r^{1/n}$) with different values of n greater than 3 (Graham and Guzmán, 2003). These galaxies exhibit high values of concentration (~ 4.4) and low values of asymmetry (~ 0.02) and smoothness (~ 0.0) in terms of their morphological coefficients (Conselice, 2014). Additionally, elliptical galaxies have lower values of Gini and M_{20} compared to other types of galaxies.

3.1.2.2 Spiral galaxies

Spiral galaxies are characterized by the presence of a rotating disk of stars and gas, featuring a central bulge and extending spiral arms. The arms contain most of the dust and gas and therefore they host most of the star formation regions in the galaxy. A notable characteristic of these galaxies is the transition from a redder bulge region, predominantly comprised of older stars, to a distinct disk region that is dominated by a younger population of stars.

The morphology of spiral galaxies is often classified based on Hubble's classification system Hubble (1926, 1936), which describes the apparent spiral structure in terms of the smoothness of arms, pitch angle, and degree of winding, ranging from Sa to Sd, where Sa is characterized by the tightest, largest, and smoothest arms and Sd correspond to loosest, smaller, and fainter arms. Sb and Sc are intermediate classes (de Vaucouleurs, 1959). Spiral galaxies that have bars in the center are classified as SBa, SBb, SBc, or SBd. Moreover, the strength of the bulge decreases as the arms become more extended and clumpy from Sa to Sd, resulting in the designation of Sa-Sb types as early-type disks (i.e. disk galaxies with a significant bulge component) and Sc-Sd types as late-type disks (i.e. disk galaxies resembling pure disk) as mentioned in Buta (2011).

Freeman (1970) proposed a fitting function for the luminosity profiles of spiral galaxies, consisting of a combination of an exponential disk and a central bulge component, with the latter being more dominant in early-type disks. Compared to elliptical galaxies, spiral galaxies have lower concentration values, with early-type disks having $C \sim 3.9$ and late-type disks having $C \sim 3.1$; higher values of asymmetry, with early-type disks having $A \sim 0.07$ and late-type disks having $A \sim 0.15$; and higher clumpiness, with early-type disks having $S \sim 0.08$ and late-type disks having $S \sim 0.29$. Additionally, spiral galaxies exhibit lower values of concentration and the Gini coefficient and higher values of M_{20} coefficients compared to ellipticals (Lotz et al. 2008).

3.1.2.3 Lenticular galaxies

Lenticular galaxies, also referred to as S0 galaxies, possess a hybrid morphology that combines features of both spiral and elliptical galaxies. Similar to spiral galaxies, they have a disk-shaped structure, albeit lacking prominent spiral arms, and their bulges are bigger than those of spirals. A central bar and a surrounding disk of stars are common to lenticular galaxies, but the disk is dominated by older, redder stars and lacks the gas and dust typically found in spiral galaxies, resulting in negligible star formation. With these characteristics, lenticular galaxies are assigned the S0 designation due to the fact that they share properties with both Sa and E7 in the Hubble and de Vaucouleurs classification systems. Therefore, lenticulars are also considered as early-type disks.

It has been proposed that lenticular galaxies, which share many similarities with spiral galaxies, may be formed by the removal of gas from a spiral galaxy (van den Bergh, 2009; Laurikainen et al., 2010) or by mergers (Querejeta et al., 2015; Tapia et al., 2017; Eliche-Moral et al., 2018).

When inspecting them visually, face-on lenticular galaxies may easily be confused with elliptical galaxies. At high redshift, they may also be confused with red spiral galaxies (passive or nonstar forming spiral galaxies, Masters et al. 2010). As a result, the detection of S0 galaxies through visual classification is challenging and constitutes one of the main sources of uncertainty in the morphological classification.

Lenticular galaxies possess luminosity profiles that are intermediate between

those of elliptical and spiral galaxies. In terms of non-parametric morphological coefficients, lenticular galaxies typically have intermediate values of the C, A, S, G, and M_{20} coefficients.

3.1.2.4 Irregular galaxies

Irregular galaxies are galaxies that do not have a distinct shape like elliptical, spiral, or lenticular galaxies. They lack the spiral arms and central bulge of spiral galaxies, and they do not have the smooth, symmetrical shape of elliptical or lenticular galaxies. Instead, irregular galaxies have a chaotic, asymmetric shape, with no apparent structure or pattern. They are often characterized by a high level of ongoing star formation, which gives them a bright, patchy appearance. Irregular galaxies are often originated through galaxy collisions, tidal interactions, and gas accretion. Irregular galaxies may have originally been spiral or lenticular galaxies that were disrupted by gravitational interactions with other galaxies (Chapman et al., 2003).

These galaxies have been classified into two sub-types (Buta, 2011). Irregular type I (Irr I) galaxies lack symmetry or well-defined arms, but exhibit some degree of structure such as bright knots or arms. Irr I galaxies have two sub-types: spiral-like (Sm) and non-spiral-like (Im). Irregular type II (Irr II) galaxies are asymmetric objects that lack any type of structure.

Irregular galaxies have a wide variety of luminosity profiles, which can be influenced by their recent star formation activity and interactions with other galaxies. High values of asymmetry are common among irregular galaxies, which often exhibit irregular shapes and lack a clear bulge-disk structure. The C, A, S, G, and M_{20} coefficients of irregular galaxies can vary widely, depending on their specific morphology and recent star formation activity.

3.2 The Law of Cosmological Surface Brightness Dimming

The intensity or surface brightness of a source is defined as the flux per unit solid angle. In astronomy it is commonly measured in magnitudes per square arcsecond or solar luminosities per squared parsec. The observed flux can be related to the

observed surface brightness Σ_0 as:

$$\Sigma_0 = \frac{F}{\Omega}, \tag{3.2.1}$$

where $\Omega = A/d^2$ is the solid angle of the source and $A = \pi(D/2)^2 = \pi R^2$ is the area of the source in the sky (D is the diameter of the source). We can then write the flux of a source in terms of its luminosity distance (d_L):

$$F = \frac{L}{4\pi d_L^2}. \tag{3.2.2}$$

Then, we can express surface brightness as:

$$\Sigma_0 = \frac{[L/(4\pi d_L^2)]}{(\pi R^2)/d_A^2} = \frac{L}{4\pi d_L^2} = \frac{L}{4\pi\left(\frac{R^2}{4}\right)}\frac{d_A^2}{d_L^2} = \frac{L}{\pi R^2}\cdot\left(\frac{d_A}{d_L}\right)^2, \tag{3.2.3}$$

where d_A is the angular distance. Both luminosity distance and angular distance are defined in Appendix A.

Notice that the $L/(\pi R^2)$ term is the intrinsic surface brightness (Σ). We further write:

$$\Sigma_0 = \Sigma\cdot\left(\frac{d_A}{d_L}\right)^2, \tag{3.2.4}$$

$$\Sigma_0 = \Sigma\cdot\left(\frac{d_l}{(1+z)^2}\frac{1}{d_L}\right)^2, \tag{3.2.5}$$

$$\Sigma_0 = \frac{\Sigma}{(1+z)^4}. \tag{3.2.6}$$

So the observed surface brightness of a source at redshift z is $(1+z)^{-4}$ lower than if it were at $z = 0$. This implies that distant galaxies smaller and fainter than their counterparts in the local Universe just as a consequence of the cosmic expansion.

Chapter 4

The Data

The focus of this study is the morphological evolution of galaxies in low-density environments, and for this purpose we built a sample from the five fields of the Cosmic Assembly Near-infrared Deep Extragalactic Legacy Survey, CANDELS (Grogin et al., 2011; Koekemoer et al., 2011).

CANDELS is an observational program that obtained deep images (mosaics) of the GOODS-S, GOODS-N, EGS, COSMOS, and UDS fields using the Hubble Space Telescope (HST) WFC3/IR and ACS cameras over a period of 902 orbits. The CANDELS HST imaging survey was chosen for this study for three main reasons. Firstly, the survey covers a large area of about $130 arcmin^2$ and $720 arcmin^2$ in its deep-mode and wide-mode, respectively, containing images of more than 250,000 galaxies, allowing for high statistics that are necessary in the study of the morphological mixing in the field. Secondly, the photometric depth in the F160W (H) band is high, reaching up to ~ 27.0 magnitudes, which allows us to obtain high-quality structural information on galaxies (Grogin et al., 2011) that is crucial for this study. Finally, the CANDELS fields have been extensively explored by the scientific community, and this has resulted in a large amount of high-quality public datasets containing photometric and spectroscopic redshifts, stellar masses, rest-frame colors, morphological classifications and Sérsic structural parameters. The accumulation of a vast library of ancillary data from these fields allows for contextualization and comprehensive comparisons of the results obtained in our study with other results already published in the recent literature.

The selection criterion employed in our study of the CANDELS sample defines

all galaxies within the redshifts range $z = 0.4 - 3.0$ and with H-band magnitudes in the AB photometric system (Oke and Gunn, 1983) less than 24.5. These criterion yielded a sample of 25,456 galaxies with stellar masses ranging from $log(M_*) = 9.00$ to $log(M_*) = 12.00$.

To analyze the morphology of the sample, we relied on the visual-like morphological classifications provided by Huertas-Company et al. (2015), who utilized a convolutional neural network (CNN) architecture to classify all objects in the five CANDELS fields. The CNN algorithm was trained with the visual classifications provided by Kartaltepe et al. (2015) and produced a series of values between 0 and 1, indicating the likelihood of each galaxy belonging to one of the morphological classes defined in (Kartaltepe et al., 2015): dominant spheroid (f_{sph}), dominant disk (f_{disk}), dominant irregular (f_{irr}), dominant point source (f_{ps}), and unclassifiable (f_{unc}). To convert the set of five morphological frequencies to a single morphological class label, we followed the criterion proposed in Huertas-Company et al. (2016):

- **Spheroid:** $f_{sph} > 2/3$ and $f_{disk} < 2/3$ and $f_{irr} < 1/10$.
- **Late-type disk:** $f_{sph} < 2/3$ and $f_{disk} > 2/3$ and $f_{irr} < 1/10$.
- **Early-type disk:** $f_{sph} > 2/3$ and $f_{disk} > 2/3$ and $f_{irr} < 1/10$.
- **Irregular:** $f_{sph} < 2/3$ and $f_{irr} > 1/10$.

As explained in Huertas-Company et al. (2016) the thresholds are calibrated through visual inspection to make sure that the intervals corresponded to distinct morphological classes.

4.1 Parent Sample

In order to quantify the impact of CSBD and to develop effective correction methods, we constructed a parent sample that comprises 206 galaxies from the GOODS-S field (Guo et al., 2013) located at $z = 0.2 - 0.4$. We selected a parent sample of galaxies with H < 24.5 AB, corresponding to the limit used by Huertas-Company et al. (2016). The physical properties of the control sample, such as their coordinates, stellar mass, bulge mass, Sérsic indices, redshift, star formation rate and others, were obtained from the published catalog associated with the

3D-HST Treasury Program (Momcheva et al., 2016)[1].

We use the F160W photometric band mosaic of the GOODS-S field retrieved from the 3D-HST Treasury program (Grogin et al., 2011; Koekemoer et al., 2011; Brammer et al., 2012; Skelton et al., 2014; Momcheva et al., 2016), which is available in the Mikulski Archive for Space Telescopes (MAST) data archive[2], to visually classify all objects from the parent sample. To facilitate the classification of the 206 objects, we extracted postage stamp images of each galaxy from the F160W band mosaic. Each postage stamp is centered in the object and its size is set to four times the geometric mean of the semi-major axis and the semi-minor axis of the Petrosian ellipse[3].

4.2 Simulating the Surface Brightness Dimming

In 1930, Tolman (1930) conducted observational comparisons of the surface brightness of elliptical galaxies in three clusters at varying distances to test the expansion of the Universe. His study revealed that the surface brightness of extended objects in the sky, such as galaxies, is affected by the expansion of the Universe. The surface brightness of a source at optical, near-UV and near-IR wavelengths is typically measured in magnitudes/arcsec^{-2} or $erg\,sec^{-1}\,cm^{-2}\,arcsec^{-2}$ and is expected to decrease as $(1+z)^{-4}$ (as demonstrated in Chapter 3). The first $(1+z)$ factor is attributed to time dilation, which causes a decrease in the number of photons received per unit of time, while the second factor is due to the decrease in the energy carried by photons as they shift to lower wavelengths when they travel through space. The remaining two factors are due to the object appearing larger in two dimensions, being closer to us by a factor of $(1+z)^2$ at the time the light was emitted (Lerner et al., 2014). This phenomenon, CSBD effect consists in that the observed surface brightness Σ_0 of an extended source with intrinsic surface brightness Σ, located at redshift z, is given by equation 3.2.6 (Calvi et al., 2014).

As outlined in the introduction, one of the primary effects attributed to the surface

[1]Available here.
[2]Available here.
[3]The Petrosian ellipse is an ellipse that encloses a fixed fraction of the total flux of a galaxy, regardless of its shape. The Petrosian flux is the amount of light that falls within the Petrosian ellipse.

brightness dimming is the systematic under-detection of low-surface brightness high-redshift galaxies. Various investigations, including works by Bouwens et al. (2004) and Calvi et al. (2014), have suggested that the CSBD does not significantly influence the observed size of galaxies, but instead introduces a detection bias against fainter sources.

Our objective is to examine whether the CSBD results in a substantial source of bias in identifying the morphological and structural traits of non-compact galaxies, such as irregular or disk galaxies. To this end, we have artificially degraded our parent sample of 206 galaxies based on the CSBD law. By comparing the original images with their simulated versions at higher redshifts, one can quantify the impact of CSBD and develop methodologies to correct its effects.

To simulate the impact of CSBD on our galaxy sample, we utilized the software *DOPTERIAN* (Paulino-Afonso et al., 2017). *DOPTERIAN* is a Python implementation of the IDL routine *FERENGI* (Barden et al., 2008), which simulates high-redshift observations of low-redshift galaxies. *DOPTERIAN* achieves this by accounting for changes in the source's angular size and surface brightness, as briefly described in the following steps:

1. The input image, of pixel size p_i (angular size of the pixel in arcseconds), is modified for cosmological effects (i.e. changes in the source's angular size and surface brightness) by re-binning the image into an output-image of pixel size p_f, while preserving the galaxy's physical scale and the image total flux.

2. The flux of each pixel is scaled to correct for the effect of surface brightness dimming, as described by equation (3.2.6). In addition, the evolution of surface brightness dimming across redshift is taken into account by introducing a luminosity evolution factor. This factor is obtained from the work of Sobral et al. (2013).

3. Creation of a point spread function (PSF) convolution kernel to compensate for the differences between the input and output PSFs. This step is critical, since with the shrinking and degrading of the images performed in the previous two steps, the original PSF is also shrunk. The output and shrunken input PSFs are transformed into the Fourier space and the spectrum of the former is divided by that of the latter. This is equivalent to a deconvolution

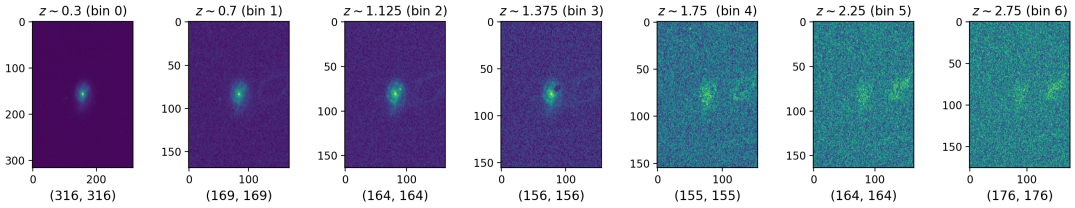

Figure 4.2.1: Postage stamps of a parent sample galaxy across different redshift bins. The pixel scale of each stamp varies, while preserving the physical scale of the image. As redshift increases, there is a gradual loss of the characteristic spiral morphology in the observed galaxy.

of the output PSF by the shrunken input PSF. The obtained spectrum is transformed back to the spatial domain, providing in this way the convolution kernel for the degraded image.

4. The kernel is convolved with the corrected and re-scaled image. Poisson noise is added randomly, and the galaxy is then placed on top of an image of an empty patch of the sky derived from the original image.

The simulations also incorporate changes in resolution and signal-to-noise ratio. However, we hereafter will refer to these modifications that may also affect the surface brightness of the source simply as CSBD. For further details and information on the working procedures of *DOPTERIAN* and *FERENGI*, the reader is referred to the works of Paulino-Afonso et al. (2017) and Barden et al. (2008), respectively. An example of the simulations performed on one of the galaxies in the parent sample is illustrated in Figure 4.2.1.

Each postage stamp was simulated at random redshifts within six predefined redshift bins, resulting in six artificially redshifted versions of each of the 206 galaxies in the parent sample. The redshift bin ranges are presented in Table 4.2.1. From now on, we use the terms *parent sample* and *original sample* interchangeably when referring to the 206 galaxy images that have not been artificially redshifted.

Bin	$[z_{low} - z_{high}]$	Intermediate z
0	0.2-0.4	0.3
1	0.4-1.0	0.7
2	1.0-1.25	1.125
3	1.25-1.5	1.375
4	1.5-2.0	1.75
5	2.0-2.5	2.25
6	2.5-3.0	2.75

Table 4.2.1: Redshift ranges of each bin. The intermediate z indicates a representative redshift for every bin.

4.3 The Comparison Sample: Illustris-TNG50 simulation

According to the standard ΛCDM cosmological paradigm, the first structures of the Universe are thought to have formed from matter over-densities, where there was an excess of matter compared to the average density of the Universe (Abel et al., 1998). These over-densities gravitationally collapsed and eventually led to matter-condensation and thus the formation of small structures (Ryden and Gunn, 1987). One of the prevailing theories of galaxy formation suggests that galaxies formed hierarchically (Cole et al., 2000), as smaller structures merged together. However, understanding the formation and evolution of galaxies in detail is a highly complex task.

The evolution of these structures is influenced by a variety of physical processes, such as gravitational, radiative, hydrodynamical, and magnetic effects, like star formation, gas cooling and heating, chemical enrichment, and feedback mechanisms (e.g. supernovae, AGN, and outflows). Furthermore, all of these phenomena can act simultaneously and with varying degrees of dominance in different epochs of the Universe.

In recent years, various analytical and semi-analytical models and numerical simulations have been developed to model the evolution of the Universe, providing estimates of physical and cosmological parameters and building a cosmic scenario consistent with observations. Among the most significant of these simulations is the Illustris-TNG50 project (Nelson et al., 2019; Pillepich et al., 2019), which is an updated successor to the original Illustris simulation (Genel et al., 2014;

Vogelsberger et al., 2014b,a). The project uses large-scale magneto-hydrodynamic simulations to realistically model the cosmic evolution of the Universe, taking into account the effects of gravity, fluid dynamics, magnetic fields, gas diffusion, radiative phenomena, and structure formation, including stars, galaxies, galaxy clusters, and black holes.

Varma et al. (2022) trained a model based on a convolutional neural network on simulated images of galaxies produced from IllustrisTNG-50 to classify them morphologically. The morphological scheme that these authors used is similar to Huertas-Company et al. (2015) and for this reason we use the publicly released catalog of galaxy morphologies as a comparison sample for CANDELS.

4.3.1 Galaxy Formation and Evolution in IllustrisTNG

The Illustris simulation encompasses various essential aspects, including hydrodynamics, employing the quasi-Lagrangian moving mesh code *AREPO* (Springel, 2010), gas heating and cooling models, ultraviolet (UV) background radiation, star formation, chemical enrichment, supernovae kinetic feedback, black hole growth and merging, as well as radio and quasar-mode AGN feedback. The general objective of the Illustris project is to establish an effective theory for galaxy formation across a broad range of masses, redshifts, and environments. To achieve this, the simulation is calibrated to reproduce the observations of the Universe's specific star formation rate ($sSFR$) evolution. The aim extends beyond the creation of realistic galaxies, as it also encompasses considerations of the hierarchical growth of structures (such as mergers, accretion, etc.) and their implications for large-scale structure formation. If the simulation successfully captures the average galaxy population, it can be employed as an invaluable exploratory tool, facilitating investigations into various phenomena related to galaxy formation and evolution.

Nevertheless, the Illustris simulation is subject to three main limitations: *i)* the overprediction of the specific star formation rate ($sSFR$) at $z < 1$ (Vogelsberger et al., 2014a); *ii)* the overprediction of the low- ($M* < 10^{10} M_{\odot}$) and high-ends ($M* > 10^{11} M_{\odot}$) of the galaxy mass function toward $z < 1$ (Genel et al., 2014); and *iii)* the failure to reproduce the bimodality in galaxy colors for galaxies with $M* > 10^{9} M_{\odot}$ at $z \sim 0$ (Vogelsberger et al., 2014b). In order to address these issues, the IllustrisTNG project builds upon the foundation of the Illustris

framework and incorporates numerical improvements and new physical models. In particular, IllustrisTNG introduces magneto-hydrodynamics, black hole-driven winds, and refined galactic wind feedback. These additions aim to more accurately capture the morphology, color, metallicity, and magnetic field distribution within the simulated galaxies. IllustrisTNG provides predictions of galaxy interactions, as demonstrated by the predominant role of satellite accretion and mergers in the mass accumulation of the most massive galaxies. Remarkably, these galaxies acquire more than half of their total mass through such mechanisms, surpassing the significance of internal star formation processes as the primary driver of their mass growth (Pillepich et al., 2019).

4.3.2 The Illustris-TNG50 sample

The present investigation employed the highest resolution product of the IllustrisTNG project, namely the IllustrisTNG-50 simulation (Nelson et al., 2019; Pillepich et al., 2019), which consists of a simulated volume of 50 Mpc. The choice of this particular version of the simulation was motivated by the availability of morphological measurements of some of the galaxies in the associated supplementary data catalogs. These catalogs were published by Huertas-Company et al. (2019) and Varma et al. (2022), who used a similar convolutional neural network model developed by Huertas-Company et al. (2019) and described in Chapter 4 to perform the morphological classification of galaxies. Specifically, they applied this model to six snapshots (25, 29, 33, 40, 50, and 67) of the TNG50 simulation, corresponding to redshifts z = 3.0, 2.4, 2.0, 1.5, 1.0 and 0.5, respectively. The algorithm was applied to synthetic CANDELS-like galaxy images generated from the IllustrisTNG-50 products.

Varma et al. (2022) used the *SKIRT* radiative transfer code (Baes et al., 2011) to create these images in four different HST filters (F435W, F606W, F775W, F160W) and mimic the properties, depth, and resolution of a CANDELS-like observational sample. The resulting catalog provides the probabilities (frequencies) for each galaxy to belong to one of three major morphological classes, namely dominant disks (f_{disk}), dominant spheroids (f_{sph}), and irregulars (f_{irr}). We use these probabilities to obtain a single dominant class label for each galaxy in our study, following the same criteria suggested in Varma et al. (2022):

- **Spheroid:** if $f_{sph} > 0.5$ and $f_{disk} < 0.5$.

- **Early-type disk:** if $f_{sph} > 0.5$ and $f_{disk} > 0.5$ and $f_{irr} < 0.5$.
- **Late-type disk:** if $f_{sph} > 0.5$ and $f_{disk} < 0.5$ and $f_{irr} < 0.5$.
- **Irregular:** $f_{irr} > 0.5$.

The resulting simulation sample comprises a total of 10,487 galaxies with stellar masses in the range $9.0 < \log(M_*/M_\odot) < 12.0$.

4.4 Star-forming and Quiescent Galaxy Separation

To divide all of our samples into star-forming and quiescent galaxies, we used a $\log_{10}(SFR)$ cut. To account for the evolution of the SFR of main-sequence galaxies with redshift, we adopted the parametrization provided by Schreiber et al. (2015):

$$\log_{10}(SFR_{MS}[M_\odot/yr]) = m - m_0 + a_0 r - a_1[max(0, m - m_1 - a_2 r)]^2, \quad (4.4.1)$$

where $r \equiv \log_{10}(1+z)$, $m \equiv \log_{10}(M_*/10^9 M_\odot)$, $m_0 = 0.5 \pm 0.07$, $a_0 = 1.5 \pm 0.15$, $a_1 = 0.3 \pm 0.08$ and $m_1 = 0.36 \pm 0.3$ and $a_2 = 2.5 \pm 0.6$.

Assuming that galaxies along this main-sequence follow a normal SFR distribution with standard deviation σ_{SFR}, we initially consider that all galaxies that are $3\sigma_{SFR}$ below the main sequence are quiescent. In the resulting star-forming sample, we fit a non-parametric curve using a Gaussian process (a mathematical tool that models the relationship and patterns within a set of data points, assuming that their values are distributed according to a Gaussian distribution), assuming that the SFR is a normal distributed variable. Then we split again the sample into star-forming and quiescent galaxies, now having a new value for the standard deviation about the main sequence, σ_*. We again define as quiescent every galaxy that is now below $3\sigma_*$. We keep fitting a non-parametric curve and repeating the above $3-\sigma$ clipping procedure until no more objects are removed from the star-forming subsample and added to the quiescent subsample.

Chapter 5

Analysis and Results

The present chapter describes the methods developed for the analysis of the CSBD and its effects on galaxy morphology and presents the results on the redshift and stellar mass evolution of the morphological fractions.

To investigate the impact of CSBD on the estimation of morphological fractions, we developed two approaches for quantifying and correcting this effect. The first approach is based on the comparison of the visual classification assigned to the original and redshifted galaxies, while the second approach is based on the displacement of objects in the G-M_{20} plane, specifically the change in the positions of the galaxies in this plane between bin 0 ($z \sim 0.3$) and a higher redshift bin. Using the information from the parent sample's original and simulated images, the first method yields a set of correction percentages for false-positive and false-negative classifications, while by following the second method we generate a G-M_{20} plane position correction probability distribution. These methods can be applied to any other sample to obtain CSBD-corrected morphological estimates.

Before explaining both methods, it is important to introduce the morphological scheme used in the analysis. We initially classified galaxies into seven morphological classes: ellipticals, lenticulars, early-type disks, late-type disks, irregulars, point sources and unclassifiable/artifacts. The initial subdivision in these morphological classes was revised in order to align our results with those of previous studies (e.g. Kartaltepe et al., 2015; Huertas-Company et al., 2016; Cerulo et al., 2017; Varma et al., 2022; Huertas-Company et al., 2023; Jacobs et al., 2023). Specifically, we merged the lenticular and early-type spiral classes into early-type

disks. Additionally, we eliminated from our parent sample all objects that were categorized as unclassifiable/artifacts or point sources in any given redshift bin. As a result of these modifications, our parent sample was reduced to 157 objects and categorized with a 5-class morphological classification scheme:

- **Spheroids:** Galaxies with a smooth and round/elliptical appearance that is centrally concentrated. This class includes only ellipticals.
- **Early-type disks:** Galaxies with a distinct flat disk structure that may or may not exhibit visible spiral arms. They also feature a significant central bulge. This class includes Sa and Sb spirals and lenticulars.
- **Late-type disks:** Galaxies with a distinct flat disk structure that may or may not exhibit visible spiral arms. The also feature a small or no bulge. This class includes Sc and Sd spirals.
- **Irregulars:** Objects that do not have a regular structure, are neither spheroidal nor have a disk-dominated morphology. They may exhibit asymmetries, tidal tails, merging features, or other signs of morphological disturbances. This class includes only irregulars.
- **Point sources and unclassifiable:** Point sources are round-like sources whose internal structure cannot be resolved due to their small size. Objects may be labeled as unclassifiable due to a variety of reasons such as image issues (e.g. satellite trail, proximity to a bright star or galaxy, etc.), spuriousness of the object (e.g. part of a diffraction spike), or extreme faintness of the object that makes it impossible to discern any structure.

5.1 Morphological Fractions

The morphological fractions are defined as the ratio of the number of objects of a specific morphological type to the total number of objects considered within each redshift bin. In a statistical framework, these fractions can be understood as the success rate proportion in a Bernoulli probability distribution. Here, the number of objects belonging to the target morphological type is considered as the successes, while the total number of objects in the redshift or stellar mass bin is the sample size i.e. the total number of trials. The measured success rate is obtained from a sample that is part of a population, and hence, is referred to as

the sample proportion, denoted as $\hat{p} = k/n$.

If we were to randomly choose different samples of the same size, we would obtain various values for the observed sample proportion, which would follow a specific probability distribution. We assume the existence of an unknown population proportion p, whose point estimator is the measured proportion $\hat{p}$. Since the point estimate of the population proportion is sensitive to the selected sample, it is essential to present the estimate $\hat{p}$ with a range of uncertainty.

The Beta distribution is a normalized version of the likelihood of observing the ratio k/n for a given value of p, and has the form:

$$B(a,b) = \frac{(a+b-1)!}{(a-1)!(b-1)!} p^{(a-1)} q^{(b-1)}. \tag{5.1.1}$$

Assuming that all values of p are equally likely ($P_{prior} = 1$, for $0 < p < 1$), the Beta distribution can be used to estimate the credibility intervals of p from the observed sample proportion $\hat{p}$, as done in Cameron (2011). The lower (p_l) and upper (p_u) limits of the credibility interval of p, for a confidence level $c = 1 - \alpha$, are given by:

$$\int_0^{p_l} B(a,b)dp = \frac{\alpha}{2} \quad \text{and} \quad \int_{p_u}^{1} B(a,b)dp = \frac{\alpha}{2}. \tag{5.1.2}$$

The morphological fractions can be interpreted as the population proportion in a hypothetical experiment in which k galaxies of a given morphological type are randomly *drawn* from a sample of n galaxies. In this work we consider the mean of the Beta function as the best estimator for the morphological fractions and we adopt a confidence level of $\pm 68\%$ for the estimation of the uncertainties on the fractions. Following Cameron (2011), in the extreme cases $k = 0$ and $k = 1$ we take the median of the distribution as the estimate for the fractions.

Number counts in limited regions of the sky such as those probed in the CANDELS survey may be affected by cosmic variance. In order to determine the importance of this source of error in the number counts of the parent sample we used the method described in Trenti and Stiavelli (2008) and implemented in an on-line calculator, to derive the fractional errors arising from cosmic variance in the GOODS-South field at $z = 0.2 - 3.0$. We obtained the values 0.15 ($z \sim 0.3$), 0.14

Bin/Class	Spheroids	Early-type disks	Late-type disks	Irregulars
Bin 0 ($z \sim 0.3$)	9	80	44	24
Bin 1 ($z \sim 0.7$)	25	80	34	18
Bin 2 ($z \sim 1.125$)	42	83	13	19
Bin 3 ($z \sim 1.375$)	57	75	2	23
Bin 4 ($z \sim 1.75$)	63	56	1	37
Bin 5 ($z \sim 2.25$)	60	36	0	61
Bin 6 ($z \sim 2.75$)	55	17	0	85

Table 5.2.1: Morphological counts for every redshift bin.

($z \sim 0.7$), 0.13 ($z \sim 1.125$), 0.13 ($z \sim 1.375$), 0.13 ($z \sim 1.75$), 0.12 ($z \sim 2.25$) and 0.12 ($z \sim 2.75$).

We also estimated the cosmic variance and Poisson noise budget for each redshift bin in the CANDELS sample, finding 0.13 ($z \sim 0.3$), 0.08 ($z \sim 0.7$), 0.06 ($z \sim 1.125$), 0.07 ($z \sim 1.375$), 0.06 ($z \sim 1.75$), 0.06 ($z \sim 2.25$) and 0.02 ($z \sim 2.75$). The mean fractional errors given by equation 5.1.2 for every redshift bin are 0.08 ($z \sim 0.3$), 0.03 ($z \sim 0.7$), 0.04 ($z \sim 1.125$), 0.04 ($z \sim 1.375$), 0.02 ($z \sim 1.75$), 0.03 ($z \sim 2.25$) and 0.05 ($z \sim 2.75$).

5.2 First Method: Visual Classifications

A group of four classifiers (DS, PC, FO, CG)[1] assigned a morphological class to all the galaxies in the original image set, as well as the artificially redshifted ones. The morphological type of each object was defined as the mode of all the classifications. The objects for which all the classifications were different from each other (43) and was not possible to derive the mode were reclassified by DS. The results of the visual classifications in the F160W band can be found in Table 5.2.1.

For a significant proportion of galaxies the visual morphological type changes with redshift as a result of CSBD: for only $\sim 19\%$ (or 30 galaxies) in the parent sample the visual type remained unchanged across all redshift bins.

The change in the morphological type for galaxies initially assigned to the same morphological class in bin 0 is shown in Figure 5.2.1. For instance, in the upper left panel of the figure it can be seen the visual classification change of all galaxies

[1]Diego Salvador, Pierluigi Cerulo, Felipe Oyarzo and Caleb Gatica.

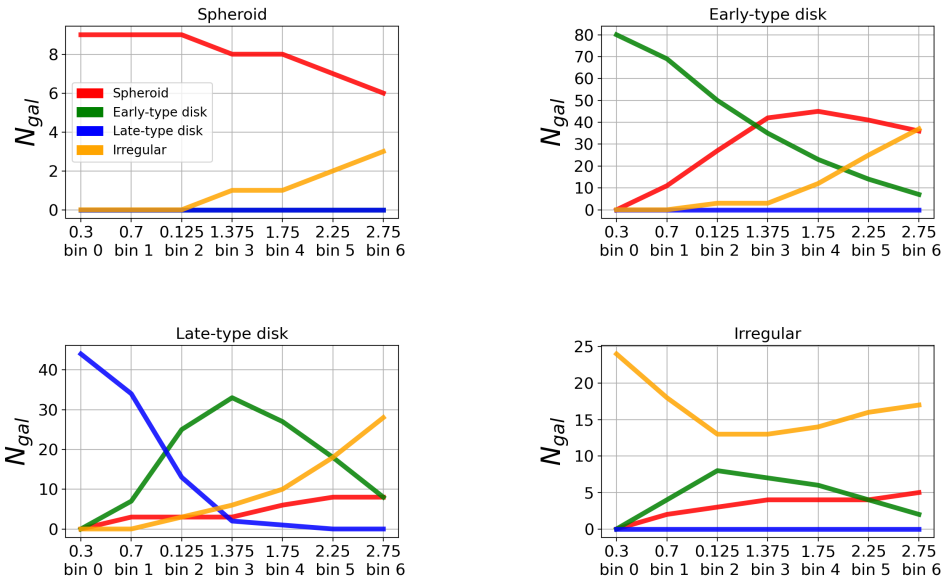

Figure 5.2.1: Evolution of initial classifications as a function of redshift. Each panel displays all galaxies that share a morphological label in the bin 0. This diagram provides insights into which morphological classes each morphological type is commonly confused with and in what quantity.

classified as spheroids in bin 0. The plot helps visualizing the number of galaxies that were misclassified in each redshift bin. It is evident from the results that at higher redshifts, spheroids are frequently misclassified as irregular galaxies. On the other hand, irregular galaxies and early-type disks are often misclassified as spheroids and irregular galaxies, respectively. Additionally, late-type disks are occasionally misidentified as early-type disks.

The misclassification may be primarily attributed to two confusion channels: galaxies tend to either look more bulge-dominated or their apparent structure becomes more irregular. The former channel likely accounts for the misidentification of spheroids and early-type disks, while the latter translates into the misidentification of irregular galaxies. We will expand more on this in the discussion section.

5.2.1 Morphological Count Correction

Results from Figure 5.2.1 provide strong evidence that in the analysis of morphological counts of high-redshift sources it is important to account for the

effect of CSBD as it can lead to misclassification of galaxies and hence compromise the reliability of the estimated morphological fractions. Thus, it is important to take into account the possibility that galaxies may be assigned an erroneous morphological type at high redshift. In particular the following situations can happen:

1. Objects in bin i that are actually of the target class A, are classified as class A. This group is called **true-positives** (TP).
2. Objects in bin i that are not actually of the target class A, are not classified as class A. This group is called **true-negatives** (TN).
3. Objects in bin i that are actually of the target class A are classified as being of another class B. This group is called **false-negatives** (FN).
4. Objects in bin i that are actually of class B, are classified as type A. This group is called **false-positives** (FP).

Correcting the observed morphological fractions for the effect of the CSBD bias implies, then, correcting for the false positives and false negatives cases described above. Let us now define the correction factors or percentages for false positives and false negatives.

- **False positives (FP).** The true-positive rate is defined as the number $n_{i,A}$ of objects of type A observed in bin i that are actually of class A, divided by the total number of sources of class A observed in the same bin, $N_{i,A}$. Then, the correction factor for false-positives for galaxies of type A in bin i is:

$$FP_{i,A} = (1 - TP) = 1 - \frac{n_{i,A}}{N_{i,A}}. \tag{5.2.1}$$

- **False negatives (FN).** Of the $N_{i,B}$ objects of type B observed in bin i, $n_{i,B,A}$ actually belong to class A. Then, the false-negative correction factor for galaxies of type A that are classified as type B in bin i is given by:

$$FN_{i,A,B} = \frac{n_{i,B,A}}{N_{i,B}}. \tag{5.2.2}$$

- Thus, the corrected number of counts of type A galaxies in bin i, $N_{i,A}$, is

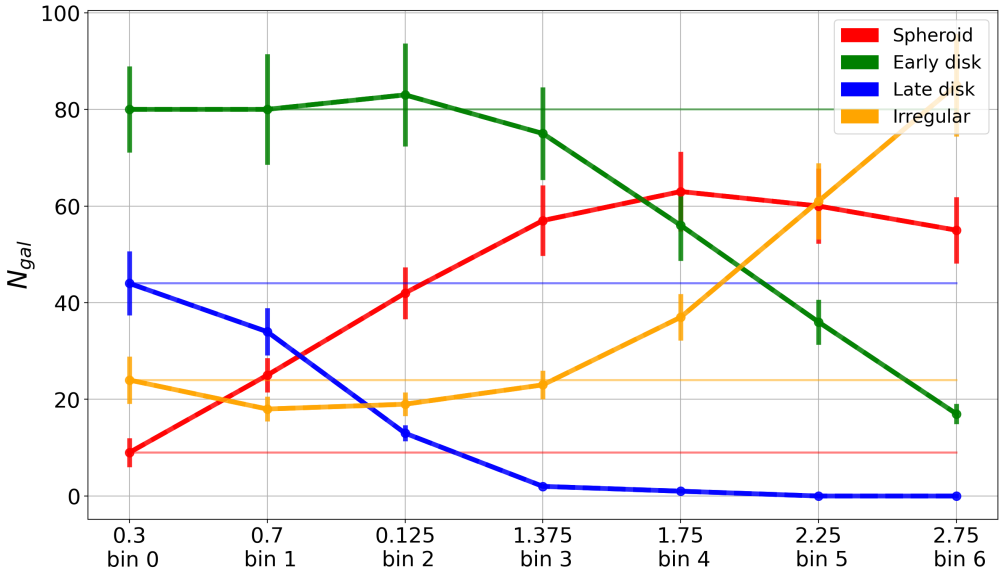

Figure 5.2.2: Visual morphological counts of the parent sample as a function of redshift. Each color corresponds to a specific morphological class, as indicated in the legend. The dark solid lines represent the observed counts, while the opaque solid lines represent the CSBD-corrected counts. The corrected counts maintain a consistent value, equal to the counts in bin 0, indicating that the correction successfully retrieves the unbiased morphological counts at all redshifts. The error bars show the bias introduced by Poisson error and cosmic variance.

given by:

$$N_{i,A} = X_{i,A} - (X_{i,A} \cdot FP_{i,A}) + \left(\sum_C X_{i,C} \cdot FN_{i,A,C} \right), \tag{5.2.3}$$

$$= X_{i,A} - \left[X_{i,A} \cdot \left(1 - \frac{n_{i,A}}{N_{i,A}} \right) \right] + \left(\sum_C X_{i,C} \cdot \frac{n_{i,C,A}}{N_{i,C}} \right). \tag{5.2.4}$$

where i is an integer between 1 and 6, and C corresponds to all morphological classes, excluding class A (e.g.: if A =spheroid, then C ={early-type disk, late-type disk, irregular}). Here $X_{i,A}$ and $X_{i,C}$ correspond to the number of galaxies of class A and C, respectively, observed in bin i.

Figure 5.2.2 plots the observed and corrected morphological counts for the sample of 157 galaxies in all redshift bins.

5.2.2 Results in CANDELS

This section presents the morphological fractions as a function of redshift observed in the CANDELS sample in the F160W band, and those corrected for the effect of CSBD with the first correction method. The analysis also includes a detailed investigation of the evolution of the morphological fractions over time of the star-forming and quiescent subsamples.

Figure 5.2.3 presents a plot of the observed and CSBD-corrected morphological fractions as a function of redshift for the CANDELS sample. The observed morphological fractions are shown as dashed lines, while the CSBD-corrected fractions are represented by solid lines. A first analysis reveals that the irregular galaxies exhibit the most notable variations. At redshift $z = 0.3-0.7$, the observed and corrected fractions are nearly identical, but the latter fraction is overestimated by a factor of four at $z = 2.25 - 2.75$. The CSBD correction significantly impacts the trend of irregular galaxies, which goes from decreasing in fraction from high- to low-redshift to increasing by approximately 20% from $z \sim 2.75$ to $z \sim 0.3$. The observed fraction of spheroids remains relatively constant throughout the redshift range, but according to our correction, it is overestimated by around 10%. The corrected fraction of early-type disks, on the other hand, decreases from approximately $\sim 40\%$ at $z = 2.75$ to $\sim 20\%$ at $z \sim 0.3$. The observed fraction of late-type disks increases steadily from $\sim 5\%$ at $z = 2.75$ to $\sim 40\%$ at $z \sim 0.3$, while the corrected fraction exhibits a less steep increase from approximately $\sim 30\%$ at high redshift to nearly 40% at $z \sim 0.3$. It is evident that CSBD has a significant impact on the observed morphological fractions, particularly at $z > 1.0$, and that this effect increases toward higher redshifts.

In order to analyze the morphological fractions of star-forming and quiescent galaxies separately, we implemented a division of the CANDELS sample into two distinct subsamples based on their star formation rate, as explained in Chapter 5.4. A total of 23,235 galaxies were classified as star-forming in this subsample, while the remaining galaxies were classified as quiescent, comprising 2,220 objects. It should be noted that we did not divide the parent sample into quiescent and star-forming galaxies to derive the correction terms for the two subsamples. This decision was primarily driven by the limited number of quiescent galaxies available, rendering the correction factors statistically unreliable.

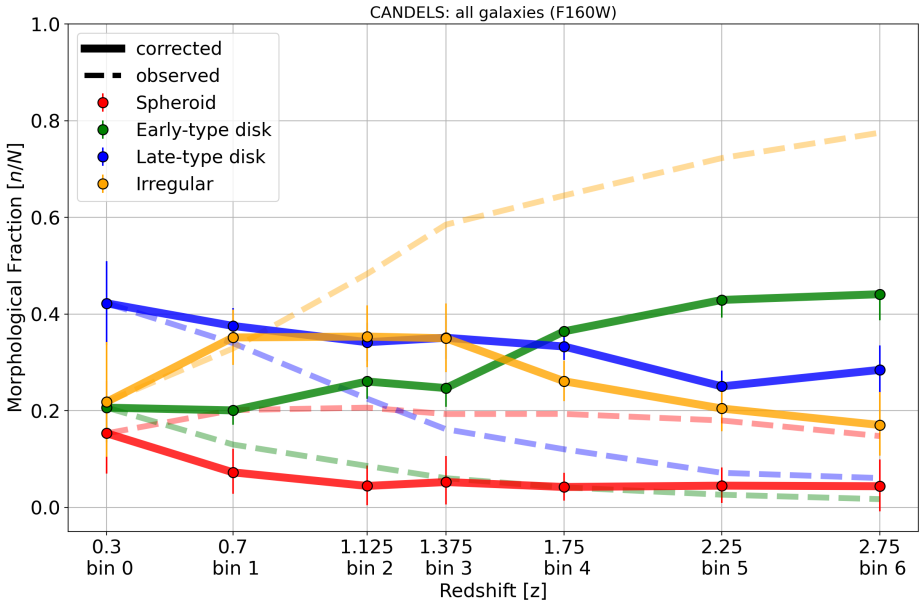

Figure 5.2.3: Morphological fractions in the CANDELS sample as a function of redshift. The observed morphological fractions are depicted by dashed and opaque lines, while the CSBD-corrected fractions are represented by solid lines. The influence of CSBD on the observed morphological fractions is clearly evident, indicating a significant impact on the interpretation of visual galaxy morphologies.

The results for star-forming and quiescent galaxies are presented in Figures 5.2.4 and 5.2.5, respectively. The observed and corrected morphological fractions of the star-forming subsample closely resemble those of the total CANDELS sample, both qualitatively and quantitatively. This is expected since the star-forming subsample constitutes about 84.39% in CANDELS at the redshifts considered in this work. In contrast, the quiescent subsample exhibits a distinct trend compared to that of the whole sample. Specifically, in the uncorrected sample, the dominant morphological class throughout all the considered redshift range is that of the spheroidal galaxies, with their fraction ranging from $\sim 30\%$ to $\sim 50\%$. After applying the CSBD correction, the fraction of spheroids does not exceed 20%, with a value lower than 10% at $z = 2.75$ and increasing to $\sim 20\%$ at $z \geq 0.7$. The early-type disk fraction displays an increasing trend, from $\sim 10\%$ at redshift ~ 2.75 to $\sim 40\%$ in the lowest redshift bin. However, after correcting for CSBD, early-type disks become the dominant class, with a relatively constant fraction of approximately $40 - 50\%$ across all redshifts. The morphological fractions of late-type disks show a trend similar to that of early-type disks, with an initially low

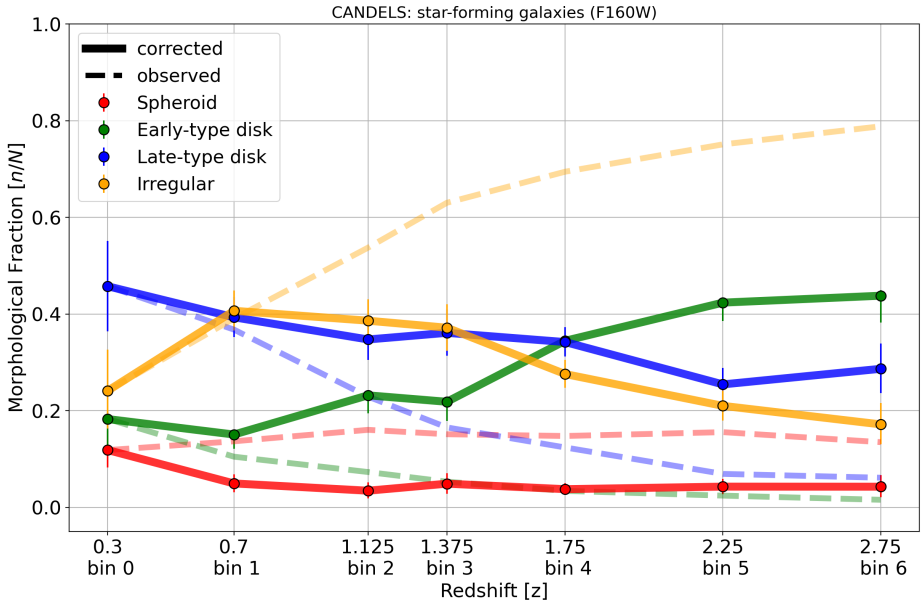

Figure 5.2.4: Same as Figure 5.2.3, but for the CANDELS star forming subsample.

uncorrected fraction, and a corrected fraction remaining close to approximately 30%. Finally, it can be observed that the fraction of irregular galaxies in the sample decreases from approximately 60% at $z \sim 2.75$ to nearly $\sim 0\%$ at $z \sim 0.3$, whereas after applying the correction, it remains relatively constant at less than 20% across all redshift bins.

5.2.3 Results in the Illustris-TNG50 simulation

The morphological classifications of the TNG-50 sample are obtained from Varma et al. (2022), who trained a CNN model on CANDELS-like mock images produced from the IllustrisTNG-50 simulation (see Chapter 4) to obtain morphological probabilities resembling visual classifications for six TNG50 snapshots.

The morphological fractions as a function of redshift in IllustrisTNG-50 are plotted in Figure 5.2.6. We compared the observed and corrected fractions of the TNG50 sample with those obtained from the CANDELS sample and found good agreement between them. Specifically, we observe that the fraction of irregular galaxies in the observed sample decreases from a dominant value of approximately 95% at $z = 3$ to $\sim 20\%$ at $z = 0.5$, while the corrected fraction increases from $\sim 20\%$ in bin 6 to $\sim 50\%$ at $z = 1.0$ and then decreases to $\sim 20\%$ in the lowest redshift bin.

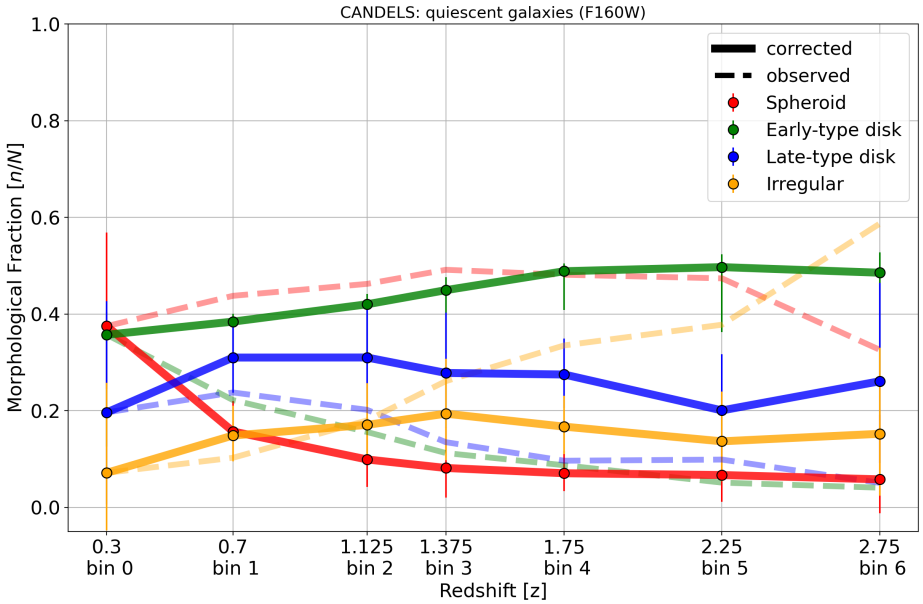

Figure 5.2.5: Same as Figure 5.2.3, but for the CANDELS quiescent subsample.

In the case of late-type disks, we find that the observed fraction is underestimated by up to 20%; the corrected fraction shows an increase of approximately 20% from high to low redshifts. On the other hand, early-type disks are almost absent in the observed fraction, but they are the dominant class at high redshift in the corrected fraction, decreasing from approximately 40% to approximately 20% from $z = 3$ to $z = 0.5$. Finally, we found that the corrected and uncorrected fractions of spheroids were very similar and remained at around 5% at all redshifts.

We further divided the TNG50 sample into quiescent and star-forming subsamples based on the criterion described in Chapter 5.4. The star-forming subsample in the TNG50 simulation comprises approximately 76.53% of the total sample. We observed in Figures 5.2.7 and 5.2.8, that the sat-forming subsample morphological fractions are similar to those of the whole sample. In contrast, the quiescent subsample reveals a consistent pattern wherein early-type disks maintain dominance across all redshift bins, comprising approximately 40% of the population. Conversely, the fraction of spheroids gradually rises until around $z \sim 1.125$, at which point their population undergoes a rapid increase to approximately 20%. Late-type disks and irregulars, on the other hand, exhibit a relatively stable fraction of approximately 25% and 15%, respectively, throughout the entire redshift range.

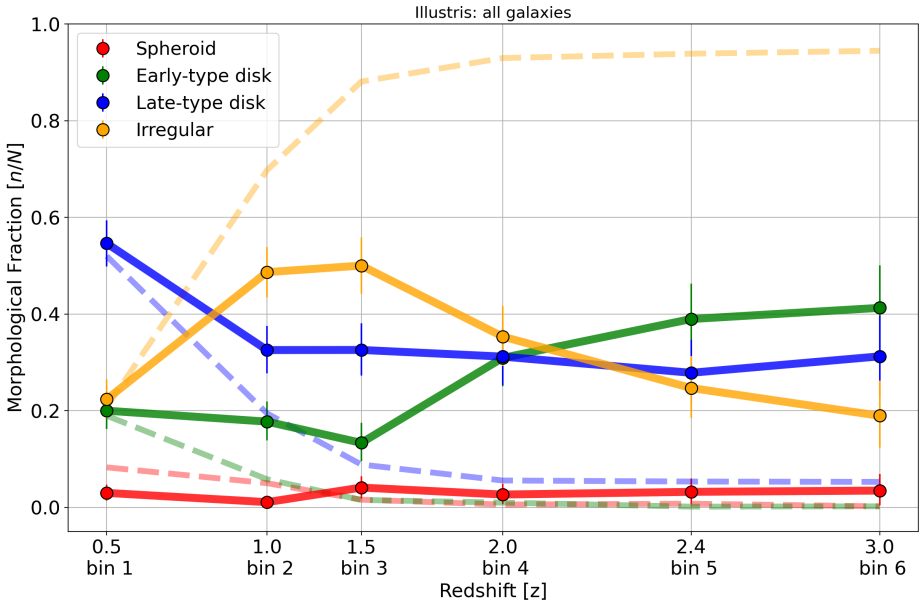

Figure 5.2.6: Morphological fractions in the TNG50 sample as a function of redshift. The observed morphological fractions are depicted by dashed and opaque lines, while the CSBD-corrected fractions are represented by solid lines. The effect of CSBD on the observed morphological fractions is just as significant as for the CANDELS sample.

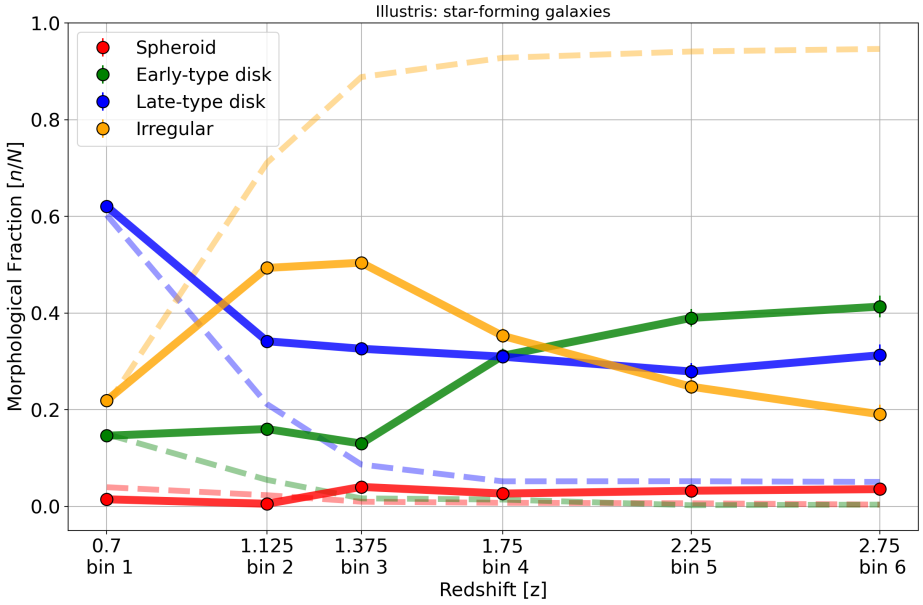

Figure 5.2.7: Same as Figure 5.2.6, but for the CANDELS star forming subsample.

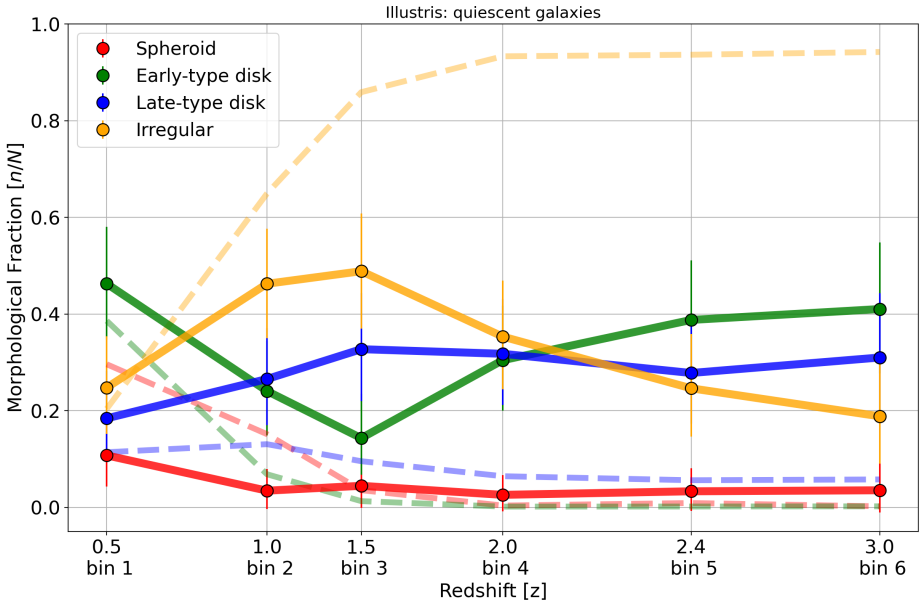

Figure 5.2.8: Same as Figure 5.2.6, but for the CANDELS quiescent subsample.

5.3 Second Method: Morphological Coefficients

In this section, we investigate the evolution of morphological fractions using the non-parametric coefficients to distinguish between different galaxy types.

5.3.1 Morphological Coefficients

The Gini coefficient and M_{20} are particularly useful for accurately measuring disturbances in galaxies with irregular morphologies that may not exhibit circular symmetry. As opposed to the CAS (concentration, asymmetry, and clumpiness) coefficients, which assume symmetry, G and M_{20} do not rely on any assumptions regarding the analytical form of a galaxy's light distribution (Lotz et al., 2004, 2008), making them well-suited for quantifying the morphology of disturbed galaxies or ongoing mergers. The morphological coefficients and their properties were discussed in Chapter 3.

In this study, we employed the *STATMORPH* Python package, developed by Rodriguez-Gomez et al. (2019), to compute the morphological coefficients of the 206 galaxies in both the parent and CANDELS samples. To run *STATMORPH*, we required a segmentation image of each galaxy, which was obtained by running

SExtractor (Bertin and Arnouts, 1996) on all the images. We also performed pre-processing of the input images for *STATMORPH* by removing nearby neighbors in both the science and segmentation images.

5.3.2 K-Correction

Up to this point, our analysis has neglected the influence of morphological K-correction (i.e. the change of galaxy appearance as a function of wavelength), as our focus was on determining the effects of CSBD. Nevertheless, in our second correction method, we have taken into account the effect of the morphological K-correction in estimating the morphological coefficients and, consequently, the morphological counts.

To achieve this, we redshifted the galaxies of the parent sample using different photometric bands, with each band selected to be the closest to the rest-frame in a specific redshift bin. Specifically, we used images in different photometric bands as input for *DOPTERIAN*, according to the desired simulated redshift bin. The filters used for each redshift bin are outlined in Table 5.3.1. It can be noted that not all CANDELS fields have the same set of optical filters.

Since the signal-to-noise ratio of the images decreases towards bluer wavelengths and higher redshifts, STATMORPH was able to determine the morphological coefficients up to bin 6 only for 60 objects. By extending the measurement of the morphological coefficients to a sample of 683 objects in all CANDELS at $0.2 \leq z < 0.4$, we were only able to increase the sample to 83 galaxies with coefficients estimated up to $z \sim 3$.

If we drop the requirement of considering the morphological K-correction, we end up having a larger sample, but the results on the variation of the morphological coefficients with redshift do not change significantly.

5.3.3 Determination of the CSBD correction for the Morphological Coefficients

After estimating the morphological coefficients G and M_{20} for both the original and simulated galaxies in the parent sample, we obtain 83 pairs of coefficients in bin 0 (G_0 and M_0) and 83 pairs in a higher redshift bin X (G_X and M_X). To simplify the notation, we denote M_{20} as M, and so $\Delta M = M_{20,bin0} - M_{20,binX}$.

	GOODS-S/GOODS-N	COSMOS/AEGIS/UDS
Bin 1 z=0.7	F775W	F814W
Bin 2 z=1.125	F606W	F606W
Bin 3 z=1.375	F606W	F606W
Bin 4 z=1.75	F435W	F606W
Bin 5 z=2.25	F435W	F606W
Bin 6 z=2.75	F435W	F606W

Table 5.3.1: The photometric band images used for each redshift bin determined based on the CANDELS field.

As represented in Figure 5.3.1, as the redshift increases, galaxies tend to shift toward lower values of G and higher values of M_{20}. This positional change arises due to the cosmological effects under investigation, namely the K-correction and the CSBD. Consequently, when estimating the morphological coefficients of galaxies at higher redshifts, we are obtaining biased values as a result of these effects. By exploiting the positional shift of objects in the parent sample within the $G - M_{20}$ plane as a function of redshift, we develop our second correction method.

We define the difference scalars $\Delta G = G_0 - G_X$ and $\Delta M = M_0 - M_X$, and introduce a correction vector $\vec{r} = (\Delta G, \Delta M)$, such that $(G_0, M_0) = (G_X, M_X) + \vec{r} = (G_X + \Delta G, M_X + \Delta M)$.

The available data provide us with 83 estimates of ΔG and ΔM. These differences are used along with the Bayes' theorem to construct a generative model that enables the determination of the most likely values of ΔG and ΔM for any given pair of measured coefficients G_j and M_j in a particular redshift bin.

The generative model is represented by the following probability distribution

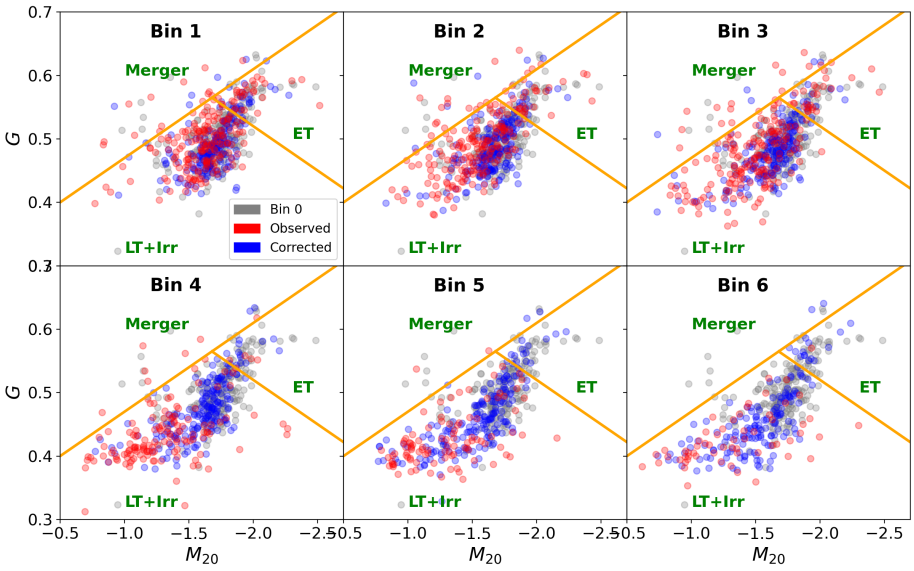

Figure 5.3.1: The distribution of parent sample galaxies within the $G - M_{20}$ plane. The coefficients obtained from the observed data are represented by the red color, while the corrected coefficients are depicted in blue, and the coefficients from the initial bin 0 are shown in gray. The orange lines displayed on the plot indicate the morphological geometric division defined by Lotz et al. (2008) for the $G - M_{20}$ plane. This visualization allows for a comparative analysis of the morphological properties of galaxies based on their positions within the $G - M_{20}$ parameter space.

function:

$$p(r|G_i, M_i) = p(\Delta G, \Delta M|G_i, M_i), \tag{5.3.1}$$
$$\propto p(G_i, M_i|r)p(r), \tag{5.3.2}$$
$$\propto p(G_i|M_i, \Delta G, \Delta M)p(M_i|\Delta M)p(\Delta G, \Delta M), \tag{5.3.3}$$
$$\propto p(G_i|M_i, \Delta G, \Delta M)p(M_i|\Delta M)p(\Delta G)p(\Delta M), \tag{5.3.4}$$

where we have assumed that:

1. G_i is linearly dependent on M_i as:

$$G_i = \alpha + \beta \cdot M_i. \tag{5.3.5}$$

2. M_i is the independent variable.

3. ΔG and ΔM are correlated (see Figure 5.3.2).

We assume that the likelihood term $p(G_i|M_i, \Delta G, \Delta M)$ follows a normal distribution, $N(\mu_l, \sigma_l)$, with parameters:

$$\mu_l = G_i - \alpha - \beta M_i - \Delta G - \beta \Delta M, \tag{5.3.6}$$

and with σ_l being the variance obtained by fitting a Gaussian to the distribution of ΔG. The term $p(M_i|\Delta M)$ follows a normal distribution, $N(\mu_m, \sigma_m)$, with parameters:

$$\mu_m = M_i - \Delta M, \tag{5.3.7}$$

and with σ_m being the variance obtained by fitting a Gaussian to the distribution of ΔM. Finally, each of the prior probabilities $p(\Delta G)$ and $p(\Delta M)$ is assumed to be Gaussian where the parameters are the best fit to the observed distribution of each parameter in each bin.

Two important points should be noted. Firstly, the probability distribution that we seek is conditioned on the values of the unique α and β parameters for each redshift bin, as well as on the observed coefficients. Secondly, it is assumed that all terms in equation 5.3.4 follow a normal distribution.

Note that 83 galaxy is not a large sample, specially when compared to the CANDELS sample. Thus, we re-calculated the morphological coefficients for the

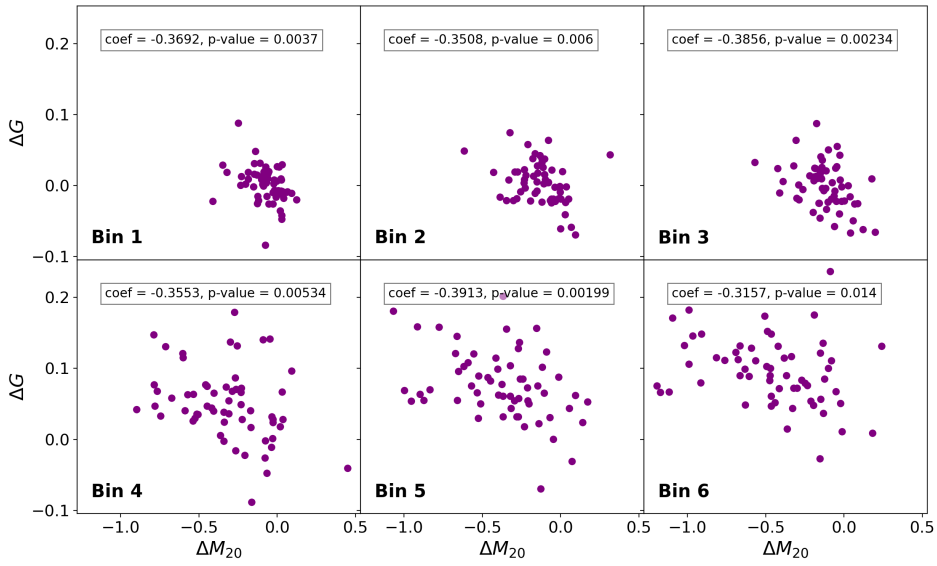

Figure 5.3.2: Spearman correlation test conducted to assess the relationship between the variables ΔG and ΔM. The results indicate a significant correlation between these two variables.

683 galaxy sample but only using the F160W band, i.e. without considering the morphological K-correction effect. We were able to increase our sample to 226 galaxies. We further compared the estimated and corrected morphological coefficients of the galaxies that are both in the original 60-galaxy sample and the new 226-galaxy sample, and found no major differences. We therefore proceed our analysis considering the 83-galaxy sample, since this sample accounts for the effects of both CSBD and K-correction.

To determine the values of ΔM and ΔG that maximize the probability distribution expressed by equation 5.3.4 for a specific pair of observed coefficients G_j and M_j, we employ a gradient descent algorithm. After obtaining the optimal values of ΔG and ΔM, we add them to the observed coefficients G_j and M_j, respectively, to obtain the morphological coefficients that are free from the CSBD bias. The median values for ΔG and ΔM_{20} are presented in Table 5.3.2. The influence of the correction process on the coefficients of the parent sample can be clearly observed in Figure 5.3.1. The corrected coefficients, represented by the blue dots, tend to resemble the coefficients of bin 0 more closely compared to the uncorrected estimated coefficients, plotted as red dots.

Bin	Redshift	Median G	Median M_{20}	Median ΔG	Median ΔM_{20}
0	0.3	$0.518^{0.051}_{0.044}$	$-1.818^{0.162}_{0.215}$	-	-
1	0.7	$0.509^{0.057}_{0.054}$	$-1.621^{0.303}_{0.305}$	$-0.004^{0.008}_{0.008}$	$-0.256^{0.038}_{0.044}$
2	1.125	$0.482^{0.057}_{0.048}$	$-1.387^{0.349}_{0.319}$	$-0.008^{0.01}_{0.01}$	$-0.378^{0.07}_{0.063}$
3	1.375	$0.471^{0.059}_{0.046}$	$-1.329^{0.352}_{0.324}$	$-0.011^{0.01}_{0.011}$	$-0.347^{0.068}_{0.061}$
4	1.75	$0.474^{0.058}_{0.048}$	$-1.326^{0.359}_{0.312}$	$0.007^{0.02}_{0.019}$	$-0.68^{0.149}_{0.126}$
5	2.25	$0.484^{0.055}_{0.054}$	$-1.336^{0.356}_{0.309}$	$0.029^{0.024}_{0.021}$	$-0.796^{0.183}_{0.149}$
6	2.75	$0.481^{0.058}_{0.052}$	$-1.331^{0.345}_{0.306}$	$0.045^{0.026}_{0.021}$	$-0.781^{0.178}_{0.143}$

Table 5.3.2: Median values of G, M_{20}, ΔG and ΔM_{20} for every redshift bin in the CANDELS sample.

5.3.4 Morphological Labels from Morphological Coefficients

The $G - M_{20}$ diagram provides a continuous distribution of galaxies, thereby morphological coefficients provide information beyond a discrete morphology assignment. This diagram shows a majority of galaxies distributed along a main sequence, representing a continuum of morphologies that span the transition from disk-dominated to spheroidal structures (Sazonova et al., 2020). However, in order to differentiate the $G - M_{20}$ plane into three distinct regions corresponding to early-type (E-S0-Sa), late-type (Sb-Irr), and merger morphologies, Lotz et al. (2008) introduced the following criterion:

- Mergers: $G > -0.14M_{20} + 0.33$.
- E/S0/Sa: $G \leq -0.14M_{20} + 0.33$ and $G > 0.14M_{20} + 0.8$.
- Sb-Irr: $G \leq -0.14M_{20} + 0.33$ and $G \leq 0.14M_{20} + 0.8$.

Nevertheless, the morphological classification introduced by Lotz et al. (2008) was developed for a low-redshift sample ($0.05 < z < 0.25$). Therefore, if morphological coefficients evolve with redshift, this classification criterion may not be applicable even if one uses CSBD-corrected values.

To address this issue, we adopt the methodology of Sazonova et al. (2020), who employed Principal Component Analysis (PCA) to identify the main sequence of the $G - M_{20}$ diagram. The first principal component (PC1) is used to capture the highest amount of variance in the data and is aligned with the main sequence, while the second principal component (PC2) measures the distance perpendicular to it. PC1 is then correlated with the Gini coefficient. Galaxies with high Gini coefficients have a high concentration of light in their central regions, indicating

the presence of a prominent bulge. Additionally, PC1 is negatively correlated with the M_{20} coefficient. Galaxies with high M_{20} values are more likely to have a disrupted or irregular morphology, which is associated with disk-dominated systems. Thus, by combining information from both G and M_{20}, one can deduce that PC1 provides a robust measure of the bulge strength of a galaxy. On the other hand, galaxies located above the $G - M_{20}$ main sequence (with high values of G and M_{20}) are likely perturbed systems undergoing mergers, while galaxies lying below the main sequence (those with low values of G and M_{20}) are of diffuse or unresolved types. Therefore, PC2 provides a measure of the level of disturbance of a galaxy.

In Sazonova et al. (2020) galaxies were defined as having high bulge dominance if $PC1 > 1$ and as highly disturbed if $PC2 > 1$. To further investigate the relationship between PC1 and the bulge-to-total (B/T) ratio, we performed a Spearman correlation test on galaxies in the CANDELS dataset. Our analysis revealed a significant negative correlation between the two variables, as can be seen in Figure 5.3.2. Based on these results, we established the following classification criterion:

- **Spheroid:** if $PC2 \leq 1$ and $PC1 \geq 1$ and $B/T \geq 0.8$.
- **Early-type disk:** if $PC2 < 1$ and $-1 \leq PC1 < 1$ and $0.2 < B/T < 0.8$.
- **Late-type disk:** if $PC2 < 1$ and $PC1 < -1$ and $B/T \leq 0.2$.
- **Irregular:** if $PC2 \geq 1$ and $0 \leq BT \leq 1$.

Hence, we differentiate spheroids, early-type disks, and late-type according to the dominance of their bulge and identify a galaxy as irregular if it displays high levels of perturbation, regardless of its B/T value. The evolution of the $PC1 - PC2$ parameter space is shown in Figure 5.3.3.

The classification criterion based on the Sazonova et al. (2020) approach is based on relative distances (between each object and the $G - M_{20}$ main sequence), while the Lotz et al. (2008) criterion uses fixed limits, which have been proven not to hold at $z \sim 0.6$ (Deger et al., 2018). Since the Sazonova et al. (2020) criterion only takes into account the position and scatter of the $G - M_{20}$ main sequence, which may change with redshift, we decided to employ it in our study of morphology as a function of redshift.

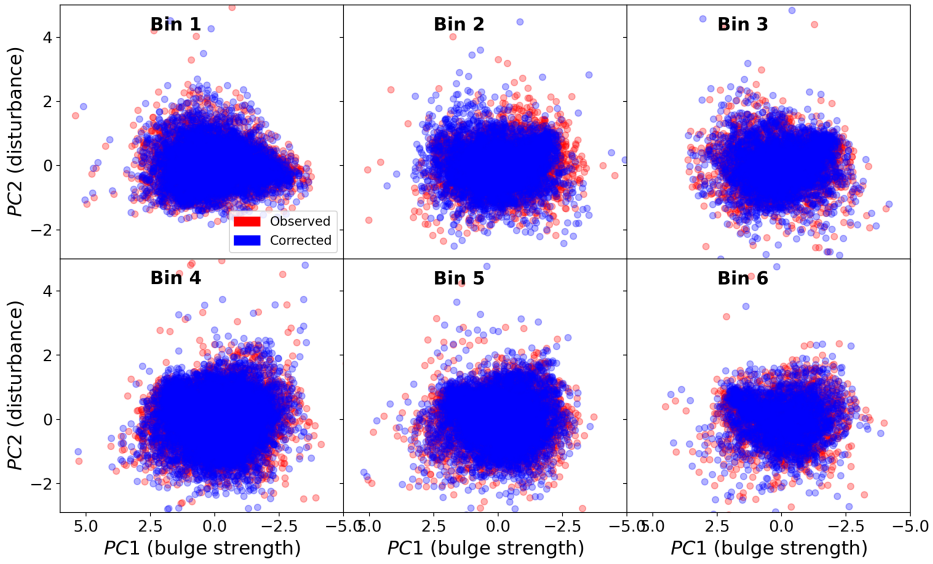

Figure 5.3.3: The PCA parameter space which illustrates the distribution of the CANDELS sample, both corrected and uncorrected. The x-axis represents the first principal component ($PC1$), which is associated with the strength of the galactic bulge. On the other hand, the y-axis corresponds to the second principal component ($PC2$) and represents the degree of disturbance or perturbation exhibited by each galaxy.

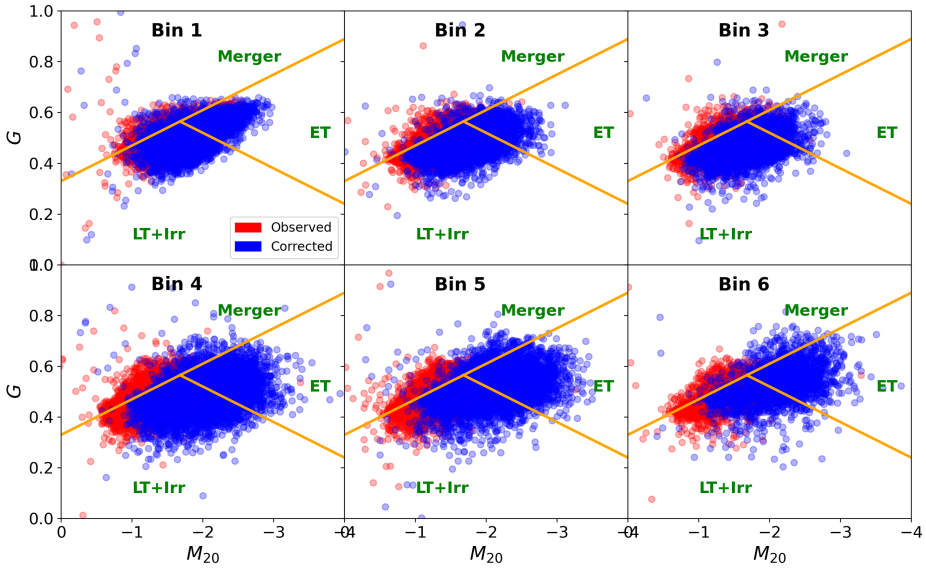

Figure 5.3.4: The $G - M_{20}$ plane for the observed (red) and corrected (blue) morphological coefficients of the galaxies in the CANDELS sample. Orange lines represent the geometric morphological division from Lotz et al. (2008).

In order to guarantee equal weighting of the G and M_{20} parameters during the Principal Component Analysis (PCA), a normalization of these coefficients is necessary to set them on the same scale. The normalization process involves computing the mean and variance of the distribution of each parameter in each bin. From each measurement, the sample mean is subtracted and the result is divided by the variance, resulting in a normalized data set.

5.3.5 Results in CANDELS

We now present the morphological fractions using the second CSBD-correction method and the classification criterion described in the previous sections. Figure 5.3.4 illustrates the application of the second correction method to the CANDELS sample. It is noteworthy that the corrected coefficients tend to exhibit smaller values of M_{20} and larger values of the G. As it was mentioned earlier, the observed values of G decreased with redshift while those of M_{20} increased. So this indicates that the second correction method successfully shifts the galaxies toward the expected location of the unbiased coefficients. This is represented in Figure 5.3.5.

We now present the morphological fractions as a function of redshift and stellar

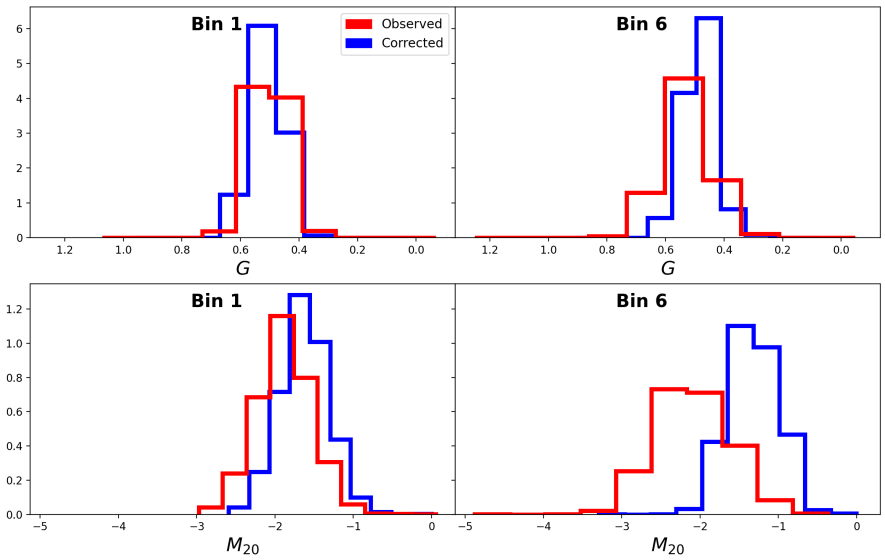

Figure 5.3.5: Distributions of observed (red) and corrected (blue) morphological coefficients G (top panels) and M_{20} (bottom panels), for bin 1 and bin 6, within the CANDELS sample. It is worth noting that in bin 1, the corrected and uncorrected distributions appear similar, indicating that cosmological effects can still be disregarded. However, in bin 6, a noticeable difference between these coefficients is evident, with the corrected coefficients exhibiting higher values of M_{20} and lower values of G.

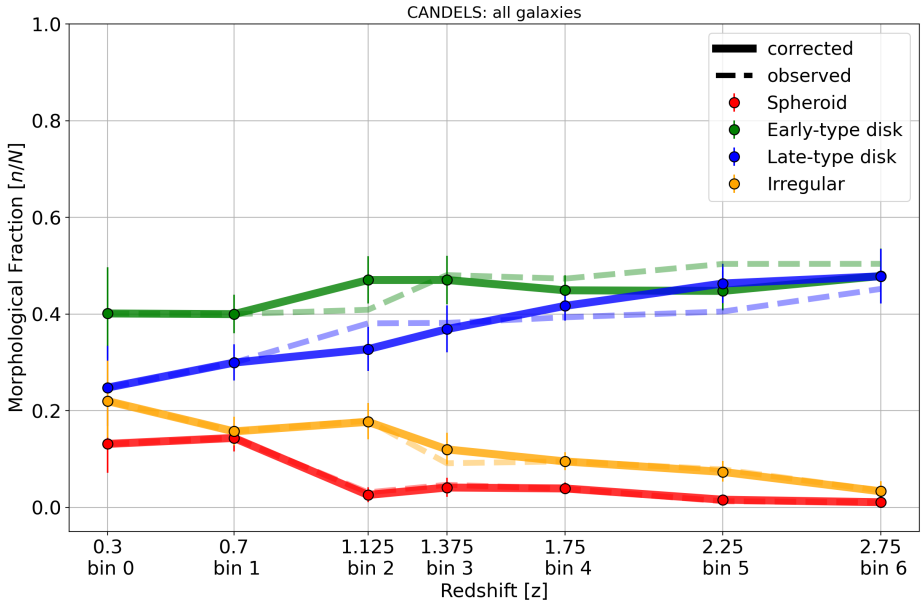

Figure 5.3.6: Morphological fractions in the CANDELS sample estimated using the G-M_{20} plane as a function of redshift. The observed fractions are depicted with dashed lines, while the corrected fractions are represented with solid lines. It can be seen that the difference between observed and corrected fractions is little.

mass obtained with the morphological coefficient classification method, as well as an analysis of the median of the distribution of some coefficients.

Results from Figure 5.3.6 show that early-type disks have a mostly constant fraction at $\sim 40\%$ at all redshifts. Late-type disks, on the other hand, decrease their fraction from $\sim 45\%$ at $z \sim 2.75$ to $z \sim 25\%$ at ~ 0.3. Also, irregulars and spheroids increase their fraction from about $\sim 5\%$ at $z \sim 2.75$ to $\sim 20\%$ at the lowest redshift bin, whit irregular fraction growing progressively and the spheroid fraction have a steeper slope at $z < 1.125$. One of the most important results concerning the corrected morphological fractions is the absence of a significant difference between the observed and corrected fractions, unlike what was obtained with the first correction method. We will dive into this discrepancy between both outcomes in the discussion chapter.

In Figures 5.3.7 and 5.3.8, we present the uncorrected and corrected morphological fractions for the star-forming and quiescent subsamples. As observed, both the corrected and uncorrected morphological fractions of the star-forming subsample resemble the fractions of the entire sample, as a result of the larger population of

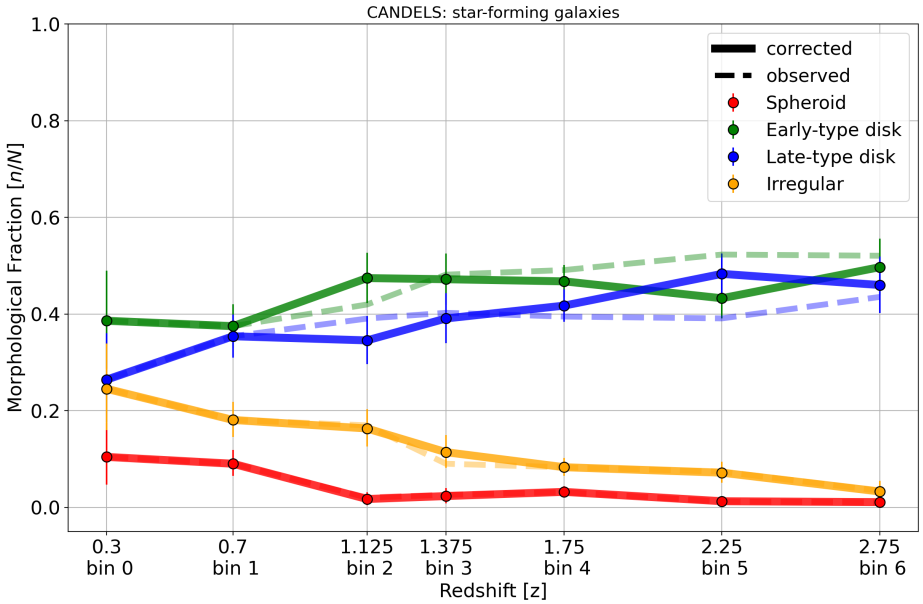

Figure 5.3.7: Same as Figure 5.3.6 but for the star-forming subsample.

star-forming galaxies in CANDELS.

When analyzing the quiescent subsample we see a striking decrease in the fraction of late-type disks, from $\sim$ 75% at $z \sim 2.75$ to $\sim$ 20% at $z \sim 0.4$. Early-type disks and irregulars have a constant fraction of $\sim$ 50% and $\sim$ 15%, respectively, trough out all redshift bins. Finally, spheroids increase their fraction from almost $\sim$ 0% at the highest redshift bin to $\sim$ 30% at $z \sim 0.3$ These trends suggest that galaxies with a larger bulge component tend to dominate the quiescent sample at low redshift, in agreement with the scenario in which galaxies grow their bulge over time.

As the visual-like correction method is only correcting morphological counts, we lose information about the stellar mass distribution of each morphological class. On the other hand, the morphological coefficient-correction method does not suffer this loss of information because the classification is made after the correction of the coefficients. We can then only derive corrections for the types defined in the $G - M_{20}$ plane as a function of stellar mass. The results are presented in Figure 5.3.9.

It can be seen that there is trend in which spheroids, a morphological class that corresponds to a high bulge fraction, tend to occupy the heavy end of the

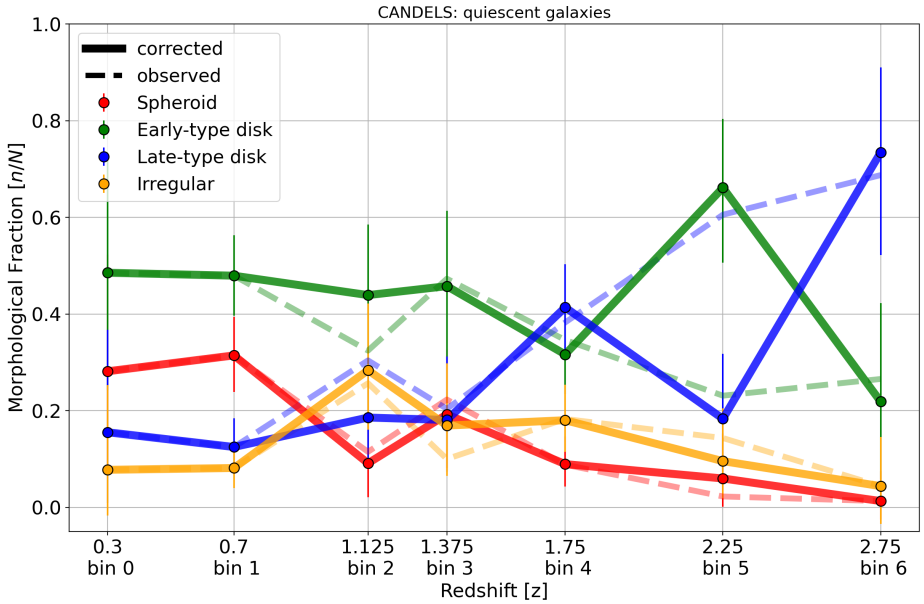

Figure 5.3.8: Same as Figure 5.3.6 but for the quiescent subsample.

stellar mass ranges. Notably, the fraction of high-mass spheroids increases at lower redshifts, suggesting that their mass is built up over cosmic time, likely through dry-minor or major mergers (Lidman et al., 2013; Ownsworth et al., 2014; Rodriguez-Gomez et al., 2016). While the there are less massive late-type disks toward lower redshift, there is a transition in the morphological fraction as a function of stellar mass for the early-type disks class, where most early-type disk are in the lowest mass bins at high redshift, but the most populated mass bins at low-redshift ($z < 1.375$) are those of highest mass. Late-type disks populate the low stellar mass bins as at redshift (except for bin 6). We also find weak evidence for irregular galaxies populating low-stellar mass bins toward lower redshifts.

Figures 5.3.10 and 5.3.11 show the morphological fractions as a function of mass for the star-forming and quiescent galaxies, respectively. We find no significant difference between the whole sample morphological fractions as a function of stellar mass and that of the star-forming sample. For the quiescent subsample we note that, broadly speaking, both spheroids and early-type disks increase their population in all stellar mass bins. Similarly to the star-forming fractions, late-type disks dominate the low-end of the stellar mass function and irregulars also do not show any particular trend with redshift or mass.

Although the morphological classifications derived using the G-M_{20} plane should

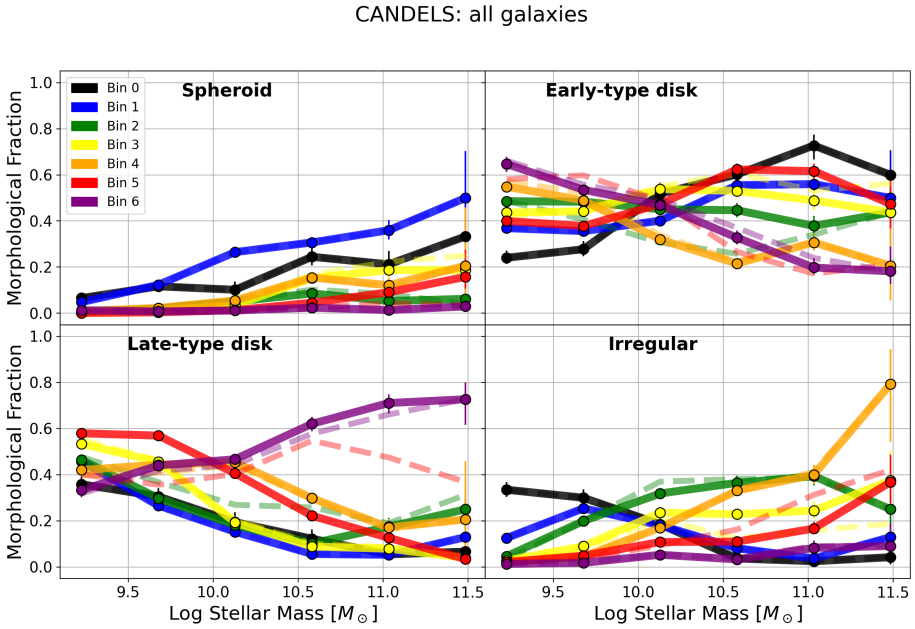

Figure 5.3.9: The morphological fractions as a function of the logarithm of stellar mass in the CANDELS sample are presented in different panels, each representing a distinct morphological type. The redshift evolution of the morphological fractions is depicted by displaying the fractions of each redshift bin using different colors. The morphology in these plots is defined according to the location of galaxies in the G-M_{20} plane.

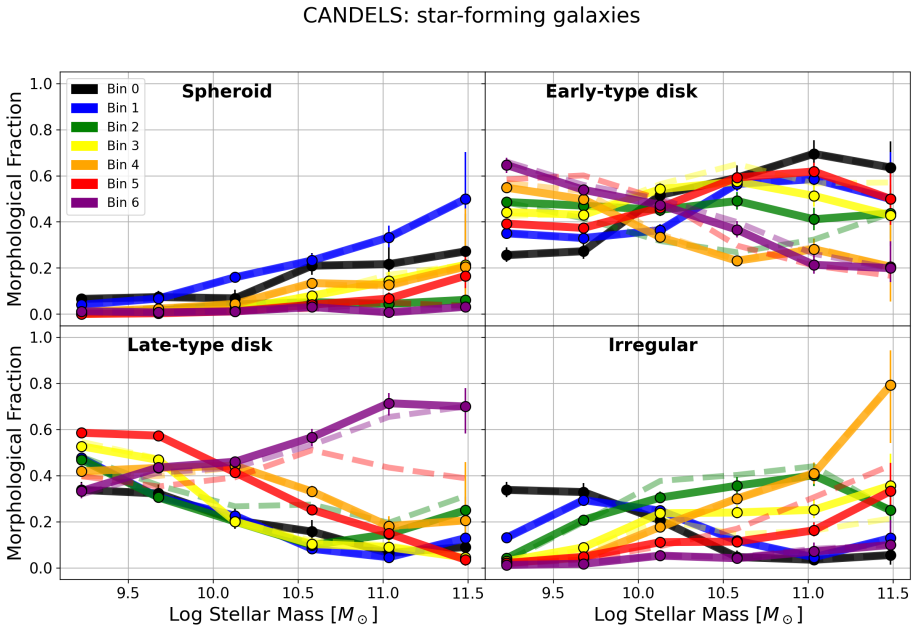

Figure 5.3.10: Same as Figure 5.3.9 but for the star forming subsample.

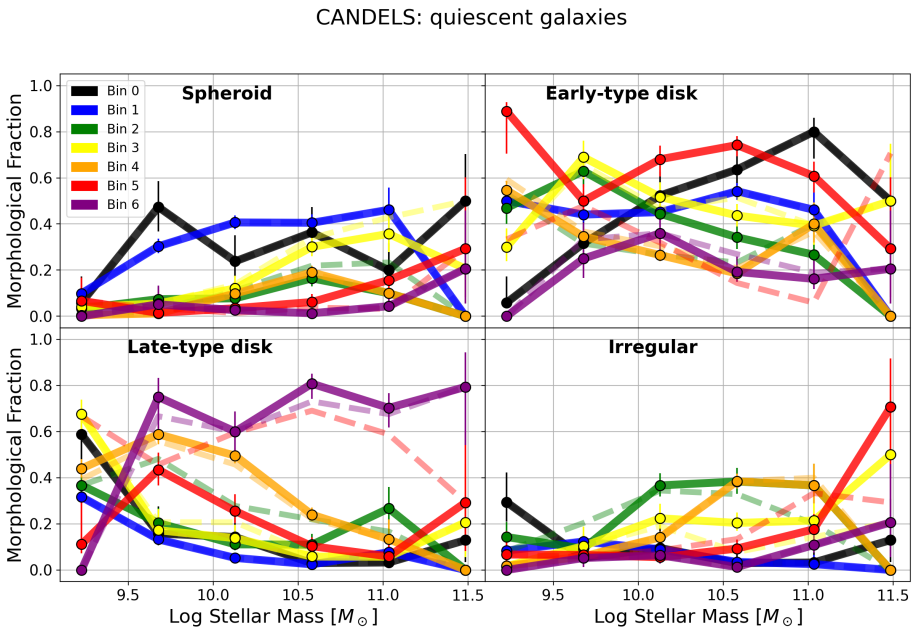

Figure 5.3.11: Same as Figure 5.3.9 but for the quiescent subsample.

be taken into account with the previously mentioned caveats, the corrections that we have derived provide us with useful information about the light distribution of the galaxies in our sample. Figure 5.3.12 displays the median and the 1σ widths of the distributions of G, M_{20}, shape asymmetry, and half-light radius as a function of redshift. It can be observed that, in general, as the redshift increases, G and the half-light radius decrease and, as a result of that, galaxies may appear fainter and smaller. Conversely, M_{20} and the shape-asymmetry increase, suggesting a clumpier and more asymmetric appearance for high redshift objects.

Although these results may explain why galaxies tend to be misidentified as irregular galaxies at higher redshifts when visually inspected, and thus the results obtained from the corrected morphological fractions derived with visual inspection, the observed and corrected median values of G and M_{20} fall within the uncertainty range, indicating that the difference is not statistically significant. Further elaboration on this topic will be provided in the discussion chapter.

5.3.6 Results in the Illustris-TNG50 Simulation

In this section, we present the morphological fractions of the TNG50 sample. We used the morphological coefficients estimated in the HST-like images of TNG50 simulated galaxies published in Snyder et al. (2017).

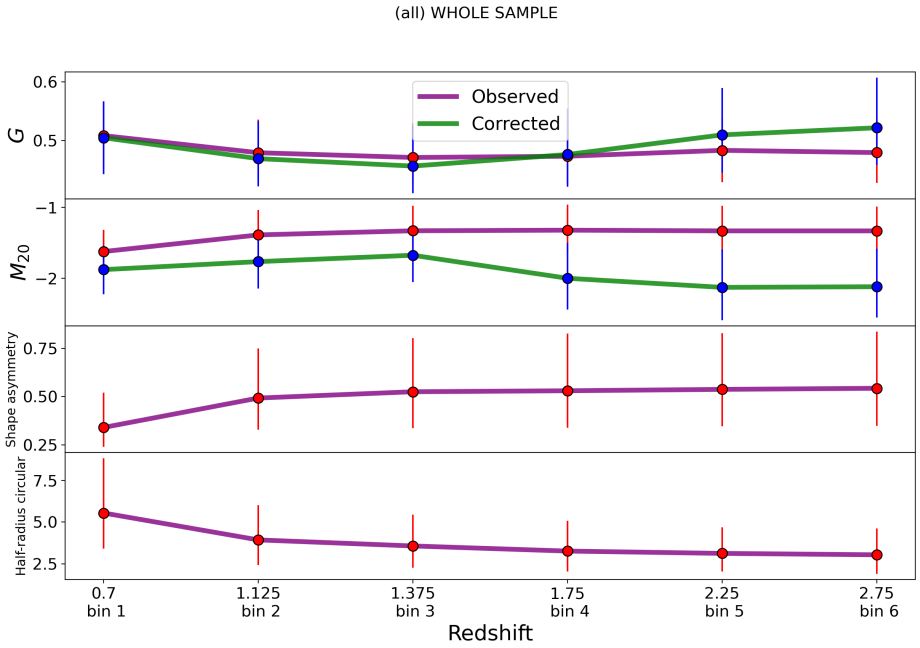

Figure 5.3.12: The median values and the 1σ width of the observed G, M_{20}, shape asymmetry and half-light radius are displayed in the top to bottom panels, respectively. The median of the corrected G and M_{20} values are shown as green lines.

We observe in Figure 5.3.13 that the early-type disks constitute the dominant class across all redshift bins. Their fraction remains almost constant at $\sim 70\%$. Conversely, late-type disks, irregulars and spheroids exhibit a roughly constant fraction of $\sim 15\%$ throughout the entire redshift range.

The trends of the morphological fractions as a function of stellar mass, represented in Figure 5.3.14, are considerably more intricate than those observed with the visual classification. In the TNG50 sample there appears to be no discernible evolutionary trend in the fractions as a function of stellar mass across different redshifts for spheroids, late-type disks and irregulars. However, it is remarkable that early-type disks start to populate higher stellar mass ($M_* > 10^{10} M_\odot$) bins toward lower redshifts, implying a positive mass evolution for early-type disks.

We also looked at the trends of the star-forming and quiescent subsamples; however, we find inconclusive results and a large scatter in both subsamples.

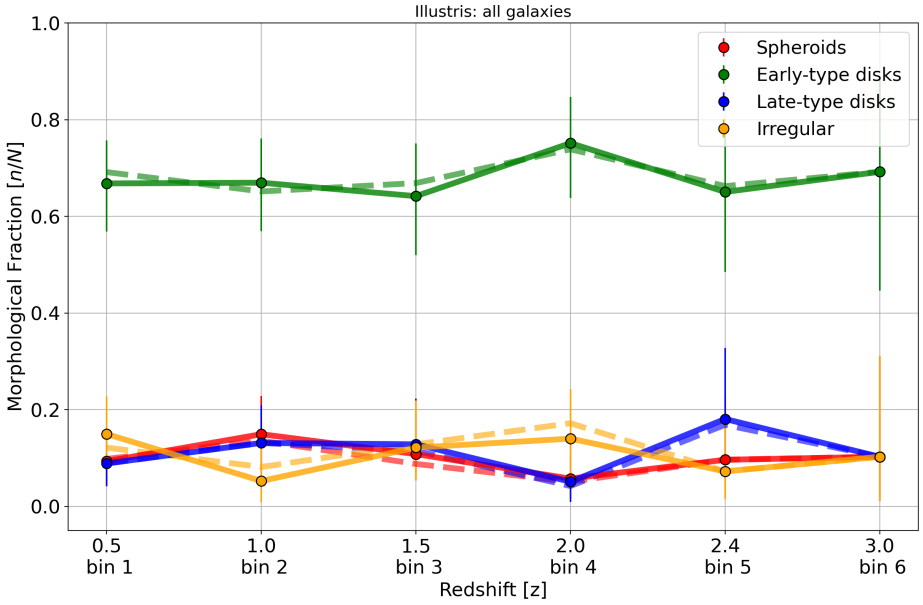

Figure 5.3.13: The morphological fractions of the TNG50 sample, estimated using the morphological coefficients method, as a function of redshift. The observed and corrected fractions are shown in dashed lines and solid lines, respectively. The observed and corrected morphological fractions again exhibit a high degree of similarity.

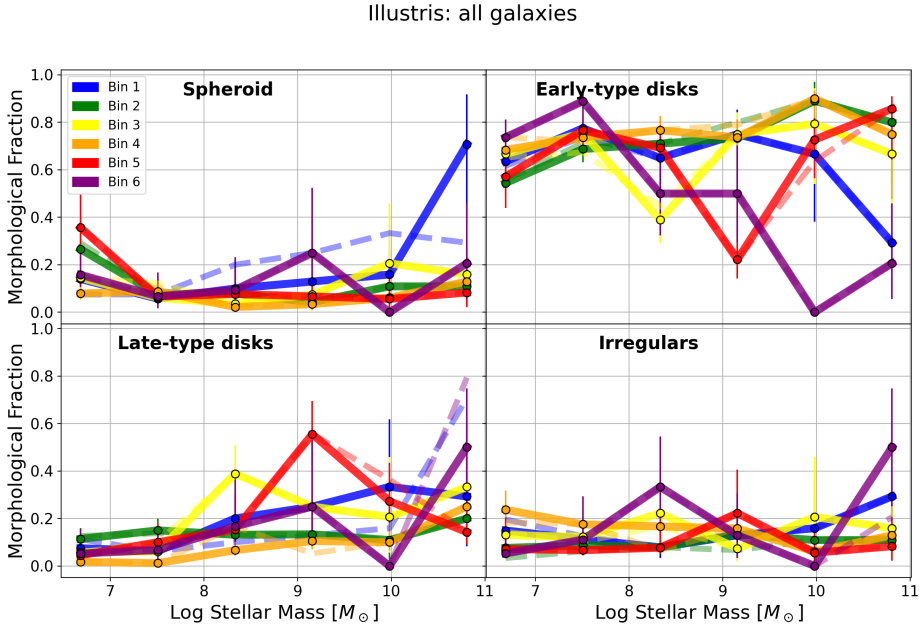

Figure 5.3.14: Morphological fractions as a function of the logarithm of stellar mass in the TNG50 sample, calculated with morphological coefficients method. Each panel represents a particular morphological type. The morphological fraction as a function of stellar mass for every redshift bin are shown in different colors.

Chapter 6

Discussion

6.1 The Effects of Cosmological Surface Brightness Dimming on Morphological Classifications

The comparison between the observed and CSBD-corrected morphological fractions in CANDELS and Illustris show that CSBD introduces a significant bias in the visual morphological classification of galaxies. Figure 6.1.1 illustrates the difference between observed and corrected morphological fractions in the CANDELS sample. The fractions of irregular and spheroidal galaxies are overestimated, where spheroids exhibit a consistent but slightly lower overestimation of approximately 20%, while irregular galaxies are greatly overestimated, reaching up to 60% at high redshifts and gradually declining to nearly 0% in the lowest redshift bin. On the other hand, both observed late-type and early-type disks are underestimated by up to 40%. The overestimation or underestimation of these fractions becomes significant at $z \geq 1$, suggesting that CSBD plays a progressively more important role beyond this redshift in morphological measurements.

We also find that for a given redshift bin, high-stellar mass ($M_* \geq 10^{10} M_\odot$) spheroids are more prone to overestimation, whereas low-stellar mass ($M_* < 10^{10} M_\odot$) irregular galaxies tend to be more overestimated, when compared to the whole sample. However, for early- and late-type disks, the magnitude of the effect of CSBD seems to have little dependence on stellar mass. This suggest that CSBD effect is stellar mass dependent only for spheroids and irregular galaxies.

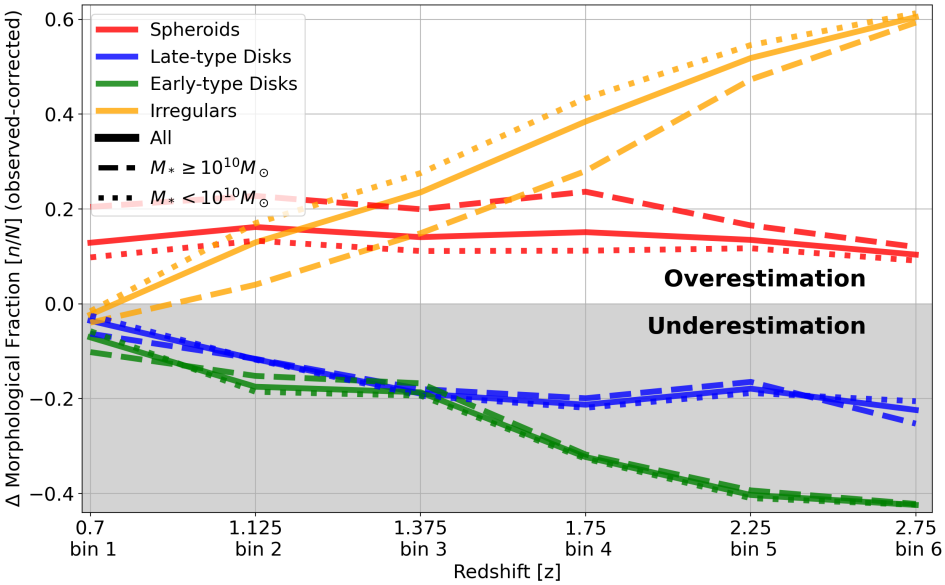

Figure 6.1.1: Amount of over/underestimation of the observed morphological fractions in the CANDELS sample for each morphological type, as a function of redshift. Dotted, dashed and solid lines represent the low-stellar mass sample ($M_* < 10^{10} M_\odot$), high-stellar mass sample ($M_* \geq 10^{10} M_\odot$) and the whole sample, respectively. The y-axis represents the difference between the observed and corrected fractions. In this context, the light-gray region corresponds to an underestimation of the observed morphological fractions, while the white area indicates the overestimation zone. Notably, the differences between the observed and corrected fractions increases with redshift, with the exception of the spheroid class.

One of the main highlights we have found regarding the effect of CSBD on morphological classification is that it is a significant source of confusion for visual classifications but not for coefficient-based morphological classification, as the corrected and uncorrected morphological fractions obtained with the second correction method do not vary significantly. We argue that this is a result of the fact that the original and the artificially redshifted galaxies that appear different in visual classification may, in fact, have similar morphological coefficients.

When artificially degrading a galaxy image, we modify its surface brightness and its pixel scale. The Gini coefficient is sensitive to the cumulative distribution of the flux of the galaxy pixels, while M_{20} is sensitive to the width of the light distribution among the pixels. The degradation factor of $(1+z)^{-4}$ can be understood as a simple multiplication of the pixels flux values by a constant. Consequently, we expect that the changes in the cumulative pixel distribution and the width of the light distribution not to be significant. However, after degradation, the values of the G and M_{20} coefficients may be affected when the pixel flux values fall below the source detection threshold, i.e. equal to or lower than those of the sky background. In such cases, the pixels are no longer within the detection area, resulting in changes in the values of the least bright pixels of the galaxy and consequently affecting the values of the coefficients.

Figure 6.1.2 shows the changes in visual appearance and the estimated morphological coefficients between bin 0 ($z \sim 0.3$) and bin 6 ($z \sim 2.75$) for an spheroid, a late-type disk and an irregular galaxy from the parent sample. Notice how there is a noticeable change in visual appearance with redshift (e.g. the evident spiral arms and the irregular shape for the late-type disk and the irregular galaxy, respectively, in bin 0 disappear completely by bin 6) but a only small change in morphological coefficients. This suggests that changes in morphological coefficients due to the change in pixel scale and pixels falling below the detection threshold are not significant, and that the human eye is unable to distinguish the light distribution when the pixel flux is comparable to the sky noise. This explains why coefficients G and M_{20} do not change significantly in value, despite the significant visual difference perceived by the human eye. On the other hand, the shape asymmetry coefficient exhibits the highest variation as its value depends on the segmentation image, which does vary due to the increased likelihood of confusion between parts of the galaxy and the sky.

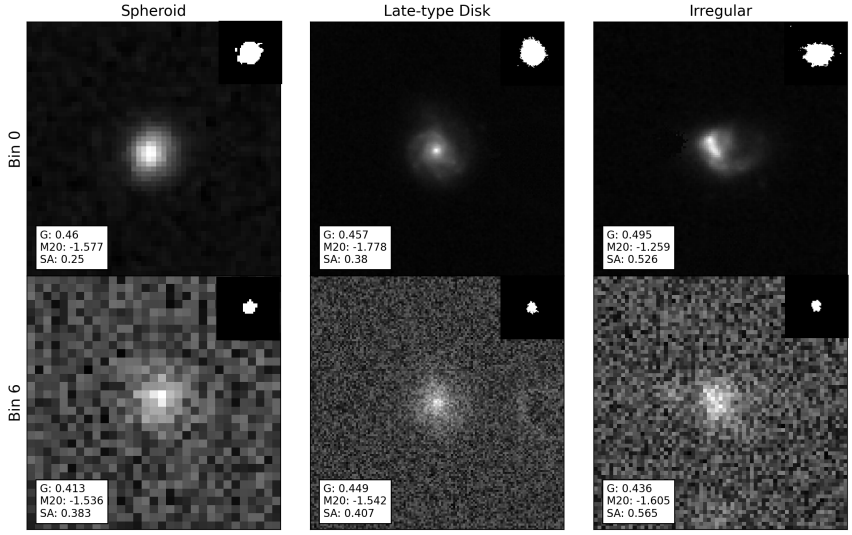

Figure 6.1.2: Example of the change of visual appearance and the value of morphological coefficients with redshift. Top row shows the image of three galaxies of the parent sample at bin 0, while bottom row shows the same galaxies artificially redshifted to bin 6 ($z \sim 2.75$). Each panel shows the morphological coefficients estimated for that galaxy in the bottom left corner and its segmentation image in the top right corner. Notice how, despite the great change in visual appearance of all galaxies, the morphological coefficients do not vary significantly.

The analysis of Figure 5.3.12 reveals that galaxies at high redshifts display a combination of characteristics: higher M_{20} and asymmetry values, smaller effective radii, and a decrease in the Gini coefficient. This combination suggests that some of these galaxies may appear smaller and fainter when compared to galaxies at low redshifts, resembling low-mass elliptical galaxies. Other galaxies may have lower values of G and higher shape asymmetry due to the presence of sub-structures (such as disordered spiral arms and tidal tails) or a stronger confusion between galaxy pixels and background pixels, and thus may have a less concentrated light distribution, resembling an irregular galaxy. However, it is important to note that the evolutionary trends of both the observed and corrected median values of G and M_{20} fall within the range of uncertainties. Therefore, the slight changes in the median values of these coefficients with redshift are not statistically significant. Nevertheless, we have also discussed the existence of a notable visual morphological change that does not correspond to a significant change in the morphological coefficients. This suggests that the human eye tends to *"exaggerate"* the small evolutionary trend of the morphological coefficients, i.e. CSBD and noise make galaxies at higher redshift look either rounder and fainter or asymmetric and fainter to the human eye.

Therefore, based on the information provided by Figures 5.2.1, 6.1.1 and 5.3.12, we propose two confusion channels to explain these results. Regardless of their true morphology, galaxies tend to be visually misclassified as spheroids or irregulars. Galaxies can be mistaken for spheroids because the observed surface brightness of extended structural features, such as the disk, may fall below the sky level and consequently not be discerned during the visual inspection. This leads an observer to classify a galaxy as spheroid. On the other hand, galaxies could be misclassified as irregular galaxies because they appear fainter and asymmetric.

A recent study by Margalef-Bentabol et al. (2022) does address the correction for CSBD in a CANDELS sample using Galaxy Zoo classifications and a decision tree algorithm. They found that the corrected fraction of spirals increases by a factor of 10 when going from $z = 2.5$ to $z = 0.5$. The fraction of spirals shows a rapid increase below $z \sim 1.5$, but the corrected fraction exhibits a shallower behavior that is more similar to our results. With the visual-like classification we found that, as seen in Figure 6.1.1, the corrected fraction of spirals increases with respect to the observed fraction by up to a factor of 20. These results show that

there is indeed an underestimation of disks galaxies at high redshift.

6.1.1 Morphological Fractions

Our findings on the morphological fractions of CANDELS field galaxies with the visual-classification method (Figure 5.2.3) suggest that galaxies do experience morphological transformations since $z = 3$. The main evolution found is that early-type disks decrease since $z = 2.75$ toward $z = 0.3$, while irregulars increase their fraction in the same redshift range. Also spheroids start to increase their fraction around $z \sim 1.125$. The star-forming subsample shows very similar trends, while in the quiescent subsample, early-type disks, late-type disks and irregulars maintain a constant fraction at all redshift, while spheroids increase their fraction significantly from $\sim 10\%$ at $z \sim 1.125$ to $\sim 40\%$ at $z \sim 0.3$. This result implies that star-forming early type disks decreasing fraction is due to morphological transformation into either star-forming irregulars or quiescent spheroids.

The results from the morphological coefficient-classification method (Figure 5.3.6) suggest a different morphological evolution history. Early-type disks are found to have a constant fraction in the redshift range considered, while late-type disk decrease their fraction by about $\sim 20\%$ from the highest to the lowest redshift bin. Irregulars and spheroids experience a $\sim 20\%$ increase toward $z \sim 0.3$, with irregulars having a more mildly evolution. Again, we find that the star-forming subsample display very similar evolutionary trends. On the other hand, the quiescent subsample shows a strong decrease in the fraction of late-type disk alongside a increase in spheroids toward the lowest redshift bin. This result suggest that quiescent late-type disk transform into non-star-forming spheroids. The quiescent subsample also shows a slight increasing trend for early-type disks, and thus late-type disks might also transition morphologically to this class.

Several studies have been conducted to explore the evolutionary patterns of morphological fractions in distant field galaxies. Conselice et al. (2005) performed visual classifications of H-band HST-images of galaxies in the Hubble Deep North and South Fields, up to $z \sim 3$. Their findings revealed a dominant fraction of peculiar galaxies, those galaxies characterized by perturbations or indication of merger activity (Abraham et al., 1996), at redshifts $z > 2$. However, this fraction showed a steep decline, accompanied by an increase in the fractions of elliptical and spiral galaxies. Whitney et al. (2021) observed a similar trend in CANDELS up to

$z \sim 3$, utilizing visual classifications from Kartaltepe et al. (2015). They observed a power-law increase in the fractions of spheroids and disks from approximately 25% at $z = 2.5$ to over 45% and $35 - 40\%$ at $z = 0.5$, respectively, while the fraction of peculiar galaxies exhibited a linear decrease from approximately 45% at $z = 3.0$ to approximately 15% at $z = 0.5$.

The evolutionary trends of the uncorrected visual-classified morphological fractions in CANDELS obtained in our study are in agreement with these results, excluding the steep rise of spheroids toward low redshift. This discrepancy may be attributed to the fact that previous studies considered ellipticals and lenticulars as spheroids, whereas we classify S0 galaxies as early-type disks and treat ellipticals as a distinct class. Furthermore, peculiar galaxies, although seemingly irregular at first order, are a different class from irregular galaxies. In contrast, the corrected fractions in CANDELS supports a scenario in which disks are more prevalent and irregulars are less present at higher redshifts. It should be noted that disparities between our results and previous investigations may arise from two factors: *i)* the broader and fundamentally different spheroids/disks/peculiar classification scheme employed in these studies, and/or *ii)* the omission of explicit considerations for the effects of CSBD on the morphological measurements. Given that the uncorrected morphological trends obtained in our study do partially align with the aforementioned previous investigations, we propose that the discrepancies primarily stem from our explicit consideration and correction of the CSBD effect.

The morphological mixing trends obtained through visual classification methods by Conselice et al. (2005) and Whitney et al. (2021) exhibit, however, significant discrepancies when compared to our morphological coefficient-based morphological fraction evolution. However, as previously mentioned, visual classifications are strongly influenced by the effects of CSBD and limitations in human visual perception due the loss of information, and thus a direct comparison must be done carefully.

The forthcoming generation of high-redshift surveys, such as the JWST, ELT and LSST, presents an opportunity to expand upon the present study and effectively assess the impact of CSBD at lower and higher redshifts. These surveys will benefit from enhanced resolution and depth (for example, LSST will be very deep after 10 years of observations), enabling more accurate and comprehensive quantitative as well as qualitative morphological classifications. Additionally, they will provide

an initial glimpse into the morphology of high-redshift galaxies. Therefore, these surveys hold great promise in advancing our understanding of the subject.

Recent investigations utilizing images from JWST have already shed light on the morphological fractions of field galaxies at $z > 3$. For example, Jacobs et al. (2023) employed visual classifications on a sample of field galaxies ranging from $z = 0.8$ to $z = 5.4$. They found that, for galaxies with stellar masses above $10^{9.5} M_{\odot}$, there is a steeply decreasing trend from $\sim 80\%$ at $z \sim 5$ to $\sim 20\%$ at $z < 2.55$ for peculiar galaxies, a mostly $\sim 20\%$ constant fraction of spheroids at all redshift ranges, and an increasing fraction of early-type (disk+spheroid) and late-type disks. These findings align with recent CNN-morphological measurements derived from JWST images by Huertas-Company et al. (2023), who revealed a substantial fraction of regular galaxies (comprising disks and bulges) at high redshifts within the higher mass ranges ($10.5 < \log(M_*/M_{\odot}) < 11.5$). In particular, they found the same decrease of irregular galaxy fraction from $z \sim 5$ to $z \sim 2$, a sort-of constant fraction at $\sim 20\%$ for spheroids and late-type disks, and an increase of the early-type disk fraction, from $\sim 20\%$ at $z \sim 5$ to $\sim 40\%$ at $z \sim 1$. Additionally, **?** has shown morphological coefficient-estimated morphological fractions with JWST images for the SMACS-0723 galaxy cluster, finding a decreasing spheroid trend, an increasing peculiar fraction and a constant disk fraction from $z \sim 5$ to $z \sim 2$. The fact that disk and spheroids are more common at $z > 2$, compared to what is seen with HST measurements, challenge the build-up timescale of the of Hubble-sequence.

Jacobs et al. (2023) have also found that galaxies at high redshift exhibit high levels of asymmetry in comparison to their local counterparts. The increased asymmetry observed in these high-redshift galaxies may be attributed to a greater frequency of ongoing interactions and mergers, which in turn contribute to morphological transformations. This aligns with the findings of Ferreira et al. (2022), who reported a rise in the proportion of post-merger galaxies within the redshift range of $0.5 < z < 2.5$, ranging from approximately 20% to 25% depending on the mass of the galaxies. However, in our investigation, we have discovered that the higher asymmetry observed in galaxies at higher redshifts could be attributed to CSBD. Therefore, it is imperative to conduct a thorough investigation into the effects of CSBD on asymmetry in order to validate the true nature of asymmetry in high-redshift galaxies.

The results from these studies align, to some extent, with our results. However some discrepancy is expected as these studies do not account for the effect of CSBD. Considering that the CSBD law follows a $(1+z)^{-4}$ relationship, it is expected that the CSBD effect will be even more influential on visual classification of galaxies at $z > 3$. Consequently, the fractions of spiral galaxies could be even higher, while the fractions of elliptical galaxies may be lower than what has been observed. Given that we have demonstrated the impact of CSBD at lower redshifts, it is crucial to incorporate these corrections when analyzing data from higher redshifts. The high-redshift visual morphological fractions measured in the studies previously mentioned show a decrease in peculiar galaxies, which should be overestimated according to our conclusions. In the same manner, the increasing fraction of disks should be underestimated. We, nevertheless, do not find an increase of late-type disks. We stress that this might be due to our morphological coefficient-classification criterion being too strict for classification of late-type disks galaxies at low redshift. Finally, we find an agreement with a sort-of constant low-fraction of spheroids, which among all the other morphological classes, is the one that is least affected by CSBD.

Given that the impact of the CSBD is more significant in visual classifications than in the classification based on morphological coefficients, we have chosen to rely on the results obtained from the second classification method for our analysis. Quantitative classification proves to be more robust and reliable compared to visual classification, particularly when dealing with "intermediate classes" such as the distinction between early-type disks, late-type disks, and spheroids. Therefore, we expect that the second classification method is able to capture subtle variations in light distribution and thus accurately characterize the morphology of galaxies.

6.1.1.1 Morphological Fractions as a function of Stellar Mass

A more thorough analysis can be provided by considering the morphological fractions as a function of stellar mass. The observational findings reported by Huertas-Company et al. (2023) indicate that spheroids at $z > 1$ have stellar masses exceeding $10^{10} M_{\odot}$. However, lower-mass spheroids become more prevalent at $z < 1$. Early-type disks progressively gain mass as we approach the present epoch, reaching a fraction of approximately 50% in the highest mass bin at $z = 0 - 1$. Late-type disks, on the other hand, exhibit an increase in their number

in the intermediate mass range, spanning from 10^9 to 10^{10} solar masses toward the current era. Finally, irregular galaxies have a higher fraction in the low-mass segment of the mass function, with a fraction close to 100% between $z = 3$ and $z = 6$. Nonetheless, this fraction declines to approximately 70% for redshifts below 1. Also, Martin et al. (2020) finds a similar trend, with spheroids dominating the high-mass end at high redshift ($z \sim 0.9$), and early-type disks (S0-Sa) becoming more massive at $z = 0$.

Interestingly, Varma et al. (2022) found similar trends for spheroids and early-type disks for the star-forming and quiescent subsamples. However, they found that irregulars and late-type disks have a higher fraction in both subsamples, with the fraction of late-type disks becoming higher at high masses and that of irregulars increasing in low stellar masses bins at $z = 0$.

We do find specific evolutionary trends in our morphological fractions as a function of stellar mass. In particular, spheroids and early-type disks tend to populate the higher stellar mass bins toward lower redshifts, while late-type disks and irregulars populate the low-mass bins at all redshifts. We stress here that our sample is limited in stellar mass, so this result is not simply a consequence of survey depth.

When looking at star-forming morphological fractions as a function of stellar mass, we find the same results than those of the whole sample. For the the quiescent subsample, we find different trends. Broadly speaking, all spheroids and early-type disks stellar mass bins get more populated with decreasing redshift. Late-type disks have a similar trend compared to the star-forming subsample.

While our results might be inconclusive regarding irregular, our main result is in agreement with previous studies: late-type disks typically have masses lower than $10^9 M_\odot$, and early-type disks and spheroids become more massive toward low redshift. This is in agreement with the well known bulge-growth of galaxies.

6.1.2 Morphological Fractions in Simulations

Simulations provide another useful source for comparison. Some studies, such as Huertas-Company et al. (2019) and Varma et al. (2022), show that the fractions of spheroids, early-type and late-type disks increases with stellar mass at lower redshift, while irregulars galaxies constitute the majority of the galaxy population at $z > 1.5$ with a fraction of up to $\sim 80\%$, decreasing to $\sim 20\%$ at $z = 0.5$.

From Varma et al. (2022), it can be seen that the star-forming TNG50 subsample has a very similar trend to that of the whole sample, while the quiescent subsample displays a much more complex behavior. At first order, we can distinguish that early-type disks and spheroids become more prominent in lower mass bins toward lower redshifts, and the same happens for late-type disks.

In the TNG50 sample, we also obtain complex results for the redshift evolution. Nevertheless, it is possible to discern that early-type disks tend to occupy the high-mass end of the mass function, while spheroids, late-type disks and irregulars do not show any evolutionary trend. In general terms, our results for CANDELS and Illustris are consistent within each other and with Huertas-Company et al. (2019); Varma et al. (2022) regarding early-type disks.

Making a direct and quantitative comparison between our results and those of previous studies becomes challenging. The lack of consistent morphological fraction information in the literature due to the different classification methods and schemes, and the limited consideration of CSBD in previous studies highlight the need for careful interpretation when comparing results.

We further emphasize that our arbitrary boundaries to distinguish morphological types, based on the method from Sazonova et al. (2020), are conservative, and we might be only capturing the subset of any morphological population with higher bulge fraction or higher concentration. Trying different definitions for morphological classes is beyond the scope of this work, whose principal aim is to determine the way in which CSBD affects the classification of the morphology of distant galaxies.

6.2 Morphological Transformations and Star-Formation Quenching

The results previously discussed imply that high-redshift quiescent late-type disks are transforming into quiescent spheroids and some others into early-type disks toward $z \sim 0.3$. Also, star-forming late-type disks are transitioning into irregular galaxies. For this scenario to be viable, we require evidence of high-redshift late-type disks to undergo a morphological transformation in a timescale shorter than $\sim 11 Gyr$ and, in some cases, to quench their star-formation.

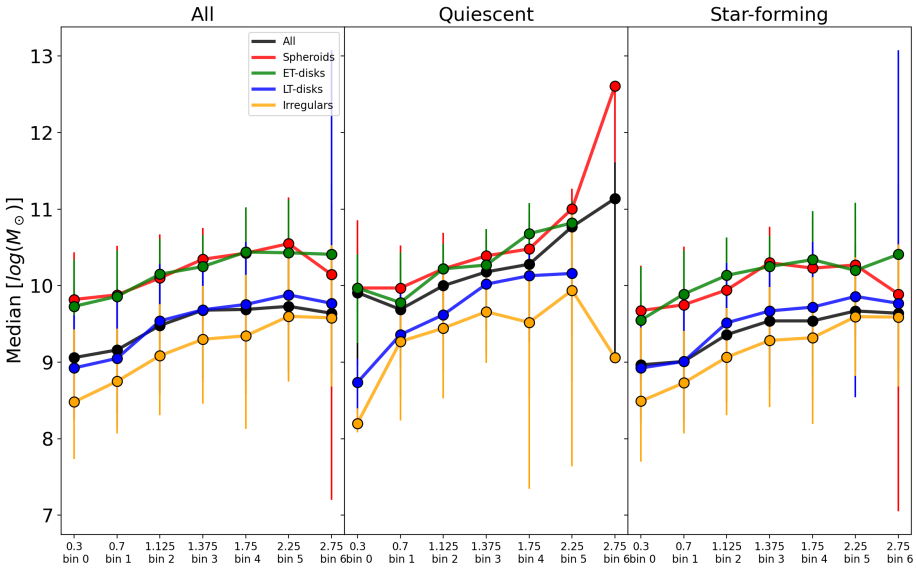

Figure 6.2.1: The median values of the bulge stellar mass for the whole, quiescent and star-forming samples (from left to right).

Minor and major merger events are good candidates to explain both morphological transformation paths for late-type disks. Dry major mergers can completely disrupt a late-type galaxy's disk, transforming the galaxy into an spheroid, or smooth out the disk structure, transforming the galaxy into an early-type disk. On the other hand, wet minor mergers may give rise to irregular substructures, and thus give the late-type disk a more asymmetric structure.

If we examine the medians of the bulge stellar mass distributions for the whole sample and the quiescent and star-forming subsamples, shown in Figure 6.2.1, we can note that in general all star-forming galaxies regardless of the morphological type have a lower bulge mass than non-star-forming galaxies. In particular, note that high-redshift quiescent late-type disks have more massive bulges than star-forming disks.

This suggest that high-redshift late-type disks undergo merger events, increasing their bulge mass and thus getting quenched while they also undergo a morphological transformation into spheroids or early-type disks, depending how strong is the merger. Alternatively, disk galaxies may undergo secular evolution, with mass being gradually accreted by the bulge from the disk.

Previous studies, for example Bluck et al. (2022), have examined the role of bulge growth in the process of star formation quenching. They find that the stellar mass of the bulge is the primary predictive parameter for quenching, surpassing the significance of other quantities such as the disk mass, the total stellar mass, and the bulge-to-total ratio (B/T). Consequently, it can be inferred that the quenching of star formation is driven by mechanisms that take place in the bulge such as AGN.

Extensive analyses in the literature have focused on the process of bulge-growth through mergers in galaxies (e.g. Hopkins et al. 2010; Brooks and Christensen 2016). It has been found that galaxy-satellite collisions increase the Sérsic index n and the bulge mass proportionally to the satellite mass Aguerri et al. (2001).

Notably the same is seen in simulations. Huertas-Company et al. (2019) conducted a study utilizing the IllustrisTNG simulation and demonstrated that the majority of massive galaxies exhibit a higher proportion of ex-situ stellar mass. Given the consistency of our findings with the results obtained from the IllustrisTNG-50 simulation, it can be inferred that the mechanisms governing galaxy formation, evolution, and morphological transformations as represented in the IllustrisTNG model are capable of accurately predicting such transformations.

Another bulge-growth explanatory mechanism that has been proposed is the radio-mode active galactic nucleus (AGN) feedback. In this process, the accretion of material onto a supermassive black hole (SMBH) generates powerful outflows of energy. These outflows expel or heat the surrounding gas, effectively suppressing star formation (Carilli and Walter, 2013b).

Recent determinations of the growth rate of massive black holes in comparison to the cosmic star formation rate density suggest that the peak of black hole accretion is consistent with the peak of star formation, indicating a close relationship between stellar formation quenching and black hole growth (Madau and Dickinson, 2014). According to more recent research, Varma et al. (2022) conducted a study using the IllustrisTNG-50 simulation and discovered a correlation between supermassive black hole (SMBH) activity and the morphological transformation of massive galaxies. They found that when the SMBH enters a low-accretion state, known as the kinetic-feedback mode, gas is rapidly depleted, increasing the observed central mass density of the galaxy and eventually resulting in quenching. Another

study by Koutsouridou and Cattaneo (2022) supports this idea, stating that morphological transformation plays a crucial role in the quenching process. They explain that during galaxy mergers, the transformation of disks into bulges occurs, which simultaneously feeds the SMBH. Star-forming galaxies, with a SMBH in quasar-mode, experience an increase in SMBH mass through mergers until a radio mode nuclear activity is reached. This nuclear activity is capable heating the surrounding gas, preventing gas cooling and thus resulting in the quenching of star formation. Consequently, galaxies undergo an inside-out quenching process (e.g Genel et al., 2014; Tacchella et al., 2015; Bluck et al., 2020). An important aspect to consider is the presence of star-forming spheroids and quiescent disks within both the CANDELS and TNG50 samples. This observation aligns with the findings of Brennan et al. (2015), who investigated the assembly of galaxies using the specific star formation rate versus Sérsic index (n) plane. They classified galaxies into four populations: star-forming/quiescent disks and star-forming/quiescent spheroids. Their analysis demonstrated that a model incorporating bulge growth through both disk instabilities and mergers provides a better fit to the observed distribution of these four populations within the CANDELS dataset.

Furthermore, de Sá-Freitas et al. (2022) discovered evidence supporting different formation processes for quenched disk-like galaxies and quenched spheroids. Quenched disk-like galaxies are more likely undergoing secular processes, such as internal dynamical instabilities, while quenched spheroids have likely experienced more violent interactions, including major or minor mergers, which may have influenced their star formation histories. Additionally, the presence of blue cloud ellipticals (Schawinski et al., 2014), which are predominantly found in low-density environments (Bamford et al., 2009; Dhiwar et al., 2023), suggests the occurrence of post-merger objects or post-rejuvenation processes that have led to their current properties.

In line with these findings, Lu et al. (2021) discovered a decreasing fraction of AGN observed in quiescent late-type galaxies over time, indicating the role of AGN feedback in maintaining quiescence in these systems. Conversely, the high fraction of AGN observed in star-forming elliptical galaxies implies the involvement of positive AGN feedback. In this scenario, AGN-driven outflows compress the gas, leading to its collapse and subsequent formation of new stars, thereby triggering star formation (Cresci and Maiolino, 2018; Nesvadba et al., 2020). It is also

important in this context to assess the role of the local environment, since the field comprises a variety of large-scale structures encompassing groups, filaments and voids. The environment affects the quenching of star formation since galaxies may interact with their neighbors.

Several studies have investigated the factors influencing quenching timescales, stellar mass, and the role of the environment in star formation quenching and morphological transformations. Wetzel et al. (2013) and Hahn et al. (2017) focused on satellite and central galaxies in clusters, respectively, and found that more massive galaxies exhibit shorter quenching timescales. Walters et al. (2022) demonstrated that quenched galaxies tend to have higher stellar and halo masses, as well as larger effective radii. Furthermore, Gu et al. (2021) highlighted the importance of stellar mass as a dominant variable in quenching massive galaxies at high redshifts ($z > 1$), whereas environmental quenching is more effective for low-mass galaxies at lower redshifts ($z < 1$).

Lu et al. (2021) reported distinct mass distributions and local environment density distributions between quiescent and star-forming galaxies at $z < 1.5$ for a given morphological type. They also found that, for a given star formation status, bulge and disk galaxies have different mass distributions but similar local density distributions. These findings suggest that stellar mass plays a crucial role in quenching and morphological transformations at high redshifts, while local galaxy density primarily affects quenching but has a lesser impact on morphological transformations. This indicates that galaxy morphology is more closely related with star formation rather than the environment at high redshifts. Nonetheless, as time progresses, the influence of a galaxy's mass on its morphology becomes less prominent as environmental quenching gains more significance Gu et al. (2021).

Chapter 7

Conclusions

7.1 Summary of the Results

The structure of galaxies is one of their fundamental properties, since it is related with their star formation and internal dynamics. The evolution of galaxies is the result of complex physical mechanisms that affect and modify their physical properties with time. The physical drivers of the evolution of galaxies may have both internal and environmental origins, and one of the key problems in modern astrophysics is the assessment of the relative importance of the internal and environmental processes that change the physical properties of galaxies.

The structural properties of galaxies may change as a result of internal processes, such as the quenching of star formation induced by AGN outflows or the growth of bulges triggered by instabilities in the disk, and as a consequence of the interactions of galaxies with their surrounding environment, as in the case of galaxy mergers and tidal interactions. Internal and environmental mechanisms are not independent: for instance, Ellison et al. (2015) showed that AGN are more frequent among galaxies in pair, suggesting that the activation of a SMBH is favoured during this interaction.

Thus, the study of the structure of galaxies is key to in the investigation of galaxy evolution, since by looking at the change of the morphological mixing of galaxies with redshift one may try to infer what the main physical mechanisms responsible for the structural evolution of galaxies are.

The present thesis presents estimations of the morphological fractions of field galaxies at $0.2 < z < 3.0$ from the CANDELS survey. We conducted a detailed analysis of the effects of CSBD on the morphological classification and on the measurements of morphological coefficients. For this purpose, we selected a sample of 157 galaxies from the GOODS-S field at redshift $0.2 \leq z < 0.4$ and simulated them at higher redshifts, accounting for changes due to CSBD, resolution and signal-to-noise ratio. We used two characterizations of galaxy morphology, namely the visual classification and the $G - M_{20}$ plane.

For the visual classification, a group of four classifiers assigned a morphological type to each galaxy in both its original (bin 0, $z \sim 0.3$) and simulated versions (bins 1 trough 6, or $z \sim 0.7$ to $z \sim 2.75$). By comparing the reference morphology (bin 0, $z \sim 0.3$) with the morphology assigned at higher redshift, we estimated correction terms for false positives and false negatives.

For the $G-M_{20}$-based morphology we compared the two morphological coefficients G and M_{20} for the original and simulated galaxies. We then developed a probabilistic method through which a correction term was applied to high-redshift galaxies to recover the unbiased values of the Gini coefficient and M_{20}. We further assigned a morphological class to each galaxy based on the values of their coefficients, following the criterion proposed by Sazonova et al. (2020).

We studied the morphological fractions in CANDELS and compared our results with those obtained on mock images built from the IllustrisTNG-50 simulation. We investigated the morphological fractions as a function of stellar mass. Finally, we studied the change in redshift of the morphological fractions for the entire galaxy population and for the subsamples of star-forming and quiescent galaxies Our main findings are the following:

- CSBD is a significant source of bias regarding the visual morphological classification of galaxies. The confusion between morphological types manifests itself in the fact that at high redshifts the numbers of spheroidal and irregular galaxies are overestimated by 20% and 60%, respectively, while the numbers of early- and late-type disks are underestimated by up to 40%. Thus, human classifiers and, probably, machine learning and deep learning models trained on visually labeled samples tend to classify distant galaxies more easily as spheroids or irregulars than as disk-dominated. The

magnitude of this effect becomes significant at $z \sim 1.375$ and increases at higher redshifts.

- There are two primary confusion channels that result from CSBD on the visual morphological classification of galaxies. The first channel comprises the spheroid vs disk confusion, which consists in the fact that the lowest surface brightness features in galaxies, such as the disks, may fall below the sky level, giving to an actual disk galaxy the appearance of a spheroid. The second channel consists in the irregular vs regular confusion, which stems from the increase in M_{20} and shape asymmetry and the decrease in G which cause that a galaxy, regardless of its actual morphology, would appear irregular to a human classifier or would be classified as such by an algorithm trained on a visual classification.

- The CSBD affects does not have a significant impact on the estimation of the morphological coefficients G and M_{20}. We found that dimming of galaxies, the dropout of pixel with fluxes under the source detection threshold and the change of pixel scale does not affect significantly the cumulative distribution of the pixels flux and the flux distribution width. Therefore, morphological coefficients are able to trace the light distribution of a galaxy much better than the human eye for low-surface brightness objects.

- Higher redshift galaxies tend to exhibit lower values of the Gini coefficient and half-light radius, and higher values of M_{20} and shape asymmetry, indicating that distant galaxies appear smaller, fainter, clumpier and more asymmetric than their low-redshift counterparts. However, these trends are not statistically significant.

- Morphological fractions based on the morphological coefficients-classification method show that early-type galaxies have a $\sim 40\%$ constant fraction from $z \sim 2.75$ to $z \sim 0.3$ and that late-type disks decrease their fraction about $\sim 20\%$ monotonically in the same redshift range. Also, irregular and spheroid galaxies increase their fraction up to $\sim 20\%$ toward $z \sim 0.3$.

- When dividing the CANDELS sample into star-forming and quiescent galaxies, we see that the trends with redshift of the morphological sample in the former case resemble those of the entire CANDELS sample. On the other hand, quiescent galaxies are predominantly late-type disks at $z > 2.75$.

However, this fractions decreases at the exchange of a strongly increasing fraction of spheroids and an slight increase in the fraction of early-type disks.

- When examining the morphological fractions as a function of the stellar mass of the galaxies, we found that spheroids and spheroids tend to populate the higher stellar mass bins ($M_* > 10^{10} M_\odot$) toward lower redshifts, while late-type disks and irregular galaxies populate the lower-mass bins. The same trends are found for the star-forming galaxies and the quiescent sample, although the trends are much more weak in the latter.

- Our results suggest that high-redshift quiescent late-type disks are transforming into non-star-forming spheroids and/or early-type disks, while star-forming late-type disks transform into irregulars. We consider that Dry major mergers and wet minor mergers are the best candidates to explain the morphological evolution of late-type disks. As the quiescent subsample has more massive bulges that the star-forming subsample, we propose that galaxies increase their bulge mass through merger events and undergo quenching thereafter via AGN-feedback or black-hole feedback.

- Notably, the findings in the CANDELS sample align to some extent with those observed in the IllustrisTNG-50 sample, suggesting that the prediction of IllustrisTNG on the structural evolution of galaxies are reliable.

We do find discrepancies between our results and the morphological fractions as a function of redshift and stellar mass measured by previous studies. We argue that these discrepancies are mainly due to the fact that most of the morphological fractions in literature do not account for the effect of CSBD, which we have prove to be a very significant source of bias for visual morphological classifications at $z > 1$. Also, our classification criterion using morphological coefficients, based on the method of Sazonova et al. (2020), has arbitrary boundaries that needs to be tuned to have a better match with visual or quantitative morphology. We are currently working on refining the classification boundaries in the G-M_{20} plane so we avoid over- and under-estimation of morphological classes.

7.2 Ongoing Work and Future Perspectives

The next steps in our research are the refinement of the boundaries of early-type and late-type disks in the G-M_{20} plane and the construction of an empirical model for the physical interpretation of the results and trends reported in this work for the morphological fractions.

In order to achieve statistical significance in our findings, our aim is to conduct these experiments using a larger parent sample. However, the inclusion of a larger sample leads to the utilization of automation techniques. In the present study, the parent sample comprised 206 galaxies, and required the visual classification of a total of 1,442 galaxies. Thus, we emphasize the importance of developing a methodology capable of effectively addressing the bias introduced by CSBD when dealing with extensive datasets.

As discussed in this thesis, the morphology of galaxies is related to their star formation rate and stellar mass. It is also known that the density of the local environment affects the structural properties of galaxies since mechanisms such as mergers and tidal interactions may disrupt or transform the morphology.

We are currently elaborating a toy model in which the morphology is a variable that depends on the stellar mass, star formation rate and local number density of galaxies. All this variables are being treated as randomly distributed according to probability densities that are calibrated on the observations. The discussion of such a model is beyond the scope of this thesis and will be the subject of a forthcoming work.

We finally note that the present work has been developed within a collaboration that is aimed at studying the structural evolution in different cosmic large-scale structures. A work on the morphological evolution of galaxies in a sample of clusters at $z = 0.2 - 0.9$ from the Cluster Lensing and Supernova Survey with Hubble (CLASH, Postman et al., 2012) is currently being led by Pierluigi Cerulo who is supervising this thesis. By comparing the results obtained in clusters with those presented here, we will be able to draw a picture of the structural changes of galaxies in different environments.

Bibliography

Abel, T., Anninos, P., Norman, M. L., and Zhang, Y. (1998). First Structure Formation. I. Primordial Star-forming Regions in Hierarchical Models. , 508(2):518–529.

Abraham, R. G., Tanvir, N. R., Santiago, B. X., Ellis, R. S., Glazebrook, K., and van den Bergh, S. (1996). Galaxy morphology to I=25 mag in the Hubble Deep Field. , 279(3):L47–L52.

Abraham, R. G. and van den Bergh, S. (2001). The Morphological Evolution of Galaxies. *Science*, 293(5533):1273–1278.

Abraham, R. G., van den Bergh, S., and Nair, P. (2003). A New Approach to Galaxy Morphology. I. Analysis of the Sloan Digital Sky Survey Early Data Release. , 588(1):218–229.

Aguerri, J. A. L., Balcells, M., and Peletier, R. F. (2001). Growth of galactic bulges by mergers. I. Dense satellites. , 367:428–442.

Baes, M., Verstappen, J., De Looze, I., Fritz, J., Saftly, W., Vidal Pérez, E., Stalevski, M., and Valcke, S. (2011). Efficient Three-dimensional NLTE Dust Radiative Transfer with SKIRT. , 196(2):22.

Baldry, I. K., Glazebrook, K., Brinkmann, J., Ivezić, Ž., Lupton, R. H., Nichol, R. C., and Szalay, A. S. (2004). Quantifying the Bimodal Color-Magnitude Distribution of Galaxies. , 600(2):681–694.

Bamford, S. P., Nichol, R. C., Baldry, I. K., Land, K., Lintott, C. J., Schawinski, K., Slosar, A., Szalay, A. S., Thomas, D., Torki, M., Andreescu, D., Edmondson, E. M., Miller, C. J., Murray, P., Raddick, M. J., and Vandenberg, J. (2009). Galaxy Zoo: the dependence of morphology and colour on environment*. , 393(4):1324–1352.

Barden, M., Jahnke, K., and Häußler, B. (2008). FERENGI: Redshifting Galaxies from SDSS to GEMS, STAGES, and COSMOS. , 175(1):105–115.

Bershady, M. A., Jangren, A., and Conselice, C. J. (2000). Structural and Photometric Classification of Galaxies. I. Calibration Based on a Nearby Galaxy Sample. , 119(6):2645–2663.

Bertin, E. and Arnouts, S. (1996). SExtractor: Software for source extraction. , 117:393–404.

Binney, J. and Merrifield, M. (1998). *Galactic Astronomy*.

Bluck, A. F. L., Maiolino, R., Brownson, S., Conselice, C. J., Ellison, S. L., Piotrowska, J. M., and Thorp, M. D. (2022). The quenching of galaxies, bulges, and disks since cosmic noon. A machine learning approach for identifying causality in astronomical data. , 659:A160.

Bluck, A. F. L., Maiolino, R., Piotrowska, J. M., Trussler, J., Ellison, S. L., Sánchez, S. F., Thorp, M. D., Teimoorinia, H., Moreno, J., and Conselice, C. J. (2020). How do central and satellite galaxies quench? - Insights from spatially resolved spectroscopy in the MaNGA survey. , 499(1):230–268.

Bouwens, R. J., Illingworth, G. D., Blakeslee, J. P., Broadhurst, T. J., and Franx, M. (2004). Galaxy Size Evolution at High Redshift and Surface Brightness Selection Effects: Constraints from the Hubble Ultra Deep Field. , 611(1):L1–L4.

Brammer, G. B., van Dokkum, P. G., Franx, M., Fumagalli, M., Patel, S., Rix, H.-W., Skelton, R. E., Kriek, M., Nelson, E., Schmidt, K. B., Bezanson, R., da Cunha, E., Erb, D. K., Fan, X., Förster Schreiber, N., Illingworth, G. D., Labbé, I., Leja, J., Lundgren, B., Magee, D., Marchesini, D., McCarthy, P., Momcheva, I., Muzzin, A., Quadri, R., Steidel, C. C., Tal, T., Wake, D., Whitaker, K. E., and Williams, A. (2012). 3D-HST: A Wide-field Grism Spectroscopic Survey with the Hubble Space Telescope. , 200(2):13.

Brennan, R., Pandya, V., Somerville, R. S., Barro, G., Taylor, E. N., Wuyts, S., Bell, E. F., Dekel, A., Ferguson, H. C., McIntosh, D. H., Papovich, C., and Primack, J. (2015). Quenching and morphological transformation in semi-analytic models and CANDELS. , 451(3):2933–2956.

Brooks, A. and Christensen, C. (2016). Bulge Formation via Mergers in Cosmological Simulations. In Laurikainen, E., Peletier, R., and Gadotti, D., editors, *Galactic Bulges*, volume 418 of *Astrophysics and Space Science Library*, page 317.

Bruce, V. A., Dunlop, J. S., Cirasuolo, M., McLure, R. J., Targett, T. A., Bell, E. F., Croton, D. J., Dekel, A., Faber, S. M., Ferguson, H. C., Grogin, N. A., Kocevski, D. D., Koekemoer, A. M., Koo, D. C., Lai, K., Lotz, J. M., McGrath, E. J., Newman, J. A., and van der Wel, A. (2012). The morphologies of massive galaxies at $1 < z < 3$ in the CANDELS-UDS field: compact bulges, and the rise and fall of massive discs. , 427(2):1666–1701.

Buta, R. J. (2011). Galaxy Morphology. *arXiv e-prints*, page arXiv:1102.0550.

Butcher, H. and Oemler, A., J. (1978). The evolution of galaxies in clusters. I. ISIT photometry of Cl 0024+1654 and 3C 295. , 219:18–30.

Calvi, R., Poggianti, B. M., Fasano, G., and Vulcani, B. (2012). The distribution of galaxy morphological types and the morphology-mass relation in different environments at low redshift. , 419(1):L14–L18.

Calvi, V., Stiavelli, M., Bradley, L., Pizzella, A., and Kim, S. (2014). The Effect of Surface Brightness Dimming in the Selection of High-z Galaxies. , 796(2):102.

Cameron, E. (2011). On the Estimation of Confidence Intervals for Binomial Population Proportions in Astronomy: The Simplicity and Superiority of the Bayesian Approach. , 28(2):128–139.

Cappellari, M. (2016). Structure and Kinematics of Early-Type Galaxies from Integral Field Spectroscopy. , 54:597–665.

Cappellari, M., Emsellem, E., Krajnović, D., McDermid, R. M., Scott, N., Verdoes Kleijn, G. A., Young, L. M., Alatalo, K., Bacon, R., Blitz, L., Bois, M., Bournaud, F., Bureau, M., Davies, R. L., Davis, T. A., de Zeeuw, P. T., Duc, P.-A., Khochfar, S., Kuntschner, H., Lablanche, P.-Y., Morganti, R., Naab, T., Oosterloo, T., Sarzi, M., Serra, P., and Weijmans, A.-M. (2011). The ATLAS^{3D} project - I. A volume-limited sample of 260 nearby early-type galaxies: science goals and selection criteria. , 413(2):813–836.

Carilli, C. L. and Walter, F. (2013a). Cool Gas in High-Redshift Galaxies. , 51(1):105–161.

Carilli, C. L. and Walter, F. (2013b). Cool Gas in High-Redshift Galaxies. , 51(1):105–161.

Cerulo, P., Couch, W. J., Lidman, C., Demarco, R., Huertas-Company, M., Mei, S., Sánchez-Janssen, R., Barrientos, L. F., and Muñoz, R. (2017). The morphological transformation of red sequence galaxies in clusters since z $\sim$ 1. , 472(1):254–272.

Cerulo, P., Orellana, G. A., and Covone, G. (2019). The evolution of brightest cluster galaxies in the nearby Universe - I. Colours and stellar masses from the Sloan Digital Sky Survey and Wide Infrared Survey Explorer. , 487(3):3759–3775.

Chapman, S. C., Windhorst, R., Odewahn, S., Yan, H., and Conselice, C. (2003). Hubble Space Telescope Images of Submillimeter Sources: Large Irregular Galaxies at High Redshift. , 599(1):92–104.

Christlein, D. and Zabludoff, A. I. (2005). Disentangling Morphology, Star Formation, Stellar Mass, and Environment in Galaxy Evolution. , 621(1):201–214.

Cole, S., Lacey, C. G., Baugh, C. M., and Frenk, C. S. (2000). Hierarchical galaxy formation. , 319(1):168–204.

Conselice, C. J. (2014). The Evolution of Galaxy Structure Over Cosmic Time. , 52:291–337.

Conselice, C. J., Blackburne, J. A., and Papovich, C. (2005). The Luminosity, Stellar Mass, and Number Density Evolution of Field Galaxies of Known Morphology from z = 0.5 to 3. , 620(2):564–583.

Conselice, C. J., Grogin, N. A., Jogee, S., Lucas, R. A., Dahlen, T., de Mello, D., Gardner, J. P., Mobasher, B., and Ravindranath, S. (2004). Observing the Formation of the Hubble Sequence in the Great Observatories Origins Deep Survey. , 600(2):L139–L142.

Cresci, G. and Maiolino, R. (2018). Observing positive and negative AGN feedback. *Nature Astronomy*, 2:179–180.

de Jong, J. T. A., Verdoes Kleijn, G. A., Kuijken, K. H., and Valentijn, E. A. (2013). The Kilo-Degree Survey. *Experimental Astronomy*, 35(1-2):25–44.

de Sá-Freitas, C., Gonçalves, T. S., de Carvalho, R. R., Menéndez-Delmestre, K., Barchi, P. H., Sampaio, V. M., Basu-Zych, A., Darvish, B., and Martin, C. (2022). Quenching, bursting, and galaxy shapes: colour transformation as a function of morphology. , 509(3):3889–3903.

de Souza, R. E., Gadotti, D. A., and dos Anjos, S. (2004). BUDDA: A New Two-dimensional Bulge/Disk Decomposition Code for Detailed Structural Analysis of Galaxies. , 153(2):411–427.

de Vaucouleurs, G. (1948). Recherches sur les Nebuleuses Extragalactiques. *Annales d'Astrophysique*, 11:247.

de Vaucouleurs, G. (1959). Classification and Morphology of External Galaxies. *Handbuch der Physik*, 53:275.

Deger, S., Rudnick, G., Kelkar, K., Aragón-Salamanca, A., Desai, V., Lotz, J. M., Jablonka, P., Moustakas, J., and Zaritsky, D. (2018). Tidal Interactions and Mergers in Intermediate-redshift EDisCS Clusters. , 869(1):6.

Delgado-Serrano, R., Hammer, F., Yang, Y. B., Puech, M., Flores, H., and Rodrigues, M. (2010). How was the Hubble sequence 6 Gyr ago? , 509:A78.

Dhiwar, S., Saha, K., Dekel, A., Paswan, A., Pandey, D., Cortesi, A., and Pandge, M. (2023). Witnessing the star formation quenching in L_* ellipticals. , 518(4):4943–4960.

Djorgovski, S. and Davis, M. (1987). Fundamental Properties of Elliptical Galaxies. , 313:59.

Dressler, A. (1980). Galaxy morphology in rich clusters: implications for the formation and evolution of galaxies. , 236:351–365.

Duncan, K., Conselice, C. J., Mortlock, A., Hartley, W. G., Guo, Y., Ferguson, H. C., Davé, R., Lu, Y., Ownsworth, J., Ashby, M. L. N., Dekel, A., Dickinson, M., Faber, S., Giavalisco, M., Grogin, N., Kocevski, D., Koekemoer, A., Somerville, R. S., and White, C. E. (2014). The mass evolution of the first

galaxies: stellar mass functions and star formation rates at $4 < z < 7$ in the CANDELS GOODS-South field. , 444(3):2960–2984.

Eliche-Moral, M. C., Rodríguez-Pérez, C., Borlaff, A., Querejeta, M., and Tapia, T. (2018). Formation of S0 galaxies through mergers. Morphological properties: tidal relics, lenses, ovals, and other inner components. , 617:A113.

Ellison, S. L., Patton, D. R., and Hickox, R. C. (2015). Galaxy pairs in the Sloan Digital Sky Survey - XII. The fuelling mechanism of low-excitation radio-loud AGN. , 451:L35–L39.

Fasano, G., Poggianti, B. M., Couch, W. J., Bettoni, D., Kjærgaard, P., and Moles, M. (2000). The Evolution of the Galactic Morphological Types in Clusters. , 542(2):673–683.

Ferreira, L., Adams, N., Conselice, C. J., Sazonova, E., Austin, D., Caruana, J., Ferrari, F., Verma, A., Trussler, J., Broadhurst, T., Diego, J., Frye, B. L., Pascale, M., Wilkins, S. M., Windhorst, R. A., and Zitrin, A. (2022). Panic! at the Disks: First Rest-frame Optical Observations of Galaxy Structure at $z > 3$ with JWST in the SMACS 0723 Field. , 938(1):L2.

Florian, M. K., Li, N., and Gladders, M. D. (2016). The Gini Coefficient as a Morphological Measurement of Strongly Lensed Galaxies in the Image Plane. , 832(2):168.

Franx, M., van Dokkum, P. G., Förster Schreiber, N. M., Wuyts, S., Labbé, I., and Toft, S. (2008). Structure and Star Formation in Galaxies out to $z = 3$: Evidence for Surface Density Dependent Evolution and Upsizing. , 688(2):770–788.

Freeman, K. C. (1970). On the Disks of Spiral and S0 Galaxies. , 160:811.

Genel, S., Vogelsberger, M., Springel, V., Sijacki, D., Nelson, D., Snyder, G., Rodriguez-Gomez, V., Torrey, P., and Hernquist, L. (2014). Introducing the Illustris project: the evolution of galaxy populations across cosmic time. , 445(1):175–200.

Genzel, R., Burkert, A., Bouché, N., Cresci, G., Förster Schreiber, N. M., Shapley, A., Shapiro, K., Tacconi, L. J., Buschkamp, P., Cimatti, A., Daddi, E., Davies, R., Eisenhauer, F., Erb, D. K., Genel, S., Gerhard, O., Hicks, E., Lutz, D., Naab, T., Ott, T., Rabien, S., Renzini, A., Steidel, C. C., Sternberg, A., and Lilly, S. J. (2008). From Rings to Bulges: Evidence for Rapid Secular Galaxy Evolution at z ~2 from Integral Field Spectroscopy in the SINS Survey. , 687(1):59–77.

Gobat, R., Magdis, G., D'Eugenio, C., and Valentino, F. (2020). The evolution of the gas fraction of quiescent galaxies modeled as a consequence of their creation rate. , 644:L7.

Graham, A. W., Driver, S. P., Petrosian, V., Conselice, C. J., Bershady, M. A., Crawford, S. M., and Goto, T. (2005). Total Galaxy Magnitudes and Effective Radii from Petrosian Magnitudes and Radii. , 130(4):1535–1544.

Graham, A. W. and Guzmán, R. (2003). HST Photometry of Dwarf Elliptical Galaxies in Coma, and an Explanation for the Alleged Structural Dichotomy between Dwarf and Bright Elliptical Galaxies. , 125(6):2936–2950.

Grogin, N. A., Kocevski, D. D., Faber, S. M., Ferguson, H. C., Koekemoer, A. M., Riess, A. G., Acquaviva, V., Alexander, D. M., Almaini, O., Ashby, M. L. N., Barden, M., Bell, E. F., Bournaud, F., Brown, T. M., Caputi, K. I., Casertano, S., Cassata, P., Castellano, M., Challis, P., Chary, R.-R., Cheung, E., Cirasuolo, M., Conselice, C. J., Roshan Cooray, A., Croton, D. J., Daddi, E., Dahlen, T., Davé, R., de Mello, D. F., Dekel, A., Dickinson, M., Dolch, T., Donley, J. L., Dunlop, J. S., Dutton, A. A., Elbaz, D., Fazio, G. G., Filippenko, A. V., Finkelstein, S. L., Fontana, A., Gardner, J. P., Garnavich, P. M., Gawiser, E., Giavalisco, M., Grazian, A., Guo, Y., Hathi, N. P., Häussler, B., Hopkins, P. F., Huang, J.-S., Huang, K.-H., Jha, S. W., Kartaltepe, J. S., Kirshner, R. P., Koo, D. C., Lai, K., Lee, K.-S., Li, W., Lotz, J. M., Lucas, R. A., Madau, P., McCarthy, P. J., McGrath, E. J., McIntosh, D. H., McLure, R. J., Mobasher, B., Moustakas, L. A., Mozena, M., Nandra, K., Newman, J. A., Niemi, S.-M., Noeske, K. G., Papovich, C. J., Pentericci, L., Pope, A., Primack, J. R., Rajan, A., Ravindranath, S., Reddy, N. A., Renzini, A., Rix, H.-W., Robaina, A. R., Rodney, S. A., Rosario, D. J., Rosati, P., Salimbeni, S., Scarlata, C., Siana, B., Simard, L., Smidt, J., Somerville, R. S., Spinrad, H., Straughn, A. N., Strolger, L.-G., Telford, O., Teplitz, H. I., Trump, J. R., van der Wel, A., Villforth, C., Wechsler, R. H., Weiner, B. J., Wiklind, T., Wild, V., Wilson, G., Wuyts, S., Yan, H.-J., and Yun, M. S. (2011). CANDELS: The Cosmic Assembly Near-infrared Deep Extragalactic Legacy Survey. , 197(2):35.

Gu, Y., Fang, G., Yuan, Q., Lu, S., and Liu, S. (2021). The Effect of Environment on Star Formation Activity and Morphology at $0.5 < z < 2.5$ in CANDELS. , 921(1):60.

Guaita, L., Melinder, J., Hayes, M., Östlin, G., Gonzalez, J. E., Micheva, G., Adamo, A., Mas-Hesse, J. M., Sandberg, A., Otí-Floranes, H., Schaerer, D., Verhamme, A., Freeland, E., Orlitová, I., Laursen, P., Cannon, J. M., Duval, F., Rivera-Thorsen, T., Herenz, E. C., Kunth, D., Atek, H., Puschnig, J., Gruyters, P., and Pardy, S. A. (2015). The Lyman alpha reference sample. IV. Morphology at low and high redshift. , 576:A51.

Gudehus, D. H. (1973). Radius - parameter and surface brightness as a function of galaxy total magnitude for clusters of galaxies. , 78:583–593.

Gunn, J. E. and Gott, J. Richard, I. (1972). On the Infall of Matter Into Clusters of Galaxies and Some Effects on Their Evolution. , 176:1.

Guo, Y., Ferguson, H. C., Giavalisco, M., Barro, G., Willner, S. P., Ashby, M. L. N., Dahlen, T., Donley, J. L., Faber, S. M., Fontana, A., Galametz, A., Grazian, A., Huang, K.-H., Kocevski, D. D., Koekemoer, A. M., Koo, D. C., McGrath, E. J., Peth, M., Salvato, M., Wuyts, S., Castellano, M., Cooray, A. R., Dickinson, M. E., Dunlop, J. S., Fazio, G. G., Gardner, J. P., Gawiser,

E., Grogin, N. A., Hathi, N. P., Hsu, L.-T., Lee, K.-S., Lucas, R. A., Mobasher, B., Nandra, K., Newman, J. A., and van der Wel, A. (2013). CANDELS Multi-wavelength Catalogs: Source Detection and Photometry in the GOODS-South Field. , 207(2):24.

Hahn, C., Tinker, J. L., and Wetzel, A. (2017). Star Formation Quenching Timescale of Central Galaxies in a Hierarchical Universe. , 841(1):6.

Hausman, M. A. and Ostriker, J. P. (1978). Galactic cannibalism. III. The morphological evolution of galaxies and clusters. , 224:320–336.

Holden, B. P., Illingworth, G. D., Franx, M., Blakeslee, J. P., Postman, M., Kelson, D. D., van der Wel, A., Demarco, R., Magee, D. K., Tran, K. V., Zirm, A., Ford, H., Rosati, P., and Homeier, N. (2007). Mass Selection and the Evolution of the Morphology-Density Relation from z = 0.8 to 0. , 670(1):190–205.

Hopkins, P. F., Bundy, K., Croton, D., Hernquist, L., Keres, D., Khochfar, S., Stewart, K., Wetzel, A., and Younger, J. D. (2010). Mergers and Bulge Formation in ΛCDM: Which Mergers Matter? , 715(1):202–229.

Hopkins, P. F., Somerville, R. S., Cox, T. J., Hernquist, L., Jogee, S., Kereš, D., Ma, C.-P., Robertson, B., and Stewart, K. (2009). The effects of gas on morphological transformation in mergers: implications for bulge and disc demographics. , 397(2):802–814.

Hubble, E. P. (1926). Extragalactic nebulae. , 64:321–369.

Hubble, E. P. (1936). *Realm of the Nebulae*.

Huertas-Company, M., Bernardi, M., Pérez-González, P. G., Ashby, M. L. N., Barro, G., Conselice, C., Daddi, E., Dekel, A., Dimauro, P., Faber, S. M., Grogin, N. A., Kartaltepe, J. S., Kocevski, D. D., Koekemoer, A. M., Koo, D. C., Mei, S., and Shankar, F. (2016). Mass assembly and morphological transformations since z $\sim$ 3 from CANDELS. , 462(4):4495–4516.

Huertas-Company, M., Gravet, R., Cabrera-Vives, G., Pérez-González, P. G., Kartaltepe, J. S., Barro, G., Bernardi, M., Mei, S., Shankar, F., Dimauro, P., Bell, E. F., Kocevski, D., Koo, D. C., Faber, S. M., and Mcintosh, D. H. (2015). A Catalog of Visual-like Morphologies in the 5 CANDELS Fields Using Deep Learning. , 221(1):8.

Huertas-Company, M., Iyer, K. G., Angeloudi, E., Bagley, M. B., Finkelstein, S. L., Kartaltepe, J., Sarmiento, R., Vega-Ferrero, J., Arrabal Haro, P., Behroozi, P., Buitrago, F., Cheng, Y., Costantin, L., Dekel, A., Dickinson, M., Elbaz, D., Grogin, N. A., Hathi, N. P., Holwerda, B. W., Koekemoer, A. M., Lucas, R. A., Papovich, C., Pérez-González, P. G., Pirzkal, N., Seillé, L.-M., de la Vega, A., Wuyts, S., Yang, G., and Yung, L. Y. A. (2023). Galaxy Morphology from $z \sim 6$ through the eyes of JWST. *arXiv e-prints*, page arXiv:2305.02478.

Huertas-Company, M., Rodriguez-Gomez, V., Nelson, D., Pillepich, A., Bottrell, C., Bernardi, M., Domínguez-Sánchez, H., Genel, S., Pakmor, R., Snyder, G. F.,

and Vogelsberger, M. (2019). The Hubble Sequence at z $\sim$ 0 in the IllustrisTNG simulation with deep learning. , 489(2):1859–1879.

Jacobs, C., Glazebrook, K., Calabrò, A., Treu, T., Nannayakkara, T., Jones, T., Merlin, E., Abraham, R., Stevens, A. R. H., Vulcani, B., Yang, L., Bonchi, A., Boyett, K., Bradač, M., Castellano, M., Fontana, A., Marchesini, D., Malkan, M., Mason, C., Morishita, T., Paris, D., Santini, P., Trenti, M., and Wang, X. (2023). Early Results from GLASS-JWST. XVIII. A First Morphological Atlas of the $1 < z < 5$ Universe in the Rest-frame Optical. , 948(2):L13.

Kartaltepe, J. S., Mozena, M., Kocevski, D., McIntosh, D. H., Lotz, J., Bell, E. F., Faber, S., Ferguson, H., Koo, D., Bassett, R., Bernyk, M., Blancato, K., Bournaud, F., Cassata, P., Castellano, M., Cheung, E., Conselice, C. J., Croton, D., Dahlen, T., de Mello, D. F., DeGroot, L., Donley, J., Guedes, J., Grogin, N., Hathi, N., Hilton, M., Hollon, B., Koekemoer, A., Liu, N., Lucas, R. A., Martig, M., McGrath, E., McPartland, C., Mobasher, B., Morlock, A., O'Leary, E., Peth, M., Pforr, J., Pillepich, A., Rosario, D., Soto, E., Straughn, A., Telford, O., Sunnquist, B., Trump, J., Weiner, B., Wuyts, S., Inami, H., Kassin, S., Lani, C., Poole, G. B., and Rizer, Z. (2015). CANDELS Visual Classifications: Scheme, Data Release, and First Results. , 221(1):11.

Koekemoer, A. M., Faber, S. M., Ferguson, H. C., Grogin, N. A., Kocevski, D. D., Koo, D. C., Lai, K., Lotz, J. M., Lucas, R. A., McGrath, E. J., Ogaz, S., Rajan, A., Riess, A. G., Rodney, S. A., Strolger, L., Casertano, S., Castellano, M., Dahlen, T., Dickinson, M., Dolch, T., Fontana, A., Giavalisco, M., Grazian, A., Guo, Y., Hathi, N. P., Huang, K.-H., van der Wel, A., Yan, H.-J., Acquaviva, V., Alexander, D. M., Almaini, O., Ashby, M. L. N., Barden, M., Bell, E. F., Bournaud, F., Brown, T. M., Caputi, K. I., Cassata, P., Challis, P. J., Chary, R.-R., Cheung, E., Cirasuolo, M., Conselice, C. J., Roshan Cooray, A., Croton, D. J., Daddi, E., Davé, R., de Mello, D. F., de Ravel, L., Dekel, A., Donley, J. L., Dunlop, J. S., Dutton, A. A., Elbaz, D., Fazio, G. G., Filippenko, A. V., Finkelstein, S. L., Frazer, C., Gardner, J. P., Garnavich, P. M., Gawiser, E., Gruetzbauch, R., Hartley, W. G., Häussler, B., Herrington, J., Hopkins, P. F., Huang, J.-S., Jha, S. W., Johnson, A., Kartaltepe, J. S., Khostovan, A. A., Kirshner, R. P., Lani, C., Lee, K.-S., Li, W., Madau, P., McCarthy, P. J., McIntosh, D. H., McLure, R. J., McPartland, C., Mobasher, B., Moreira, H., Mortlock, A., Moustakas, L. A., Mozena, M., Nandra, K., Newman, J. A., Nielsen, J. L., Niemi, S., Noeske, K. G., Papovich, C. J., Pentericci, L., Pope, A., Primack, J. R., Ravindranath, S., Reddy, N. A., Renzini, A., Rix, H.-W., Robaina, A. R., Rosario, D. J., Rosati, P., Salimbeni, S., Scarlata, C., Siana, B., Simard, L., Smidt, J., Snyder, D., Somerville, R. S., Spinrad, H., Straughn, A. N., Telford, O., Teplitz, H. I., Trump, J. R., Vargas, C., Villforth, C., Wagner, C. R., Wandro, P., Wechsler, R. H., Weiner, B. J., Wiklind, T., Wild, V., Wilson, G., Wuyts, S., and Yun, M. S. (2011). CANDELS: The Cosmic Assembly Near-infrared Deep Extragalactic Legacy Survey—The Hubble Space Telescope Observations, Imaging Data Products, and Mosaics. , 197(2):36.

Kormendy, J. and Bender, R. (1996). A Proposed Revision of the Hubble Sequence for Elliptical Galaxies. , 464:L119.

Koutsouridou, I. and Cattaneo, A. (2022). Probing the link between quenching and morphological evolution. , 516(3):4194–4211.

Larson, R. B., Tinsley, B. M., and Caldwell, C. N. (1980). The evolution of disk galaxies and the origin of S0 galaxies. , 237:692–707.

Laurikainen, E., Salo, H., Buta, R., Knapen, J. H., and Comerón, S. (2010). Photometric scaling relations of lenticular and spiral galaxies. , 405(2):1089–1118.

Lee, B., Giavalisco, M., Williams, C. C., Guo, Y., Lotz, J., Van der Wel, A., Ferguson, H. C., Faber, S. M., Koekemoer, A., Grogin, N., Kocevski, D., Conselice, C. J., Wuyts, S., Dekel, A., Kartaltepe, J., and Bell, E. F. (2013). CANDELS: The Correlation between Galaxy Morphology and Star Formation Activity at z ~2. , 774(1):47.

Lerner, E. J., Falomo, R., and Scarpa, R. (2014). UV surface brightness of galaxies from the local universe to z ~5. *International Journal of Modern Physics D*, 23(6):1450058.

Lidman, C., Iacobuta, G., Bauer, A. E., Barrientos, L. F., Cerulo, P., Couch, W. J., Delaye, L., Demarco, R., Ellingson, E., Faloon, A. J., Gilbank, D., Huertas-Company, M., Mei, S., Meyers, J., Muzzin, A., Noble, A., Nantais, J., Rettura, A., Rosati, P., Sánchez-Janssen, R., Strazzullo, V., Webb, T. M. A., Wilson, G., Yan, R., and Yee, H. K. C. (2013). The importance of major mergers in the build up of stellar mass in brightest cluster galaxies at z = 1. , 433(1):825–837.

Longhetti, M., Saracco, P., Severgnini, P., Della Ceca, R., Mannucci, F., Bender, R., Drory, N., Feulner, G., and Hopp, U. (2007). The Kormendy relation of massive elliptical galaxies at z ~1.5: evidence for size evolution. , 374(2):614–626.

Lotz, J. M., Davis, M., Faber, S. M., Guhathakurta, P., Gwyn, S., Huang, J., Koo, D. C., Le Floc'h, E., Lin, L., Newman, J., Noeske, K., Papovich, C., Willmer, C. N. A., Coil, A., Conselice, C. J., Cooper, M., Hopkins, A. M., Metevier, A., Primack, J., Rieke, G., and Weiner, B. J. (2008). The Evolution of Galaxy Mergers and Morphology at z $<$ 1.2 in the Extended Groth Strip. , 672(1):177–197.

Lotz, J. M., Primack, J., and Madau, P. (2004). A New Nonparametric Approach to Galaxy Morphological Classification. , 128(1):163–182.

Lu, S., Fang, G., Gu, Y., Yuan, Q., Cai, Z.-Y., and Kong, X. (2021). The Effect of the Morphological Quenching Mechanism on Star Formation Activity at 0.5 $<$ z $<$ 1.5 in 3D-HST/CANDELS. , 913(2):81.

Madau, P. and Dickinson, M. (2014). Cosmic Star-Formation History. , 52:415–486.

Magdis, G. E., Gobat, R., Valentino, F., Daddi, E., Zanella, A., Kokorev, V., Toft, S., Jin, S., and Whitaker, K. E. (2021). The interstellar medium of quiescent galaxies and its evolution with time. , 647:A33.

Margalef-Bentabol, B., Conselice, C. J., Haeussler, B., Casteels, K., Lintott, C., Masters, K., and Simmons, B. (2022). Observations of the initial formation and evolution of spiral galaxies at $1 < z < 3$ in the CANDELS fields. , 511(1):1502–1517.

Martin, G., Kaviraj, S., Hocking, A., Read, S. C., and Geach, J. E. (2020). Galaxy morphological classification in deep-wide surveys via unsupervised machine learning. , 491(1):1408–1426.

Masters, K. L., Mosleh, M., Romer, A. K., Nichol, R. C., Bamford, S. P., Schawinski, K., Lintott, C. J., Andreescu, D., Campbell, H. C., Crowcroft, B., Doyle, I., Edmondson, E. M., Murray, P., Raddick, M. J., Slosar, A., Szalay, A. S., and Vandenberg, J. (2010). Galaxy Zoo: passive red spirals. , 405(2):783–799.

Momcheva, I. G., Brammer, G. B., van Dokkum, P. G., Skelton, R. E., Whitaker, K. E., Nelson, E. J., Fumagalli, M., Maseda, M. V., Leja, J., Franx, M., Rix, H.-W., Bezanson, R., Da Cunha, E., Dickey, C., Förster Schreiber, N. M., Illingworth, G., Kriek, M., Labbé, I., Ulf Lange, J., Lundgren, B. F., Magee, D., Marchesini, D., Oesch, P., Pacifici, C., Patel, S. G., Price, S., Tal, T., Wake, D. A., van der Wel, A., and Wuyts, S. (2016). The 3D-HST Survey: Hubble Space Telescope WFC3/G141 Grism Spectra, Redshifts, and Emission Line Measurements for ~100,000 Galaxies. , 225(2):27.

Moore, B., Katz, N., Lake, G., Dressler, A., and Oemler, A. (1996). Galaxy harassment and the evolution of clusters of galaxies. , 379(6566):613–616.

Nelson, D., Pillepich, A., Springel, V., Pakmor, R., Weinberger, R., Genel, S., Torrey, P., Vogelsberger, M., Marinacci, F., and Hernquist, L. (2019). First results from the TNG50 simulation: galactic outflows driven by supernovae and black hole feedback. , 490(3):3234–3261.

Nesvadba, N. P. H., Bicknell, G. V., Mukherjee, D., and Wagner, A. Y. (2020). Gas, dust, and star formation in the positive AGN feedback candidate 4C 41.17 at $z = 3.8$. , 639:L13.

Oke, J. B. and Gunn, J. E. (1983). Secondary standard stars for absolute spectrophotometry. , 266:713–717.

Ownsworth, J. R., Conselice, C. J., Mortlock, A., Hartley, W. G., Almaini, O., Duncan, K., and Mundy, C. J. (2014). Minor versus major mergers: the stellar mass growth of massive galaxies from $z = 3$ using number density selection techniques. , 445(3):2198–2213.

Paillalef, M. G., Flores, H., Demarco, R., Rettura, A., Jaffé, Y., Lidman, C., Nantais, J., Puech, M., and Rosati, P. (2021). Ionized gas kinematics of cluster AGN at z 0.8 with KMOS. , 506(1):385–395.

Patel, S. G., Kelson, D. D., Holden, B. P., Franx, M., and Illingworth, G. D. (2011). The Star-formation-rate-Density Relation at $0.6 < z < 0.9$ and the Role of Star-forming Galaxies. , 735(1):53.

Paulino-Afonso, A., Sobral, D., Buitrago, F., and Afonso, J. (2017). The structural and size evolution of star-forming galaxies over the last 11 Gyr. , 465(3):2717–2733.

Pawlik, M. M., Wild, V., Walcher, C. J., Johansson, P. H., Villforth, C., Rowlands, K., Mendez-Abreu, J., and Hewlett, T. (2016). Shape asymmetry: a morphological indicator for automatic detection of galaxies in the post-coalescence merger stages. , 456(3):3032–3052.

Peng, C. Y., Ho, L. C., Impey, C. D., and Rix, H.-W. (2011). GALFIT: Detailed Structural Decomposition of Galaxy Images. Astrophysics Source Code Library, record ascl:1104.010.

Pérez-Carrasco, M., Cabrera-Vives, G., Martinez-Marin, M., Cerulo, P., Demarco, R., Protopapas, P., Godoy, J., and Huertas-Company, M. (2019). Multiband Galaxy Morphologies for CLASH: A Convolutional Neural Network Transferred from CANDELS. , 131(1004):108002.

Pillepich, A., Nelson, D., Springel, V., Pakmor, R., Torrey, P., Weinberger, R., Vogelsberger, M., Marinacci, F., Genel, S., van der Wel, A., and Hernquist, L. (2019). First results from the TNG50 simulation: the evolution of stellar and gaseous discs across cosmic time. , 490(3):3196–3233.

Postman, M., Coe, D., Benítez, N., Bradley, L., Broadhurst, T., Donahue, M., Ford, H., Graur, O., Graves, G., Jouvel, S., Koekemoer, A., Lemze, D., Medezinski, E., Molino, A., Moustakas, L., Ogaz, S., Riess, A., Rodney, S., Rosati, P., Umetsu, K., Zheng, W., Zitrin, A., Bartelmann, M., Bouwens, R., Czakon, N., Golwala, S., Host, O., Infante, L., Jha, S., Jimenez-Teja, Y., Kelson, D., Lahav, O., Lazkoz, R., Maoz, D., McCully, C., Melchior, P., Meneghetti, M., Merten, J., Moustakas, J., Nonino, M., Patel, B., Regös, E., Sayers, J., Seitz, S., and Van der Wel, A. (2012). The Cluster Lensing and Supernova Survey with Hubble: An Overview. , 199(2):25.

Postman, M., Franx, M., Cross, N. J. G., Holden, B., Ford, H. C., Illingworth, G. D., Goto, T., Demarco, R., Rosati, P., Blakeslee, J. P., Tran, K. V., Benítez, N., Clampin, M., Hartig, G. F., Homeier, N., Ardila, D. R., Bartko, F., Bouwens, R. J., Bradley, L. D., Broadhurst, T. J., Brown, R. A., Burrows, C. J., Cheng, E. S., Feldman, P. D., Golimowski, D. A., Gronwall, C., Infante, L., Kimble, R. A., Krist, J. E., Lesser, M. P., Martel, A. R., Mei, S., Menanteau, F., Meurer, G. R., Miley, G. K., Motta, V., Sirianni, M., Sparks, W. B., Tran, H. D.,

Tsvetanov, Z. I., White, R. L., and Zheng, W. (2005). The Morphology-Density Relation in z ~1 Clusters. , 623(2):721–741.

Querejeta, M., Eliche-Moral, M. C., Tapia, T., Borlaff, A., van de Ven, G., Lyubenova, M., Martig, M., Falcón-Barroso, J., and Méndez-Abreu, J. (2015). Formation of S0 galaxies through mergers. Explaining angular momentum and concentration change from spirals to S0s. , 579:L2.

Renzini, A. (2016). The dominance of quenching through cosmic times. , 460(1):L45–L49.

Rodriguez-Gomez, V., Pillepich, A., Sales, L. V., Genel, S., Vogelsberger, M., Zhu, Q., Wellons, S., Nelson, D., Torrey, P., Springel, V., Ma, C.-P., and Hernquist, L. (2016). The stellar mass assembly of galaxies in the Illustris simulation: growth by mergers and the spatial distribution of accreted stars. , 458(3):2371–2390.

Rodriguez-Gomez, V., Snyder, G. F., Lotz, J. M., Nelson, D., Pillepich, A., Springel, V., Genel, S., Weinberger, R., Tacchella, S., Pakmor, R., Torrey, P., Marinacci, F., Vogelsberger, M., Hernquist, L., and Thilker, D. A. (2019). The optical morphologies of galaxies in the IllustrisTNG simulation: a comparison to Pan-STARRS observations. , 483(3):4140–4159.

Rupke, D. S. N., Kewley, L. J., and Barnes, J. E. (2010). Galaxy Mergers and the Mass-Metallicity Relation: Evidence for Nuclear Metal Dilution and Flattened Gradients from Numerical Simulations. , 710(2):L156–L160.

Ryden, B. S. and Gunn, J. E. (1987). Galaxy Formation by Gravitational Collapse. , 318:15.

Sandage, A. (1961). *The Hubble Atlas of Galaxies.*

Sandage, A., Sandage, M., and Kristian, J. (1975). *Galaxies and the universe.*

Sazonova, E., Alatalo, K., Lotz, J., Rowlands, K., Snyder, G. F., Boone, K., Brodwin, M., Hayden, B., Lanz, L., Perlmutter, S., and Rodriguez-Gomez, V. (2020). The Morphology-Density Relationship in $1 < z < 2$ Clusters. , 899(1):85.

Schawinski, K., Urry, C. M., Simmons, B. D., Fortson, L., Kaviraj, S., Keel, W. C., Lintott, C. J., Masters, K. L., Nichol, R. C., Sarzi, M., Skibba, R., Treister, E., Willett, K. W., Wong, O. I., and Yi, S. K. (2014). The green valley is a red herring: Galaxy Zoo reveals two evolutionary pathways towards quenching of star formation in early- and late-type galaxies. , 440(1):889–907.

Schreiber, C., Pannella, M., Elbaz, D., Béthermin, M., Inami, H., Dickinson, M., Magnelli, B., Wang, T., Aussel, H., Daddi, E., Juneau, S., Shu, X., Sargent, M. T., Buat, V., Faber, S. M., Ferguson, H. C., Giavalisco, M., Koekemoer, A. M., Magdis, G., Morrison, G. E., Papovich, C., Santini, P., and Scott, D. (2015). The Herschel view of the dominant mode of galaxy growth from $z = 4$ to the present day. , 575:A74.

Sérsic, J. L. (1963). Influence of the atmospheric and instrumental dispersion on the brightness distribution in a galaxy. *Boletin de la Asociacion Argentina de Astronomia La Plata Argentina*, 6:41–43.

Simard, L. (2010). GIM2D: Galaxy IMage 2D. Astrophysics Source Code Library, record ascl:1004.001.

Skelton, R. E., Whitaker, K. E., Momcheva, I. G., Brammer, G. B., van Dokkum, P. G., Labbé, I., Franx, M., van der Wel, A., Bezanson, R., Da Cunha, E., Fumagalli, M., Förster Schreiber, N., Kriek, M., Leja, J., Lundgren, B. F., Magee, D., Marchesini, D., Maseda, M. V., Nelson, E. J., Oesch, P., Pacifici, C., Patel, S. G., Price, S., Rix, H.-W., Tal, T., Wake, D. A., and Wuyts, S. (2014). 3D-HST WFC3-selected Photometric Catalogs in the Five CANDELS/3D-HST Fields: Photometry, Photometric Redshifts, and Stellar Masses. , 214(2):24.

Snyder, G. F., Lotz, J. M., Rodriguez-Gomez, V., Guimarães, R. d. S., Torrey, P., and Hernquist, L. (2017). Massive close pairs measure rapid galaxy assembly in mergers at high redshift. , 468(1):207–216.

Sobral, D., Swinbank, A. M., Stott, J. P., Matthee, J., Bower, R. G., Smail, I., Best, P., Geach, J. E., and Sharples, R. M. (2013). The Dynamics of z = 0.8 Hα-selected Star-forming Galaxies from KMOS/CF-HiZELS. , 779(2):139.

Springel, V. (2010). E pur si muove: Galilean-invariant cosmological hydrodynamical simulations on a moving mesh. , 401(2):791–851.

Strateva, I., Ivezić, Ž., Knapp, G. R., Narayanan, V. K., Strauss, M. A., Gunn, J. E., Lupton, R. H., Schlegel, D., Bahcall, N. A., Brinkmann, J., Brunner, R. J., Budavári, T., Csabai, I., Castander, F. J., Doi, M., Fukugita, M., Győry, Z., Hamabe, M., Hennessy, G., Ichikawa, T., Kunszt, P. Z., Lamb, D. Q., McKay, T. A., Okamura, S., Racusin, J., Sekiguchi, M., Schneider, D. P., Shimasaku, K., and York, D. (2001). Color Separation of Galaxy Types in the Sloan Digital Sky Survey Imaging Data. , 122(4):1861–1874.

Tacchella, S., Carollo, C. M., Renzini, A., Förster Schreiber, N. M., Lang, P., Wuyts, S., Cresci, G., Dekel, A., Genzel, R., Lilly, S. J., Mancini, C., Newman, S., Onodera, M., Shapley, A., Tacconi, L., Woo, J., and Zamorani, G. (2015). Evidence for mature bulges and an inside-out quenching phase 3 billion years after the Big Bang. *Science*, 348(6232):314–317.

Tapia, T., Eliche-Moral, M. C., Aceves, H., Rodríguez-Pérez, C., Borlaff, A., and Querejeta, M. (2017). Formation of S0 galaxies through mergers. Evolution in the Tully-Fisher relation since z $\sim$ 1. , 604:A105.

Tolman, R. C. (1930). On the Use of the Energy-Momentum Principle in General Relativity. *Physical Review*, 35(8):875–895.

Trenti, M. and Stiavelli, M. (2008). Cosmic Variance and Its Effect on the Luminosity Function Determination in Deep High-z Surveys. , 676(2):767–780.

Treu, T., Ellis, R. S., Kneib, J.-P., Dressler, A., Smail, I., Czoske, O., Oemler, A., and Natarajan, P. (2003). A Wide-Field Hubble Space Telescope Study of the Cluster Cl 0024+16 at z = 0.4. I. Morphological Distributions to 5 Mpc Radius. , 591(1):53–78.

Tumlinson, J., Peeples, M. S., and Werk, J. K. (2017). The Circumgalactic Medium. , 55(1):389–432.

van den Bergh, S. (2009). Lenticular Galaxies and their Environments. , 702(2):1502–1506.

van der Wel, A. (2008). The Dependence of Galaxy Morphology and Structure on Environment and Stellar Mass. , 675(1):L13.

van der Wel, A., Bell, E. F., Holden, B. P., Skibba, R. A., and Rix, H.-W. (2010). The Physical Origins of the Morphology-Density Relation: Evidence for Gas Stripping from the Sloan Digital Sky Survey. , 714(2):1779–1788.

van Dokkum, P. G. and Franx, M. (2001). Morphological Evolution and the Ages of Early-Type Galaxies in Clusters. *arXiv e-prints*, pages astro–ph/0101468.

van Dokkum, P. G., Franx, M., Kriek, M., Holden, B., Illingworth, G. D., Magee, D., Bouwens, R., Marchesini, D., Quadri, R., Rudnick, G., Taylor, E. N., and Toft, S. (2008). Confirmation of the Remarkable Compactness of Massive Quiescent Galaxies at z ~2.3: Early-Type Galaxies Did not Form in a Simple Monolithic Collapse. , 677(1):L5.

Varma, S., Huertas-Company, M., Pillepich, A., Nelson, D., Rodriguez-Gomez, V., Dekel, A., Faber, S. M., Iglesias-Navarro, P., Koo, D. C., and Primack, J. (2022). The building up of observed stellar scaling relations of massive galaxies and the connection to black hole growth in the TNG50 simulation. , 509(2):2654–2673.

Vogelsberger, M., Genel, S., Springel, V., Torrey, P., Sijacki, D., Xu, D., Snyder, G., Bird, S., Nelson, D., and Hernquist, L. (2014a). Properties of galaxies reproduced by a hydrodynamic simulation. , 509(7499):177–182.

Vogelsberger, M., Genel, S., Springel, V., Torrey, P., Sijacki, D., Xu, D., Snyder, G., Nelson, D., and Hernquist, L. (2014b). Introducing the Illustris Project: simulating the coevolution of dark and visible matter in the Universe. , 444(2):1518–1547.

Walters, D., Woo, J., and Ellison, S. L. (2022). Quenching time-scales in the IllustrisTNG simulation. , 511(4):6126–6142.

Wang, T., Huang, J.-S., Faber, S. M., Fang, G., Wuyts, S., Fazio, G. G., Yan, H., Dekel, A., Guo, Y., Ferguson, H. C., Grogin, N., Lotz, J. M., Weiner, B., McGrath, E. J., Kocevski, D., Hathi, N. P., Lucas, R. A., Koekemoer, A. M., Kong, X., and Gu, Q.-S. (2012). CANDELS: Correlations of Spectral Energy Distributions and Morphologies with Star formation Status for Massive Galaxies at z ~2. , 752(2):134.

Wetzel, A. R., Tinker, J. L., Conroy, C., and van den Bosch, F. C. (2013). Galaxy evolution in groups and clusters: satellite star formation histories and quenching time-scales in a hierarchical Universe. , 432(1):336–358.

Whitney, A., Ferreira, L., Conselice, C. J., and Duncan, K. (2021). Galaxy Evolution in All Five CANDELS Fields and IllustrisTNG: Morphological, Structural, and the Major Merger Evolution to z 3. , 919(2):139.

Windhorst, R. A., Mather, J., Clampin, M., Doyon, R., Flanagan, K., Franx, M., Gardner, J., Greenhouse, M., Hammel, H., Huchings, J., Jakobsen, P., Lilly, S., McCaughrean, M., Mountain, M., Rieke, G., Sonneborn, G., Stiavelli, M., and Wright, G. (2009). Galaxies Across Cosmic Time with JWST. In *astro2010: The Astronomy and Astrophysics Decadal Survey*, volume 2010, page 317.

York, D. G., Adelman, J., Anderson, Jr., J. E., Anderson, S. F., Annis, J., Bahcall, N. A., Bakken, J. A., Barkhouser, R., Bastian, S., Berman, E., Boroski, W. N., Bracker, S., Briegel, C., Briggs, J. W., Brinkmann, J., Brunner, R., Burles, S., Carey, L., Carr, M. A., Castander, F. J., Chen, B., Colestock, P. L., Connolly, A. J., Crocker, J. H., Csabai, I., Czarapata, P. C., Davis, J. E., Doi, M., Dombeck, T., Eisenstein, D., Ellman, N., Elms, B. R., Evans, M. L., Fan, X., Federwitz, G. R., Fiscelli, L., Friedman, S., Frieman, J. A., Fukugita, M., Gillespie, B., Gunn, J. E., Gurbani, V. K., de Haas, E., Haldeman, M., Harris, F. H., Hayes, J., Heckman, T. M., Hennessy, G. S., Hindsley, R. B., Holm, S., Holmgren, D. J., Huang, C.-h., Hull, C., Husby, D., Ichikawa, S.-I., Ichikawa, T., Ivezić, Ž., Kent, S., Kim, R. S. J., Kinney, E., Klaene, M., Kleinman, A. N., Kleinman, S., Knapp, G. R., Korienek, J., Kron, R. G., Kunszt, P. Z., Lamb, D. Q., Lee, B., Leger, R. F., Limmongkol, S., Lindenmeyer, C., Long, D. C., Loomis, C., Loveday, J., Lucinio, R., Lupton, R. H., MacKinnon, B., Mannery, E. J., Mantsch, P. M., Margon, B., McGehee, P., McKay, T. A., Meiksin, A., Merelli, A., Monet, D. G., Munn, J. A., Narayanan, V. K., Nash, T., Neilsen, E., Neswold, R., Newberg, H. J., Nichol, R. C., Nicinski, T., Nonino, M., Okada, N., Okamura, S., Ostriker, J. P., Owen, R., Pauls, A. G., Peoples, J., Peterson, R. L., Petravick, D., Pier, J. R., Pope, A., Pordes, R., Prosapio, A., Rechenmacher, R., Quinn, T. R., Richards, G. T., Richmond, M. W., Rivetta, C. H., Rockosi, C. M., Ruthmansdorfer, K., Sandford, D., Schlegel, D. J., Schneider, D. P., Sekiguchi, M., Sergey, G., Shimasaku, K., Siegmund, W. A., Smee, S., Smith, J. A., Snedden, S., Stone, R., Stoughton, C., Strauss, M. A., Stubbs, C., SubbaRao, M., Szalay, A. S., Szapudi, I., Szokoly, G. P., Thakar, A. R., Tremonti, C., Tucker, D. L., Uomoto, A., Vanden Berk, D., Vogeley, M. S., Waddell, P., Wang, S.-i., Watanabe, M., Weinberg, D. H., Yanny, B., Yasuda, N., and SDSS Collaboration (2000). The Sloan Digital Sky Survey: Technical Summary. , 120:1579–1587.

Appendix A

Appendix A

A1 Energy, luminosity- and angular distance

A source located at co-moving distance r_1 with luminosity L emits N photons of energy E in a time interval Δt_1. An observer receives those photons at a distance $a_0 r_1$ from the source, where a_0 is the scale factor of the Universe at the present epoch.

A1.1 Energy and Scale Factor

The scale factor a describes how the universe expands with time. As light travels from the source to the observer, its frequency increases because of the expansion of the Universe. Redshift z can be defined as the fractional increase in wavelength between the observed, λ_{obs}, and emitted, λ_{em}, wavelengths of light:

$$z = \frac{\lambda_{obs} - \lambda_{em}}{\lambda_{em}}, \tag{A1.1}$$

One can also express the relation between the emitted and observed wavelengths in terms of the scale factor as:

$$\lambda_{obs} = a \cdot \lambda_{em}. \tag{A1.2}$$

Substituting equation A1.1 in equation A1.2, we get:

$$z = \frac{a \cdot \lambda_{em} - \lambda_{em}}{\lambda_{em}} = a - 1. \tag{A1.3}$$

A1.2 Luminosity Distance

The relative velocity between the observer and the galaxy is given by

$$dv = H\,dr = \frac{\dot{a}}{a}, \tag{A1.4}$$

where H is the Hubble-Lemaître constant. The Doppler law enables one to determine the variation in the wavelength of a photon, $d\lambda$, as it moves between the two locations,

$$\frac{\delta\lambda}{\lambda} = \frac{dv}{c}. \tag{A1.5}$$

By using Equation A1.4 and A1.5 along with the formula for the travel time of the photon, which is expressed as $dt = dr/c$, we find:

$$\frac{d\lambda}{\lambda} = \frac{\dot{a}}{a}\frac{dr}{c} = \frac{\dot{a}}{a}dt. \tag{A1.6}$$

Integrating the above we get that $\ln(\lambda) = \ln(a) + C$, where C is a constant. Thus:

$$\lambda \propto a. \tag{A1.7}$$

As the energy of a photon is directly proportional to its wavelength, we can write:

$$E = \frac{hc}{\lambda} \propto a, \tag{A1.8}$$

where h is the Planck's constant. This result implies that radiation will lose energy proportionally to the scale factor a due to the redshift of photons. Using equation A1.3, we can write the following relation:

$$E_0 = E_1\frac{a_1}{a_0} = \frac{E_1}{1+z}, \tag{A1.9}$$

where E_0 is the received energy and E_1 is the emitted energy. From the Friedmann equation for a matter-dominated universe with no cosmological constant we derive that:

$$\Delta t_0 = \Delta t_1\frac{a_1}{a_0} = \frac{E_1}{1+z}. \tag{A1.10}$$

We now write an expression for the observed flux F_0, which is defined as unit energy per unit of time per unit of area:

$$F_0 = \frac{(N \cdot E_0)/\Delta t_0}{4\pi d^2} = \frac{(N \cdot E_0/\Delta t_0)}{4\pi (a_0 r_1)^2} = \frac{N \cdot E_0}{4\pi a_0^2 r_1^2 \Delta t_0}. \tag{A1.11}$$

We now use equations A1.9 and A1.10 on the above expression:

$$F_0 = \frac{N \cdot E_1 \left(\frac{a_1}{a_0}\right)}{4\pi a_0^2 r_1^2 \Delta t_1 \left(\frac{a_1}{a_0}\right)} = \frac{(N \cdot E_1/\Delta t_1}{4\pi a_0^2 r_1^2 \left(\frac{a_0}{a_1}\right)^2} = \frac{L}{4\pi a_0^2 r_1^2 (1+z)^2} = \frac{L}{4\pi d_L^2}, \tag{A1.12}$$

where we have defined the luminosity distance, which is the distance at which a source would have to be located in order for its observed luminosity to match its intrinsic luminosity, as $d_L \equiv a_0 r_1 (1+z)$.

A1.3 Angular diameter Distance

Another way to measure cosmological distances is through the angular diameter distance. We can measure the angular size ($\Delta\theta$) of an extended source as:

$$\Delta\theta = \frac{D}{r_1}, \qquad (r_1 \gg D), \tag{A1.13}$$

where D is the proper diameter or the physical diameter of the source and r_1 is the proper distance. Then we can write:

$$D = (a_1 r_1)\Delta\theta, \tag{A1.14}$$

which follows:

$$r_1 = \frac{d_L}{a_0(1+z)}. \tag{A1.15}$$

With this we define the angular distance as:

$$d_A \equiv \frac{D}{\Delta\theta} = a_1 r_1 = a_1 \frac{d_L}{a_0(1+z)} = \frac{d_L}{(1+z)^2}. \tag{A1.16}$$

The angular diameter distance is the distance required for an object to look with an angular size $\Delta\theta$.

A2 First Correction Method: Example

The spheroid correction percentage for false-negatives can be computed as one minus the quotient of the number of authentic spheroids observed in bin 3 (10) and the total number of spheroids observed in that bin (63):

$$FP_{3,S} = (1 - TP) = 1 - \frac{n_{3,S}}{N_{3,S}} = 1 - \frac{10}{63} \approx 0.8412. \tag{A2.1}$$

To correct for false negatives in the irregular class, we calculate the fraction of irregular galaxies in bin 3 that were classified as spheroids in bin 0, with respect to the total number of irregulars observed in that bin (52 objects):

$$FN_{3,S,I} = \frac{n_{3,I,S}}{N_{3,I}} = \frac{1}{52} \approx 0.0192. \tag{A2.2}$$

The procedure for calculating the false negative correction term is similar for unclassifiable objects.

$$FN_{3,S,U} = \frac{n_{3,U,S}}{N_{3,U}} = \frac{3}{6} = 0.5. \tag{A2.3}$$

We omit the details of the calculation for early-type and late-type disks since it is evident that their correction factors are zero.

Based on the derived correction terms, the corrected morphological counts of spheroids in bin 3 can now be obtained. Specifically, we subtract 84.12% of the observed spheroids in bin 3 from the total number of spheroids observed in that bin (63), and add the contribution of 1.92% of the irregular and 50% of the unclassifiable objects observed in bin 3 (52 and 6, respectively).

$$\begin{aligned} N_{3,S} &= X_{3,S} - (X_{3,S} \cdot FP_{3,S}) + \ldots && \text{(A2.4)} \\ &\quad \cdots + (X_{3,I} \cdot FN_{3,S,I}) + (X_{3,U} \cdot FN_{3,S,U}), && \text{(A2.5)} \\ &= 63 - (63 \cdot 0.8412) + (52 \cdot 0.0192) + (6 \cdot 0.5), && \text{(A2.6)} \\ &= 14. && \text{(A2.7)} \end{aligned}$$

To summarize, in our initial sample, 14 galaxies were classified as spheroids in bin 0, and 63 spheroids were observed in bin 3. After applying the correction for the CSBD effect, we were able to recover the true number of spheroids in

bin 3, which is 14. Please note that this example serves as an illustration to demonstrate the effectiveness of our defined correction percentages in restoring the initial morphological counts. It is important to emphasize that this is merely a hypothetical scenario and not reflective of any specific data or research findings.